

**MICROSTRUCTURE AND MECHANICAL PROPERTIES OF
AL AND AL/SI ALLOYED TRIP-ASSISTED STEELS
PRODUCED THROUGH GALVANIZING HEAT TREATMENTS**

**MICROSTRUCTURE AND MECHANICAL PROPERTIES OF
AL AND AL/SI ALLOYED TRIP-ASSISTED STEELS
PRODUCED THROUGH GALVANIZING HEAT TREATMENTS**

By

YANKUI BIAN, M. ENG.

A Thesis

Submitted to the School of Graduate Studies

in Partial Fulfilment of the Requirements

for the Degree of

Master of Applied Science

McMaster University

© Copyright by Yankui Bian, January 2009

MASTER OF APPLIED SCIENCE (2009)

(Materials of Science and Engineering)

McMaster University

Hamilton, Ontario

TITLE: Microstructure and Mechanical Properties of
Al and Al/Si Alloyed TRIP-assisted Steels
Produced through Galvanizing Heat Treatments

AUTHOR: Yankui Bian, M. Eng.
(Northeastern University, Shenyang, China)

SUPERVISORS: Dr. J.R. McDermid and Dr. H.S. Zurob

NUMBER OF PAGES: xiv, 160

ABSTRACT

TRIP-assisted steels combine high strength and good ductility, which makes them attractive to the automotive industry. Simultaneously, galvanizing is essential for the corrosion resistance of these steels. In industrial practice, the processing of TRIP-assisted steels and galvanizing process must be combined.

Two Al-alloyed TRIP-assisted steels (**1.0Al**: 0.2C-1.5Mn-0.5Si-1.0Al (wt.%) and **1.5Al**: 0.2C-1.5Mn-1.5Al (wt.)) were investigated in the present research work, where two points are noteworthy. First, the experimental processing routes in the present work are compatible with the continuous galvanizing process; second, it has been shown that the two steels exhibit good galvanizability. The initial microstructure and its evolution during plastic deformation of the two steels were examined. The kinetics of phase transformations taking place during thermal processing and plastic deformation were discussed. These results were linked to the work hardening behaviour with kinematic hardening taken into account.

It was confirmed that the retained austenite in the steels obtained through the present galvanizing heat treatments contributed to the work hardening behaviour by transforming to martensite during plastic deformation. The 1.5Al steel exhibited a better work hardening behaviour due to the more stable retained austenite.

Retained austenite of higher stability transformed to martensite more gradually during plastic deformation, efficiently attenuating decreases in the instantaneous work hardening rate, $d\sigma/d\varepsilon$, and giving rise to a smoother evolution of the incremental work hardening coefficient, $d(Ln\sigma)/d(Ln\varepsilon)$. One of the attenuating mechanisms was the development of back stresses, which contributed kinematic hardening to the overall work hardening. Gradual transformation of retained austenite to martensite continuously supplied new obstacles to dislocations and delayed the saturation of back stresses.

Based on the present work and the previous work, it seems possible to process galvanizable Al-alloyed TRIP assisted steels using continuous galvanizing thermal cycles, which implies the possibility to combine continuous galvanizing and thermal processing of TRIP-assisted steels.

ACKNOWLEDGEMENTS

I would like very much to express my appreciation and gratitude to my supervisors Dr. McDermid and Dr. Zurob for their guidance and mentoring throughout my stay at McMaster University.

I always believe that I was fortunate to join Dr. McDermid and Dr. Zurob's research group. I sincerely thank them for allowing me to join this research group, so that I could have an opportunity to learn and discover another field about steel, "micro-structure and properties", since my previous background was in process metallurgy (ironmaking and steelmaking). The knowledge that I learned from Dr. McDermid and Dr. Zurob, as well as their advising at the beginning, was very important for me to start this research work. Furthermore, their inspiration and encouragement at the later stage were indispensable for the present research work as a "whole" story. Also I am very thankful for the time that Dr. McDermid and Dr. Zurob spent in reading and reviewing my previous presentation and paper drafts for conferences and the drafts of this thesis. Reading original drafts and making corrections or comments are tedious jobs. I appreciate their patience a lot. Additionally, Dr. McDermid deserves special thanks for giving me an idea about galvanizing, which was completely new for me.

I would also like to say thanks to many students in this research group. Special thanks go to Erika Bellhouse and Xin Liang for helpful discussion. Many technical people

helped me with my experimental work. I sincerely say “thank you” to them. They are Mr. Jason Lavalley, Mr. Christ Butcher, Mr. Doug Culley, Mr. John Rodda, Mr. Rob Lemmon, Dr. Steve Koprach, Dr. James Britten and Dr. Glynis de Silveira.

Last, but not least, I say thanks to my family, my wife and my daughter. They moved with me to Hamilton and lived here for two years. I thank them for their kindness and consideration.

Sincerely,

Yankui Bian

Hamilton, Ontario, Canada

January 2009

TABLE OF CONTENTS

ABSTRACT	iii
ACKNOWLEDGEMENTS	v
TABLE OF CONTENTS	vii
LIST OF FIGURES	x
LIST OF TABLES	xiv
CHAPTER 1 INTRODUCTION	1
1.1 TRIP-assisted Steels	1
1.2 Galvanizing of TRIP-assisted Steels	4
CHAPTER 2 LITERATURE REVIEW	6
2.1 Processing of TRIP-assisted Steels	6
2.1.1 Intercritical Annealing	7
2.1.2 Isothermal Bainitic Transformation	11
2.1.3 Compatibility between Thermal Processing of TRIP-assisted Steels and Continuous galvanizing	21
2.2 Strain Hardening of TRIP-assisted Steels	27
2.2.1 TRIP Effect	27
2.2.2 Composite Strengthening Effect	29
2.3 Kinematic Hardening	31

2.3.1	Development of Back Stresses	31
2.3.2	Measurement of Back Stresses	33
2.3.3	Back Stresses in Hard Phase Dispersed Steels	37
2.4	Models Characterizing the Evolution of $d\sigma/d\varepsilon$	41
CHAPTER 3	RESEARCH OBJECTIVE	45
CHAPTER 4	EXPERIMENTAL METHODS	47
4.1	Steels Investigated	47
4.2	Heat Treatments	49
4.2.1	Heat Treatment Facility	49
4.2.2	Heat Treatment Parameters	51
4.3	Sample Characterization	53
4.3.1	Scanning Electron Microscopy (SEM)	53
4.3.2	X-ray Diffraction (XRD)	56
4.3.3	Quantitative Image Analysis	57
4.4	Tensile Testing	64
4.4.1	Monotonic Tensile Tests	66
4.4.2	Unloading/Reloading Tests	66
4.4.3	Interrupted Tensile Tests	69
4.5	Examination of Fracture Mechanisms	71
CHAPTER 5	EXPERIMENTAL RESULTS	72
5.1	As-annealed Steels	72

5.1.1	Microstructures	72
5.1.2	Retained Austenite Characteristics	77
5.1.3	Monotonic Tensile Properties	79
5.2	Strain-induced Martensite Transformation	91
5.2.1	Microstructural Evolution during Plastic Deformation	91
5.2.2	Transformation of Retained Austenite to Martensite vs. Plastic Strain	97
5.2.3	Kinematic Hardening	106
5.3	Fractography	111
CHAPTER 6	DISCUSSION	117
6.1	Effects of Heat Treatment Parameters and Steel Chemistry on Phase Transformation Kinetics	118
6.1.1	Effects on Phase Transformation Kinetics during Thermal Processing	118
6.1.2	Effects on Phase Transformation Kinetics during Plastic Deformation	123
6.2	Link to Mechanical Properties	130
6.2.1	Incremental Strain Hardening Coefficient	131
6.2.2	Kinematic Hardening	134
6.3	Interpretation of Work Hardening in TRIP-assisted Steels	141
6.4	Compatibility with Continuous Galvanizing Process	147
CHAPTER 7	CONCLUSIONS	149
REFERENCES		152

LIST OF FIGURES

Figure 1.1	Schematic illustration of thermomechanical controlled processing (TMCP) of hot-rolled TRIP-assisted steels.....	3
Figure 2.1	Schematic two-stage processing of cold-rolled TRIP-assisted steels.....	7
Figure 2.2	CCT diagram from $T_{\text{Intercritical Annealing}}=770^{\circ}\text{C}$ (35% intercritical austenite), Steel composition: 0.15C-1.52Mn-0.31Si-1.0Al (wt.%).....	10
Figure 2.3	Schematic illustration of the microstructural features relevant in the kinetic description of a bainitic microstructure	12
Figure 2.4	Schematic illustration of the origin of the T_0 construction on the Fe-C phase diagram.....	13
Figure 2.5	Schematic illustration of two bainite growth mechanisms.....	14
Figure 2.6	Bainite transformation kinetics showing the effect of hold temperatures..	16
Figure 2.7	Ultimate austenite carbon contents affected by holding temperatures.....	16
Figure 2.8	Equilibrium phase diagram calculated using ThermoCalc® schematically showing the carbon concentration process in austenite.....	18
Figure 2.9	Effect of Al on bainite transformation kinetics at 410°C	19
Figure 2.10	Calculated driving force of transformation from austenite to ferrite.....	20
Figure 2.11	Calculated T_0 curves showing the effect of Al additions.....	20
Figure 2.12	TEM graph illustrating the dislocations generated in ferrite at the tip of the strain-induced martensitic variants.....	28
Figure 2.13	Schematic morphology evolution of strain-induced martensite.....	29
Figure 2.14	Comparison of the macroscopic stress and the stress calculated without taking into account the martensitic phase.....	30

Figure 2.15	Schematic illustration showing the development of internal stresses due to incompatible deformation between hard particles and the soft matrix	32
Figure 2.16	Schematic illustration of the Bauschinger test	34
Figure 2.17	Back stresses in spheroidized carbon steels	39
Figure 2.18	Back stresses in a dual phase steel	40
Figure 2.19	Back stresses in a dual phase steel as a function of prestrains showing the saturation takes place at about $\epsilon=0.01$	40
Figure 2.20	$\ln(d\sigma/d\epsilon)$ vs. $\ln\sigma$ plot of a commercial dual phase steel exhibiting three work hardening stages	43
Figure 4.1	Microstructure of as-received steels	48
Figure 4.2	McMaster Galvanizing Simulator	50
Figure 4.3	Geometry of the steel panel and the sample area for analysis	51
Figure 4.4	SEM sample preparation procedures	54
Figure 4.5	SEM micrographs showing distinguishable phases in TRIP-assisted steels after tempering at 250°C for 2 hours	55
Figure 4.6	SEM micrograph showing retained austenite distinguishable in two morphologies	58
Figure 4.7	SEM micrographs of the 1.0Al_35% γ 60s steel for image analysis	60
Figure 4.8	Separated phases of the microstructure shown in Figure 4.7 a)	61
Figure 4.9	Separated phases of the microstructure shown in Figure 4.7 b)	62
Figure 4.10	Schematic definition of equivalent circular diameter	63
Figure 4.11	Schematic definition of thread length (AB) and thread width (CD)	63
Figure 4.12	Geometry of the tensile sample	65
Figure 4.13	The unloading/reloading curve of the 1.5Al_35% γ 120s steel	67

Figure 4.14	The loading/unloading/reloading cycle at the pre-set strain of 0.100 of the 1.5Al _{35%} γ120s steel (the fourth cycle in Figure 4.13)	68
Figure 4.15	The cross-head speed of the unloading/reloading test shown in Figure 4.13	70
Figure 5.1	SEM micrographs of the as-annealed steels	73
Figure 5.2	Phase constituents of the as-annealed steels excluding intercritical ferrite	76
Figure 5.3	True stress-true strain curves of the as-annealed steels prior to the onset of necking	81
Figure 5.4	UTS and ϵ_u of the experimental steels	85
Figure 5.5	Flow curves and incremental work hardening coefficients	87
Figure 5.6	SEM micrographs of the strained 1.0Al _{50%} γ60s steel ($\epsilon=0.025$ and 0.050)	92
Figure 5.7	SEM micrographs of the strained 1.0Al _{50%} γ60s steel ($\epsilon=0.100$)	93
Figure 5.8	SEM micrographs of the strained 1.0Al _{50%} γ120s steel ($\epsilon=0.200$)	93
Figure 5.9	SEM micrographs of the strained 1.0Al steels showing partially-transformed retained austenite grains	95
Figure 5.10	SEM micrographs of the strained 1.5Al steels showing partially-transformed retained austenite grains were rarely observed	96
Figure 5.11	Volume fraction of retained austenite as a function of strain	99
Figure 5.12	Volume fraction of total, blocky and lamellar retained austenite as a function of strain	103
Figure 5.13	Volume fraction of martensite as a function of strain	105
Figure 5.14	Kinematic hardening (back stresses) vs. flow stresses	107
Figure 5.15	SEM micrographs of fracture surfaces	112
Figure 5.16	Enlarged fractographs showing the dimple, cleavage and decohesion surfaces	114

Figure 5.17	Decohesion at retained austenite particles.....	116
Figure 5.18	Cracking at a band region.....	116
Figure 6.1	Phase constituents of the as-annealed steels excluding intercritical ferrite showing the effect of intercritical annealing temperatures.....	120
Figure 6.2	Strain-induced transformation kinetics of the 1.0Al steels.....	127
Figure 6.3	Strain-induced transformation kinetics of the 1.5Al steels.....	128
Figure 6.4	Comparison of incremental strain hardening coefficients.....	132
Figure 6.5	Evolution of back stresses vs. square root of true strain.....	135
Figure 6.6	$\ln(d\sigma/d\varepsilon)$ vs. $\ln\sigma$ plots of the 1.0Al steels.....	143
Figure 6.7	$\ln(d\sigma/d\varepsilon)$ vs. $\ln\sigma$ plots of the 1.5Al steels.....	144

LIST OF TABLES

Table 2.1	Properties of conventionally-processed TRIP-assisted steels containing Al.....	26
Table 2.2	Property parameters of the plain carbon steels used by Uko (1978).....	38
Table 4.1	Chemical compositions of as-received steels (wt.%).....	48
Table 4.2	The designation of heat treated steels and their parameters.....	52
Table 5.1	The carbon content of retained austenite (RA)	77
Table 5.2	The dimensions of retained austenite.....	78
Table 5.3	Average yield strength, UTS, ϵ_u , and $UTS \times \epsilon_u$ of the experimental steels	80
Table 6.1	The fitted values of α and β parameters for the volume fraction of retained austenite (Figure 5.12).....	126
Table 6.2	Strains at which the back stresses deviated from $\epsilon^{1/2}$ linearity.....	137
Table 6.3	Property parameters at the transition points of the 1.5Al steels.....	143

CHAPTER 1: INTRODUCTION

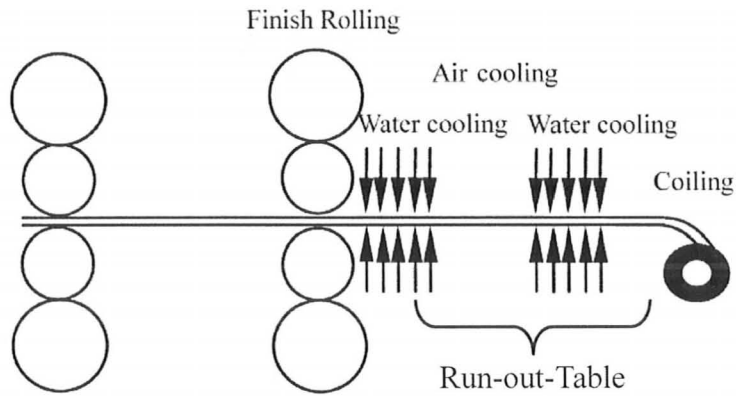
The development of high-strength steels for the automotive industry is stimulated by the need to reduce vehicle weight in order to improve fuel efficiency while continually improving passenger safety. Higher strength steels allow reduced sheet thickness without losing component strength. It should be kept in mind that good formability must not be sacrificed while improving the strength of steels. Thus, an optimum balance between strength and formability is always desirable for the automotive industry. Compared with other steels such as interstitial free, bake hardening, dual phase, and martensitic steels, TRIP-assisted steels seem to well meet the requirement.

1.1 TRIP-assisted Steels

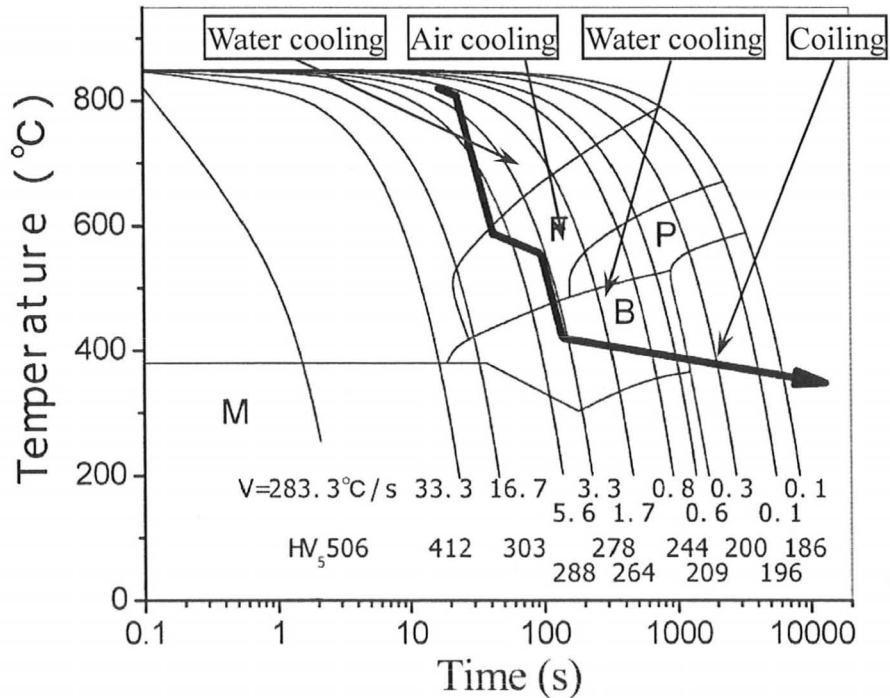
The acronym, TRIP, which stands for transformation-induced plasticity, was first introduced by Zackay et al. (1967) to highlight the fact that plasticity can be enhanced by the austenite-to-martensite transformation that takes place during the straining of some austenitic stainless steels. Bhadeshia and Honeycombe (2006) reserved the term “TRIP-

assisted” for steels in which the austenite (more precisely metastable retained austenite) is a minor phase in the overall microstructure and undergoes martensitic transformation during deformation. TRIP-assisted steels are usually low alloy steels. These steels contain a multiphase microstructure of a ferrite matrix, bainitic ferrite, retained austenite and possibly martensite. Retained austenite is obtained through an isothermal bainitic transformation, where precipitation of carbides is suppressed by using alloying element additions such as Si [Matsumura et al. (1987)] or Al [Mahieu et al. (2002a), Jacques et al. (2001a), De Meyer et al. (1999a)].

There are two kinds of TRIP-assisted steels, which undergo different thermo-mechanical processing routes. One is hot rolled and the other one is cold rolled. Hot rolled TRIP-assisted steels start from hot-rolled strips which are fully austenitic. After finish rolling, hot strips going through a run-out table (ROT) are cooled using controlled cooling processes and coiled at a controlled temperature to obtain the desired multiphase microstructure. Figure 1.1 a) is an illustration of the cooling and coiling processes for a 0.233C-1.540Mn-1.365Si (wt.%) hot-rolled TRIP-assisted steel; the cooling and coiling processes are superimposed on a CCT diagram in Figure 1.1 b) to illustrate the phase transformations taking place during processing [Wu and Li (2006)]. In this case, a three-stage cooling process is utilized to bring the sheet to the coiling temperature of ~ 400 °C. The first water cooling avoids relaxation after deformation and retains a high



a) Controlled cooling and coiling processes



b) controlled cooling processes superimposed on a CCT diagram

Figure 1.1 Schematic illustration of thermomechanical controlled processing (TMCP) of hot-rolled TRIP-assisted steels [Wu and Li (2006)]

dislocation density in austenite. The subsequent air cooling allows the formation of polygonal ferrite, and, simultaneously, the carbon concentration in the remaining austenite is enhanced. The second water cooling stage is needed to avoid pearlite formation. The final step is coiling and leads to bainitic transformation and further carbon enrichment of the remaining austenite, which is retained at room temperature. Hot-rolling can only be used to produce strip down to a gauge of 3 mm. Cold-rolling, on the other hand, is routinely used to produce thinner-gauge strip. The processing of cold-rolled TRIP-assisted steels is a two-stage (intercritical annealing and isothermal bainitic transformation) heat treatment route. Producing cold-rolled TRIP-assisted steels is one task of the present research work. The thermal processing route will be explained in detail in Chapter 2.

1.2 Galvanizing of TRIP-assisted Steels

The use of thinner gauge strips requires that steels must be corrosion resistant in order to retain their mechanical properties. Zinc coatings are predominantly used to protect steels against corrosion. Typical processing methods used to produce zinc coatings include hot-dip galvanizing, thermal spraying and electrodeposition. Hot-dip galvanizing can be conducted through a batch process or a continuous process. The continuous process is more advantageous for coiled steel strips.

The structure of a zinc coated steel consists of 1) the overlay or coating alloy, 2) an inter-facial layer between the overlay and the substrate steel, and 3) the substrate steel. The interfacial layer, termed inhibition layer, is essential in inhibiting the formation of Fe-Zn intermetallics, which are brittle. To produce a ductile coating, low Al additions (0.1 ~ 0.3wt.%) to molten zinc are used in order to form the continuous inhibition layer of $\text{Fe}_2\text{Al}_5\text{Zn}_x$ (η) [Marder (2000)]. Before the formation of the inhibition layer, molten zinc must wet the steel surface. However, this can be obstructed by the oxides of Mn and Si, commonly used as alloying elements of TRIP-assisted steels [Mahieu et al. (2002b) and (2001)]. It was shown that the wettability of the steel surface can be improved when substituting Al partially or completely for Si [Bellhouse and McDermid (2008), Bellhouse et al. (2007), Mahieu et al. (2002b)].

Another problem when galvanizing TRIP-assisted steels is that current continuous galvanizing lines are usually not compatible with the thermal processing routes of TRIP-assisted steels. The important work attempting to produce TRIP-assisted steels with desirable mechanical properties using heat treatment routes compatible with the continuous galvanizing process has been done by Bellhouse and McDermid (2007) and Mertens and McDermid (2005). The compatibility between the continuous galvanizing and processing of galvanizable TRIP-assisted steels will be reviewed in detail in Chapter 2.

CHAPTER 2: LITERATURE REVIEW

2.1 Processing of TRIP-assisted Steels

This section focuses on the processing of cold-rolled TRIP-assisted steels, of which the initial microstructure consists of deformed proeutectoid ferrite and pearlite. Proeutectoid ferrite is the ferrite coming from prior austenite during cooling from the austenite or austenite-ferrite phase fields. The processing route comprises two stages: Stage I - Intercritical Annealing (IA) and Stage II - Isothermal Bainitic Transformation (IBT) (Figure 2.1).

In Stage I, the steel is annealed at a temperature between the A_{C1} and A_{C3} to form a two-phase microstructure of ferrite and austenite. The steel is then quenched to a lower temperature (Stage II), where some of the intercritical austenite transforms to bainitic ferrite. Simultaneously, the remaining austenite is enriched with carbon and as a result it is retained to room temperature after subsequent quenching. Details of the microstructural evolution during these two key stages will be given in §2.1.1 and §2.1.2. In addition, the effects of alloying elements on the both processing stages will be discussed.

Particular emphasis is placed on the effect of Al as it has been used to obtain the galvanizable TRIP-assisted steels used in the present research work [Bellhouse and McDermid (2008), Bellhouse and McDermid (2007), Bellhouse et al. (2007)].

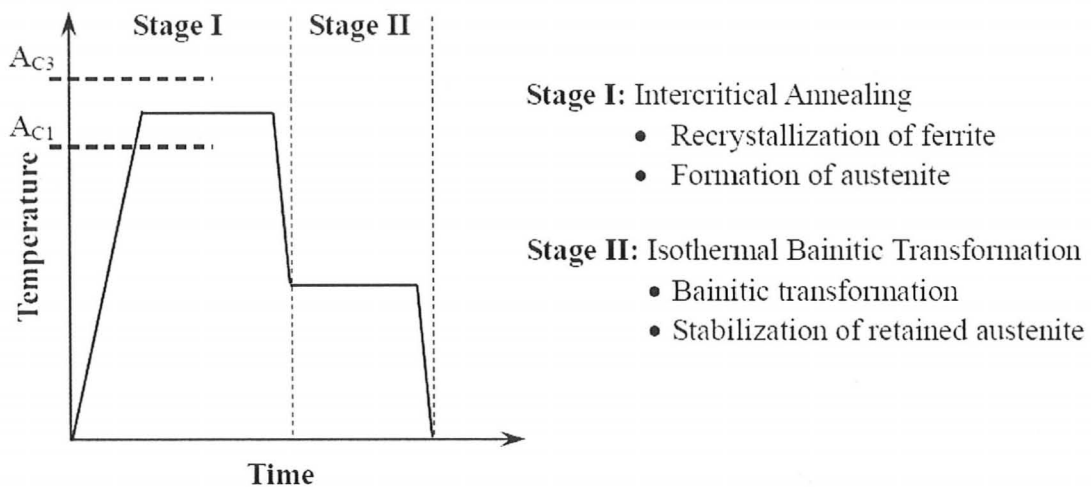


Figure 2.1 Schematic two-stage processing of cold-rolled TRIP-assisted steels

2.1.1 Intercritical Annealing

The objective of intercritical annealing is to obtain intercritical austenite. Its amount can be controlled by the selection of annealing temperature; the higher the annealing temperature, the larger the amount of austenite. In previous work, the amount of intercritical austenite was frequently selected between 30 - 60% [e.g. Lee et al. (2004), Mahieu et al. (2002a), Jacques et al. (2001a), Kim et al. (2001)]. The intercritical

annealing temperature needs to be uniquely determined for each steel since the composition of the steel affects A_{C1} and A_{C3} . It was shown that Al additions not only increase A_{C1} and A_{C3} but also expand the two-phase region [De Meyer et al. (1999a), Garcia- Gonzalez (2005)]. As a result, a higher intercritical annealing temperature is required for Al-alloyed TRIP-assisted steels.

Samajdar et al. (1998) found that, during intercritical annealing of TRIP-assisted steels, austenite nucleates within pearlite colonies. This transformation includes two steps, which are the spheroidization of cementite and the nucleation and growth of austenite from the spheroidized cementite particles. This process occurs rapidly leading to complete pearlite dissolution [Speich et al. (1981)]. Subsequently, austenite may nucleate and form at ferrite grain boundaries.

In addition to the formation of austenite, recrystallization of proeutectoid ferrite also takes place during intercritical annealing [Garcia-Gonzalez (2005), Huang et al. (2004), Samajdar et al. (1998)]. The process of recrystallization replaces deformed proeutectoid ferrite grains with equiaxed grains. The driving force of recrystallization is the energy stored in the steel due to cold rolling. Upon annealing, the stored energy is released by recrystallization [Huang et al. (2004)]. It was shown that ferrite recrystallization is rapid and usually starts during heating to the intercritical annealing temperature. In the work of Garcia-Gonzalez (2005), the intercritical annealing

temperature did not affect the percentage of recrystallized ferrite too significantly, but it was affected by the steel composition. When a lower-Al steel (0.15C-1.52Mn-0.31Si-0.051Al (wt.%) and a higher-Al steel (0.15C-1.52Mn-0.31Si-1.0Al (wt.%) were both intercritically annealed to produce 35% and 55% austenite (i.e. 65% and 45% ferrite), respectively, it was shown that 55% of the ferrite had recrystallized in the lower-Al steel for the both intercritical annealing temperatures, compared to a recrystallized fraction of 75% in the higher-Al steel for the both annealing temperatures. This implies that Al additions encourage ferrite recrystallization. Garcia-Gonzalez (2005) also found that there was a relation between austenite formation and ferrite recrystallization. The rate of austenite formation from unrecrystallized ferrite is very rapid, and decreased once ferrite recrystallization was completed. Huang et al. (2004) stated that ferrite recrystallization interacts strongly with austenite formation, and this interaction affects not only the kinetics of austenite formation but also the spatial distribution and morphology of austenite.

Following intercritical annealing, “new” ferrite grains may form upon quenching to the lower isothermal bainitic transformation temperature. Figure 2.2 shows a CCT diagram for a steel which was intercritically annealed at 770°C, where 35% austenite was produced. It is clear that ferrite formation begins immediately upon cooling from the intercritical annealing temperature. Such ferrite formation has also been reported else-

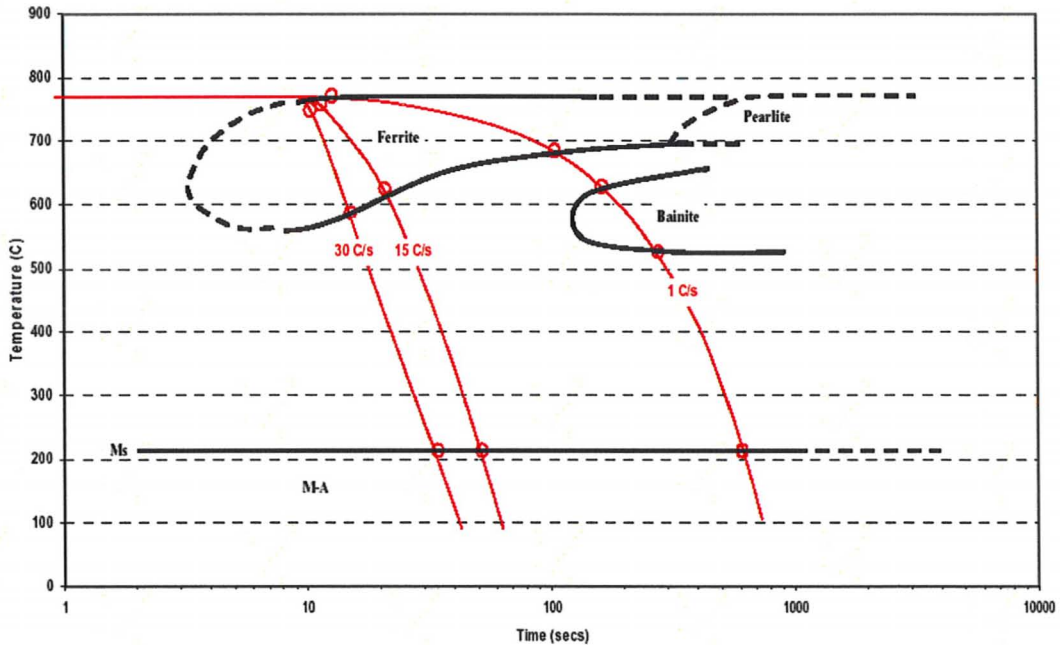


Figure 2.2 CCT diagram from $T_{\text{Intercritical Annealing}} = 770^{\circ}\text{C}$ (35% intercritical austenite), Steel composition: 0.15C-1.52Mn-0.31Si-1.0Al (wt.%) [Garcia-Gonzalez (2005)]

where [Suh et al. (2007), Huang et al. (2004), Lee et al. (2004), Kim et al. (2001), Minote et al. (1996)], and was occasionally referred to as intercritical ferrite growth. It is worth noting that, accompanying the formation of “new” ferrite, carbon is rejected to untransformed austenite, and thus causes carbon enrichment of the remaining austenite. Al has been observed to increase the formation of “new” ferrite [Garcia-Gonzalez (2005), Suh et al. (2007)]. In the work of Suh et al. (2007), it was shown that as much as 50% of the intercritical austenite transformed to ferrite when a 0.15C-1.47Mn-0.30Si-0.98Al (wt.%) steel was cooled at a rate of 20°C/s to a bainitic transformation temperature of 450°C .

This ferrite formation can be avoided using a very high cooling rate. For example, a cooling rate of 120°C/s was necessary to avoid significant transformation of intercritical austenite to ferrite for a 1.2wt.%Mn steel and 50°C/s was required in the case of a 2.4wt.%Mn steel [Garcia-Gonzalez (2005), Brandt (1997)].

2.1.2 Isothermal Bainitic Transformation

Following Intercritical Annealing (Stage I), TRIP-assisted steels are usually quenched to a lower temperature where the Isothermal Bainitic Transformation (IBT) takes place (Stage II). During Stage II, the remaining austenite starts to transform to bainitic ferrite without carbide formation. Conventionally, the isothermal bainitic transformation temperature was selected around 400 °C [De Cooman (2004)].

Different transformation mechanisms have been proposed for the isothermal bainitic transformation of TRIP-assisted steels. These are 1) displacive or diffusionless, 2) diffusional and 3) coupled diffusional/displacive mechanisms. Several investigators [Gaude-Fugarolas and Jacques (2006), Jacques (2004), Jacques et al. (1999), Girault et al. (1999)] have extensively investigated the isothermal bainitic transformation and suggested that the majority of experimental observations can be interpreted in terms of the displacive mechanism postulated by Bhadeshia and Edmonds (1980). It states that the bainite reaction involves repeated nucleation and growth of small sub-units of super-

saturated bainitic ferrite, and partitioning of carbon occurs only after the growth stops. Carbon can either form a distribution of carbides or redistribute into the surrounding untransformed austenite. The bainite reaction is therefore a nucleation-controlled transformation. The process is schematically shown in Figure 2.3. Diffusionless growth requires that transformation occurs at a temperature below T_0 , where the free energy of bainite is less than that of austenite of the same composition. A locus of the T_0 temperature as a function of carbon concentration forms the T_0 curve, which is shown in Figure 2.4. In this figure, austenite with a carbon concentration to the left of the T_0 boundary can transform without any diffusion; diffusionless transformation is thermodynamically impossible if the austenite carbon concentration exceeds the T_0 curve.

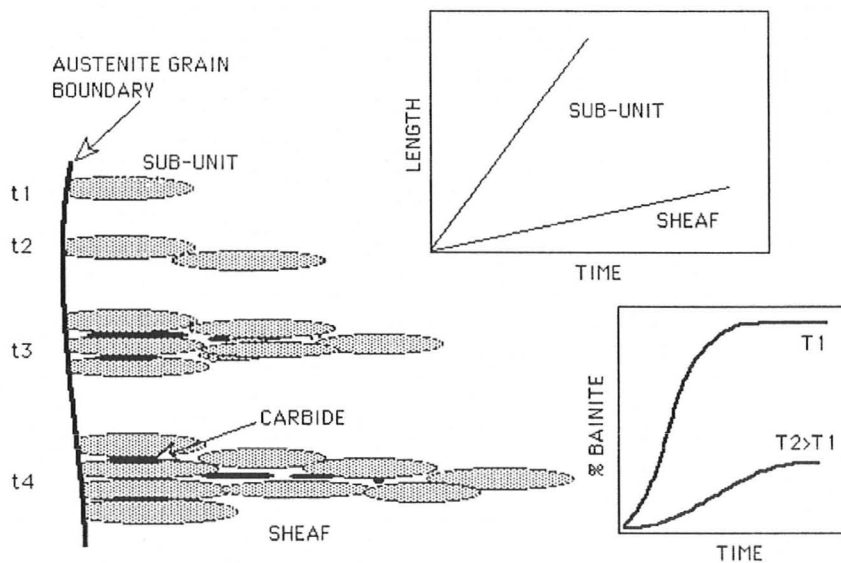


Figure 2.3 Schematic illustration of the microstructural features relevant in the kinetic description of a bainitic microstructure [Bhadeshia (2001)]

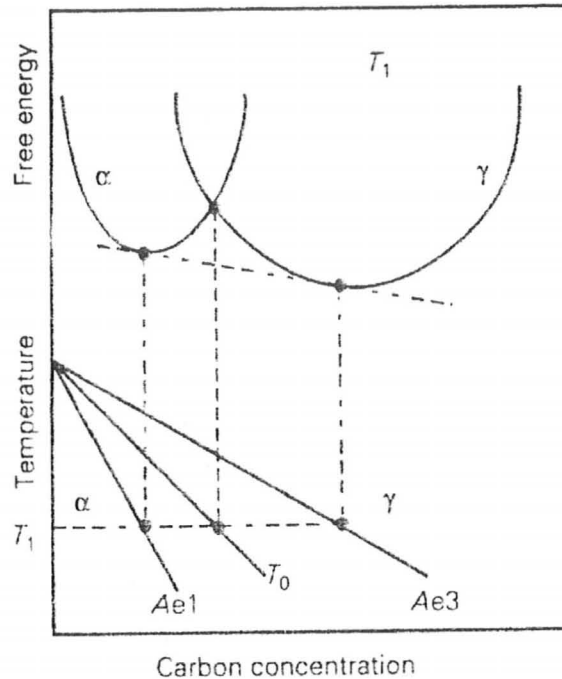


Figure 2.4 Schematic illustration of the origin of the T_0 construction on the Fe-C phase diagram [Bhadeshia and Honeycombe (2006)]

In the particular case of TRIP-assisted steels, bainitic transformation kinetics are different in at least two ways from the above description. The first is that the relatively small austenite grain size limits the repeated nucleation of sub-units (the autocatalytic effect). The second is that the precipitation of carbides must be suppressed in order to reject as much carbon as possible into the surrounding austenite to chemically stabilize it.

Jacques (2004) proposed that a small intercritical austenite grain size on the order of a few microns inhibits the autocatalytic nucleation of sub-units which was described

earlier [Bhadeshia and Edmonds (1980)]. In the case of the bainitic transformation in TRIP-assisted steels and due to the small grain size, bainite sub-units can only nucleate as parallel platelets that completely cross the austenite grain. To make this clear, the two nucleation mechanisms are schematically compared in Figure 2.5. It is evident that the much larger grain boundary area resulting from small grains promotes sub-unit nucleation. As a result, the bainitic transformation from fine-grained austenite starts earlier but proceeds at a slower rate [Jacques (2004)].

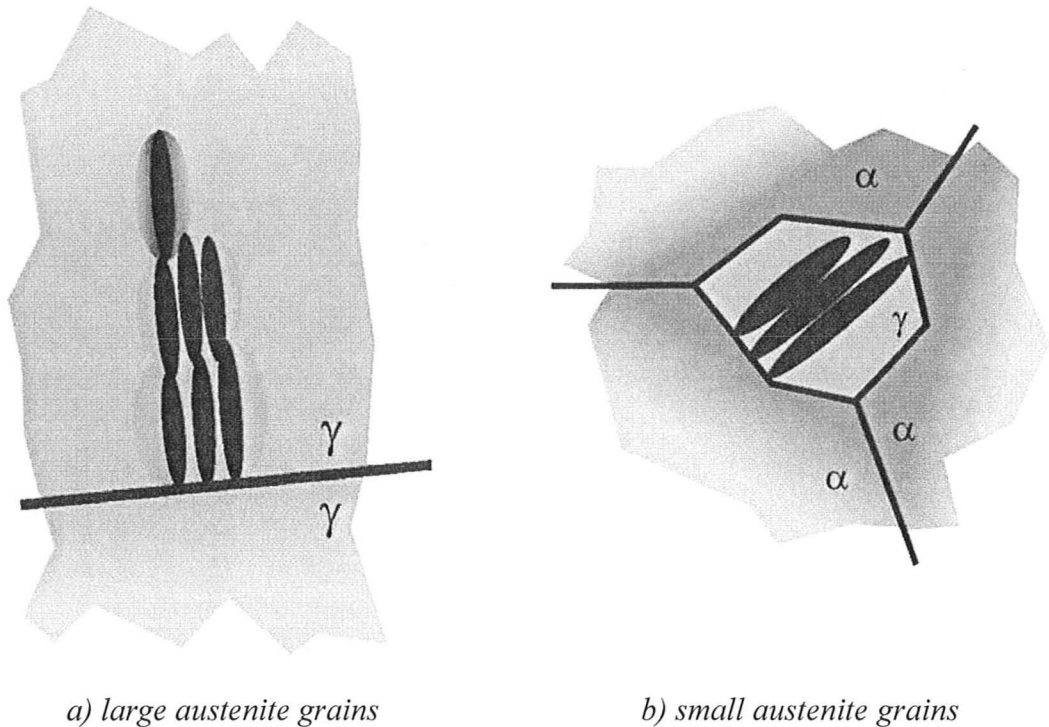


Figure 2.5 Schematic illustration of two bainite growth mechanisms [Jacques (2004)]

The kinetics of bainitic transformation in TRIP-assisted steels is dependent on the hold temperature [Mertens et al. (2003), Girault et al. (1999), Jacques et al. (1999)]. Figure 2.6 shows that a higher hold temperature increases the rate of bainitic transformation. Jacques et al. (1999) and Girault et al. (1999) attributed this effect to the unique nucleation mechanism within fine-grained austenite. To understand this, it is important to realize that the initial nucleation of bainite sub-units gives rise to heterogeneous carbon distribution in the small austenite grain and this restricts the opportunity for the nucleation of the next sub-units. The build-up of carbon near bainite/austenite interfaces persists more significantly at a lower holding temperature, and hinders further bainite reaction. At a higher temperature, the heterogeneity of carbon distribution is released due to the thermal activation of carbon diffusion, and thus the global transformation kinetics appear faster.

The isothermal bainitic transformation temperature also affects the carbon content of the retained austenite. It was previously mentioned that further transformation is impossible when the austenite carbon concentration reaches the T_0 curve. Figure 2.7 shows that the phase transformation terminates earlier at a higher holding temperature and leads to a lower carbon content in retained austenite. This is not desirable because the lower carbon content makes the final retained austenite less resistant to the transformation to martensite upon quenching or plastic deformation.

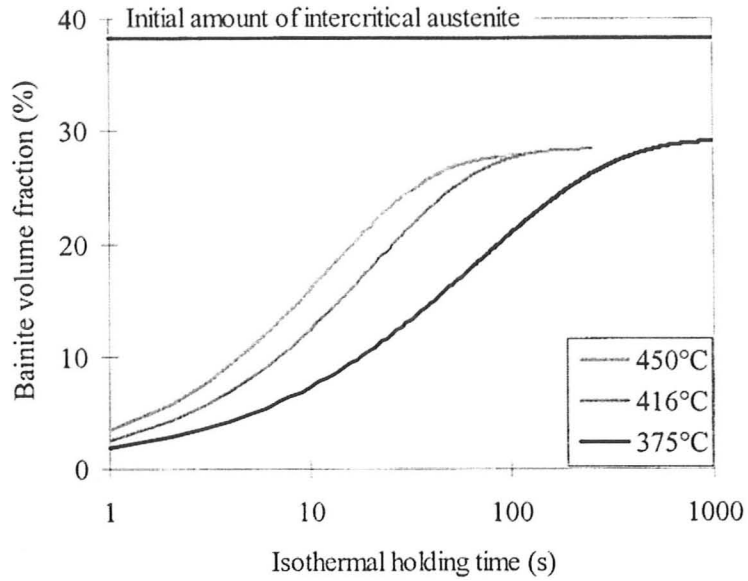


Figure 2.6 Bainitic transformation kinetics showing the effect of hold temperatures (Steel: 0.11C-1.53Mn-1.50Si (wt.%) [Girault et al. (1999)]

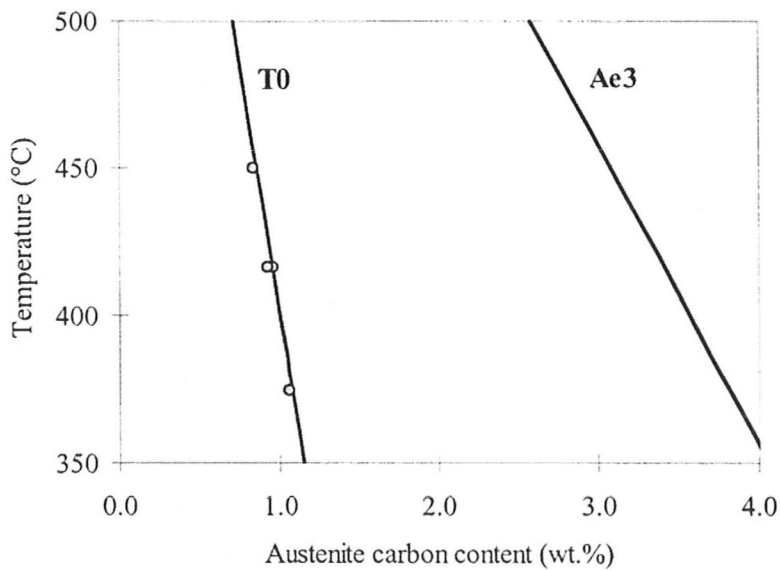


Figure 2.7 Ultimate austenite carbon contents affected by holding temperatures (dots) (Steel composition: 0.11C-1.53Mn-1.50Si (wt.%) [Girault et al. (1999)]

It should be noted that, in addition to the isothermal bainitic transformation temperature, the hold time at this temperature also affects the ultimate retained austenite carbon content. Figure 2.8 clearly shows that, in case of a lower holding temperature, a higher carbon content can be obtained only if the hold time is long enough. If the hold time is not sufficient, the carbon content in austenite can not reach the T_0 line. A more important consequence shown by Figure 2.8 is that precipitation of carbides occurs more easily at a higher holding temperature, which significantly decreases the carbon content in retained austenite and must be avoided in processing TRIP-assisted steels. Traint et al. (2002) reported that carbides started to precipitate between 450 ~ 475 °C and this temperature range was not significantly affected by the composition of steels.

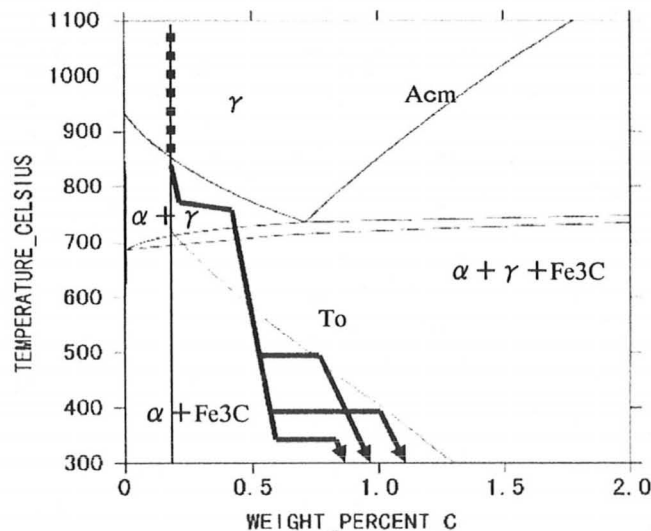


Figure 2.8 Equilibrium phase diagram calculated using ThermoCalc® schematically showing the carbon concentration process in austenite (Steel composition: 0.21C-1.45M-1.49Si (wt.%)) [Hashimoto et al. (2004)]

The suppression of carbide precipitation in TRIP-assisted steels is achieved by using various alloying elements. These elements can be Si, Al, P or Cu. The mechanism by which these elements suppress carbide precipitation might be that these elements are not soluble in carbides [Thelning (1984)]. Si is an alloying element conventionally used in TRIP-assisted steels as it also imparts a significant solid solution hardening effect [Matsumura et al. (1987)], but its oxides often lead to poor quality zinc coatings [Mahieu et al. (2002b) and (2001)]. The principle reason for the use of Al is to improve the galvanizability of TRIP-assisted steels [Bellhouse and McDermid (2008), Bellhouse et al. (2007), Mahieu et al. (2002b)], which will be reviewed in detail in §2.1.3.

Most of studies indicated that Al additions enhanced the kinetics of bainitic transformation, as seen by comparing a 1.5Si steel with a 1.0Al steel (Figure 2.9) [Soliman and Palkowski (2008), Mertens et al. (2003), Mahieu et al. (2002a), Jacques et al. (2001a)]. Using ThermoCalc®, Soliman and Palkowski (2008) calculated the driving force of the transformation of austenite to ferrite ($\Delta G^{\gamma \rightarrow \alpha}$) for two steels with varying Al contents (Figure 2.10). It confirms that a higher Al content gives rise to faster bainitic transformation kinetics. It should be pointed out that, in the work of Soliman and Palkowski (2008), a cooling rate of 50 °C/s from intercritical annealing to isothermal bainitic transformation was used and their dilatometric experiments indicated that no ferrite formation occurred during the cooling. Mahieu et al. (2002a) and Jacques et al.

(2001a) used cooling rates of 50 °C/s and 70 °C/s, respectively, and they also did not report the ferrite formation during the cooling from intercritical annealing to isothermal bainitic transformation. Mertens et al. (2003) did not report the cooling rates in their work. It was mentioned in §2.1.1 that ferrite formation can occur during quenching from intercritical annealing to isothermal bainitic transformation, leading to carbon enrichment of the remaining austenite before the start of bainitic transformation. In this case, the kinetics of isothermal bainitic transformation could be changed by ferrite formation.

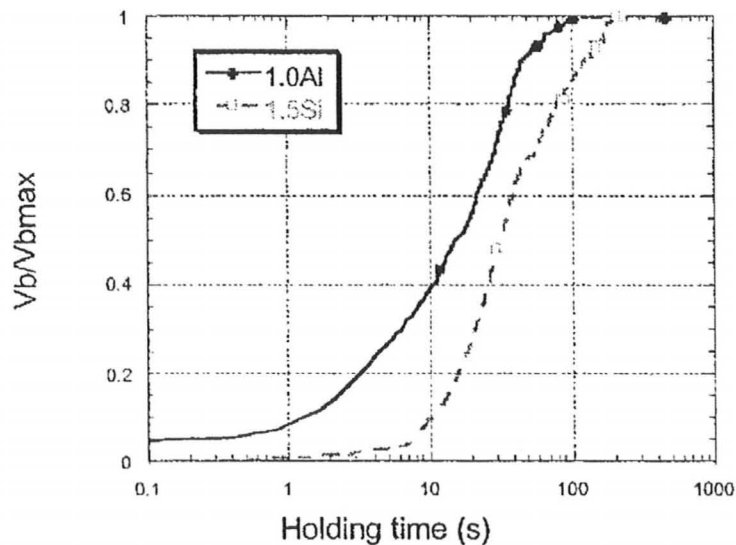


Figure 2.9 Effect of Al on bainitic transformation kinetics at 410°C (1.0Al: 0.12C-1.5Mn-1.0Al (wt.%), 1.5Si: 0.15C-1.5Mn-1.5Si (wt.%)) [Mertens et al. (2003)]

ThermoCalc® calculations also indicated that a higher Al content moved the T_0 line to right (Figure 2.11) [Soliman and Palkowski (2008)], which implies that retained

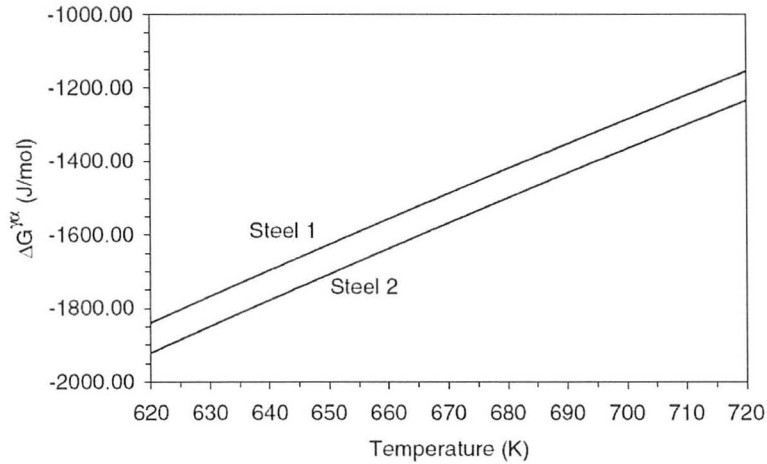


Figure 2.10 Calculated driving force of transformation from austenite to ferrite (Steel 1: 0.278C-1.48Mn-0.852Si-0.228Al (wt.%), Steel 2: 0.254C-1.37Mn-0.869Si-0.643Al (wt.%)) [Soliman and Palkowski (2008)]

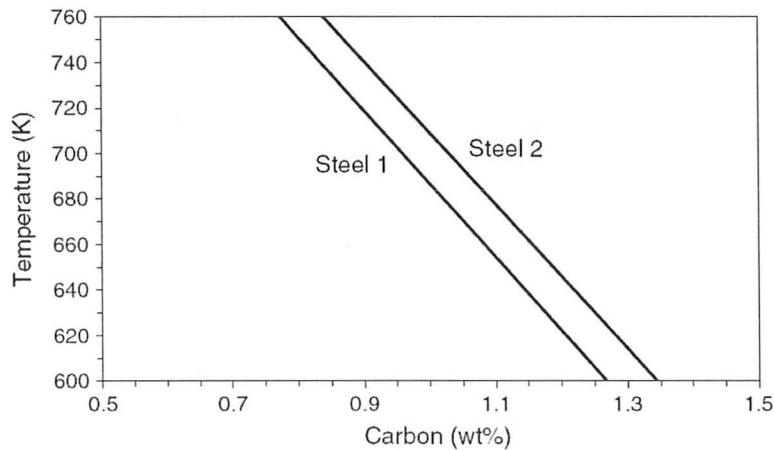


Figure 2.11 Calculated T_0 curves showing the effect of Al additions (Steel 1: 0.278C-1.48Mn-0.852Si-0.228Al (wt.%), Steel 2: 0.254C-1.37Mn-0.869Si-0.643Al (wt.%)) [Soliman and Palkowski (2008)]

austenite in a higher-Al alloyed TRIP-assisted steel is able to obtain a higher carbon

content in the case of a proper bainitic transformation hold time. It can be seen that the combined effects of faster bainitic transformation kinetics and a right-shifted T_0 line due to Al additions can make the isothermal bainitic transformation of Al-alloyed TRIP-assisted steels very different from that of Si-alloyed TRIP-assisted steels.

Kim et al. (2001) and Brandt (1997) showed that bainitic transformation does not take place immediately upon the steel being quenched to the isothermal bainitic transformation temperature, which can also be seen in Figure 2.9. An incubation time exists between the initial hold and the start of bainite formation. In the work of Brandt (1997), a 0.26C-1.22Mn-1.58Si-0.05Al (wt.%) steel exhibited an incubation time of 40 s. Ghosh and Olson (2001) stated that two things are happening during the incubation time. The first is the continuation of ferrite formation that starts upon quenching from the inter-critical annealing to isothermal bainitic transformation temperatures; the second is the homogenization of carbon distribution within ferrite and austenite.

2.1.3 Compatibility between Thermal Processing of TRIP-assisted Steels and Continuous Galvanizing

The conventional thermal processing route of cold-rolled TRIP-assisted steels has been discussed in the last two sub-sections. It was mentioned, in Chapter 1, that the continuous galvanizing process, compared with the batch process, is more advantageous in hot-dip galvanizing of coiled steel strips. The issues when combining the conventional

thermal processing route of cold-rolled TRIP-assisted steels and a continuous galvanizing line, as well as the important work that has been done, will be reviewed in this subsection, starting with a brief description of the continuous galvanizing process.

Most of current continuous galvanizing lines comprise cleaning, continuous annealing, hot-dipping, and subsequent cooling or galvannealing processes [Marder (2000)]. Before thermal processing, the steel strip is usually cleaned using sodium hydroxide (NaOH) with concentrations varying from 1.5 to 2.5% to remove rolling oils, loose soils, surface carbon and iron fines. The cleaning section is then followed by a continuous annealing section which performs two functions - deoxidation of the steel surface and thermal processing of the steel to obtain the desired properties. A N_2/H_2 reducing atmosphere at about 500-760 °C is used during annealing to further remove residual organic contaminants and reduce surface oxides, which make the strip surface difficult to be wetted by molten zinc. Annealing atmospheres are usually composed of 5-20vol.% H_2 (balance N_2) with a controlled water vapour content to control the oxygen partial pressure. On exiting the annealing furnaces, through a gas jet section, the steel strip is cooled down to a temperature suitable for subsequent immersion into the molten zinc bath. The zinc bath temperature, depending on the bath composition, is usually about 450~470 °C. A typical dipping time is around 4 seconds. Upon exiting the zinc pot, the excess liquid metal is forced backed into the bath by gas wiping dies, which are

designed to precisely control and maintain a uniform coating thickness. After galvanizing, the steel strip moves up to a cooling tower where the coating is cooled down, or is transformed to an annealing furnace for galvannealing. To combine the current continuous galvanizing line with the thermal processing route of cold-rolled TRIP-assisted steels, at least two issues must be solved.

First, the current continuous galvanizing line usually does not have an isothermal holding process suitable for bainitic transformation of TRIP-assisted steels (Stage II in Figure 2.1). As already mentioned, this stage is conventionally conducted at ~ 400 °C [De Cooman (2004)]. Nevertheless, this temperature must be changed to the zinc bath temperature, which is about $450 \sim 470$ °C, to make the processing route compatible with the galvanizing line. The much higher bainitic transformation temperature gives rise to faster bainitic transformation kinetics, a lower carbon content of the retained austenite, and more chance for the decomposition of retained austenite to ferrite and carbides, as discussed in §2.1.2. Carbide precipitation results in both a low amount of retained austenite and a low carbon content of the retained austenite, which is not desirable in producing TRIP-assisted steels.

Second, the reducing atmosphere used in the current continuous galvanizing line (the mixture of N_2 and H_2) is reducing for iron oxides but not for the oxides of Mn, Si and Al. Mahieu et al. (2002b) and (2001) showed that a large amount of Mn_2SiO_4 formed

on the steel surface while galvanizing a conventional C-Mn-Si TRIP-assisted steel. This oxide was unable to be reduced by the atmosphere of 95vol.% N₂ + 5vol.% H₂ (dew point: -30 °C) and hindered molten zinc wetting the steel surface. It was shown that the wettability of the steel surface was improved when Al was substituted partially or completely for Si [Mahieu et al. (2002b)]. Bellhouse et al. (2007) investigated the galvanizability of the 0.23C-1.52Mn-0.55Si-1.05Al (wt.%) and 0.20C- 1.55Mn-1.52Al (wt.%) steels, which are also the research objectives of the present work, and showed that, despite the presence of some oxides, good reactive wetting occurred during galvanizing in a zinc bath containing effective 0.2wt.% Al using the atmospheres of 95vol.% N₂ + 5vol.% H₂ (dew point: -30 °C) and 80vol.% N₂ + 20vol.% H₂ (dew point: -53 °C). It was also shown that Mn and Si tended to be oxidized externally and Al tended to be oxidized internally. MnO, Al₂O₃, MnAl₂O₄ and Mn₂SiO₄ were identified on the 0.23C-1.52Mn-0.55Si-1.05Al (wt.%) steel surface immediately prior to galvanizing; MnO, Al₂O₃, and MnAl₂O₄ were identified on the 0.20C-1.55Mn-0.025Si-1.52Al (wt.%) steel surface immediately prior to galvanizing. After galvanizing [Bellhouse and McDermid (2008)], the formed inhibition layer contained a mixture of Fe₂Al₅ and FeAl₃. It was pointed out that the oxide-containing surface was able to be wetted due to two mechanisms. First, when Mn was in the form of MnO, the oxide was reduced by Al in the zinc bath. Second, when Mn was in the form of Mn₂SiO₄, Zn bridging of the oxide particles occurred. The

presence of Al_2O_3 was not observed to be detrimental to the reactive wetting.

As previously discussed, Al additions affect both intercritical annealing and isothermal bainitic transformation during the thermal processing, resulting in 1) encouragement of ferrite formation, 2) faster bainitic transformation kinetics and 3) right-shifted T_0 line. Furthermore, Al is not as a good solid solution strengthener as Si [Jacques et al. (2001a)].

Using thermal processing routes compatible with the continuous galvanizing process, i.e. the isothermal bainitic transformation temperature was selected at 465 °C, which are called galvanizing heat treatments in this thesis, Mertens and McDermid (2005) and Bellhouse and McDermid (2007) investigated the optimum thermal processing parameters for a series of Si-Al alloyed TRIP-assisted steels, where Al was substituted for Si in intervals of 0.5wt.% such that the total Al + Si content of the steel was maintained at 1.5wt.%. It was shown that, although it was difficult to obtain the desired retained austenite in the Si-alloyed steel, a certain amount of retained austenite was obtained with substitution of Si by Al. Especially, approximately 10 ~ 15vol.% retained austenite was achieved in the 0.23C-1.52Mn-0.55Si-1.05Al (wt.%) and 0.20C-1.55Mn-1.52Al (wt.%) steels [Bellhouse and McDermid (2007)]. The true ultimate tensile strength (UTS) and uniform elongation (ϵ_u) were approximately 1,000 MPa and 0.20, respectively, for the 0.23C-1.52Mn-0.55Si-1.05Al (wt.%) steel. These values were about

800 MPa and 0.25, respectively, for the 0.20C-1.55Mn-1.52Al (wt.%) steel. These properties are comparable with those of other Al-alloyed TRIP-assisted steels obtained through conventional thermal processing routes, which are shown in Table 2.1.

Table 2.1 Properties of conventionally-processed TRIP-assisted steels containing Al

Steel (wt.%)	Isothermal Bainite Trans- formation Temperature	UTS / ϵ_u	Source
0.11C-1.55Mn- 0.059Si-1.5Al	370 ~ 430 °C	700 MPa/0.22	Jacques et al. (2001a)
0.183C-1.56Mn- 0.02Si-1.73Al	400°C	633 MPa/0.24	Mahieu et al. (2002a)
0.31C-1.57Mn- 0.34Si-1.23Al	400°C	~ 850 MPa	De Meyer et al. (1999a)

This indicates possibility of producing TRIP-assisted steels using galvanizing heat treatments, which have properties comparable to conventionally processed alloys.

Combining the thermal processing and continuous galvanizing of TRIP-assisted steels appears promising when Al alloying element is used.

2.2 Strain Hardening of TRIP-assisted Steels

The superior combination of strength and ductility exhibited by TRIP-assisted steels is traditionally attributed to two mechanisms that dynamically enhance the sustainability of the work hardening rate ($d\sigma/d\varepsilon$) of the steels. In other words, the enhanced $d\sigma/d\varepsilon$ can be sustained until high strains. The two mechanisms are 1) the TRIP effect and 2) the composite strengthening effect [Jacques (2004)]. A third hardening mechanism, which is rarely reported in the literature, is kinematic hardening. All three mechanisms are reviewed in detail below.

2.2.1 TRIP Effect

In TRIP-assisted steels, deformation results in the gradual conversion of retained austenite into martensite. Jacques et al. (2001b) proposed that, due to the shape change and volume expansion accompanying the transformation from retained austenite to martensite, extra dislocations are generated in the surrounding ferrite in addition to the dislocations associated with normal strain hardening. The extra dislocations improve the local strength of the ferrite grains. Figure 2.12 is a TEM micrograph showing the dislocations generated in the surrounding ferrite. Through a theoretical calculation based

on the elastic-plastic analysis of Hill (1950), Jacques et al. (2001b) showed a correspondence between the strain-induced transformation rate and the strength-ductility balance of TRIP-assisted steels.

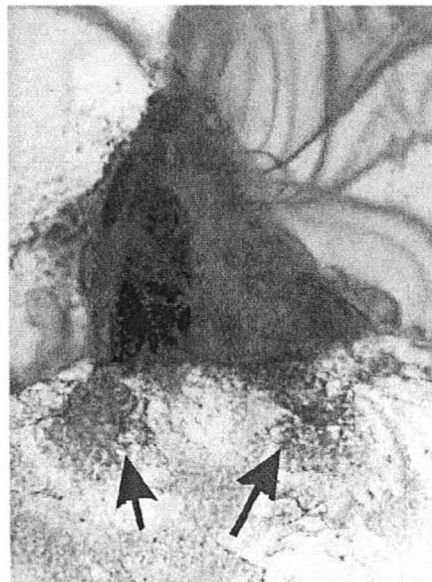


Figure 2.12 TEM micrograph illustrating the dislocations generated in ferrite at the tip of strain-induced martensitic variants [Jacques (2004)]

Perlade et al. (2003) proposed that the austenite phase is also strengthened due to the TRIP effect. The argument is that strain-induced martensitic plates (Figure 2.13) partition austenite grains, and this process decreases the dislocation mean free path. Since the amount of retained austenite decreases through strain-induced martensitic transformation, the contribution of such austenite strengthening is probably minor.

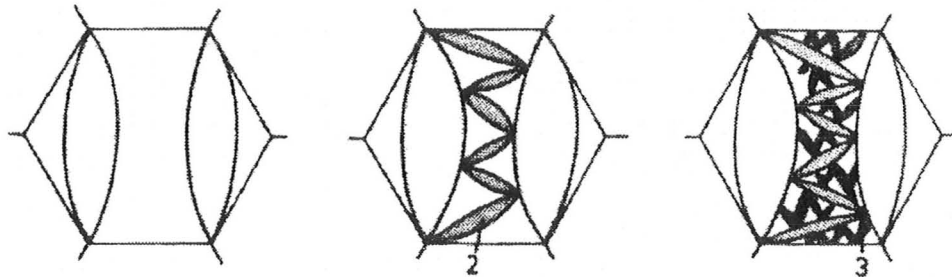


Figure 2.13 Schematic morphology evolution of strain-induced martensite [Perlade et al. (2003)]

2.2.2 Composite Strengthening Effect

It is clear that the microstructure of TRIP-assisted steels resembles that of a composite material. The yield strengths of ferrite, bainitic ferrite, austenite and martensite measured using neutron diffraction are about 500 MPa, 650 MPa, 900 MPa and 2000 MPa, respectively. As a result of the large variability of the strengths of the different phases, stress and strain partitioning takes place during loading and dictates the macroscopic stress-strain behaviour. In addition, the amounts of austenite and martensite continuously change during deformation, and this will dynamically modify the stress and strain partitioning. Based on the stresses carried on by the BCC (ferrite and bainitic ferrite) and FCC (retained austenite) phases, which were evaluated using neutron diffraction, Jacques (2004) calculated the global stress using the law of mixtures, equation (2.1), with the martensitic term excluded. When the calculated results were

compared to the measured macroscopic stress, a clear discrepancy was observed as shown by the shaded area in Figure 2.14. This discrepancy corresponds to the strengthening resulting from the continuously transformed martensite.

$$\sigma(\varepsilon) = f_{\alpha+\alpha_b} \sigma_{\alpha+\alpha_b}(\varepsilon) + f_{\gamma}(\varepsilon) \sigma_{\gamma}(\varepsilon) + f_{\alpha'}(\varepsilon) \sigma_{\alpha'}(\varepsilon) \quad (2.1)$$

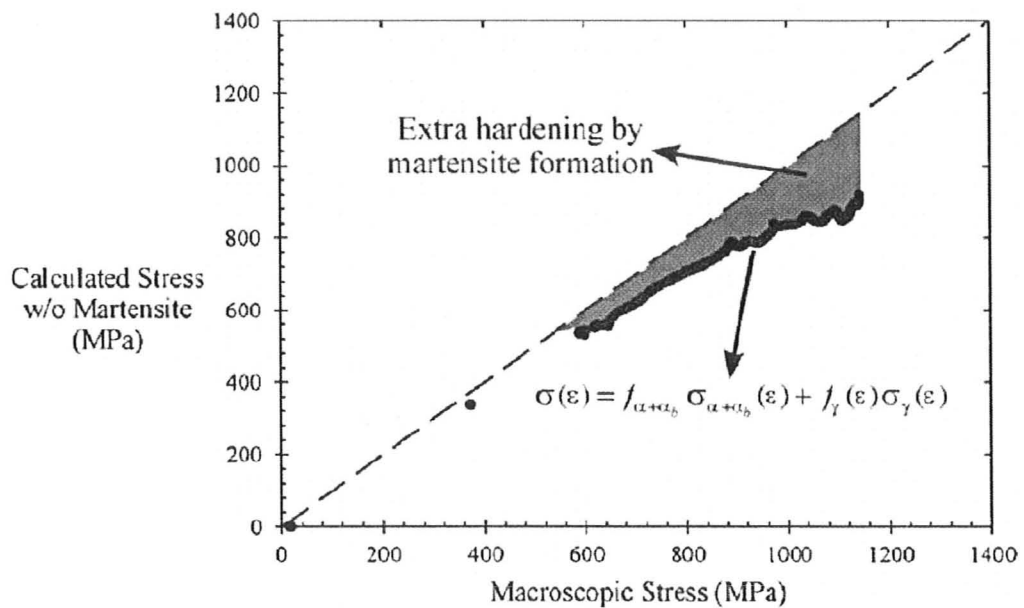


Figure 2.14 Comparison of the macroscopic stress and the stress calculated without taking into account the martensitic phase [Jacques (2004)]

It is worth noting that Bhadeshia (2002) argued that the excellent mechanical properties of TRIP-assisted steels are mainly due to the composite strengthening effect, and it is possible that the role of the TRIP effect has been exaggerated when calling these steels “TRIP-assisted” steels. Nonetheless, the strengthening contribution due to

martensite formation should not be ignored because martensite can comprise as much as 20% of the total microstructure. In addition, martensite formation may play an important role in enhancing the work hardening rate and delaying the onset of plastic instability, as will be discussed in §2.4.

2.3 Kinematic Hardening

Another hardening mechanism which is rarely reported for TRIP-assisted steels is “kinematic hardening”, due to the development of back stresses in a material. In this section, first a general review of the development and measurement of back stresses will be presented, and then some studies concerning kinematic hardening in “hard phase dispersed” steels will be summarized.

2.3.1 Development of Back Stresses

Figure 2.15 is a schematic diagram showing a system consisting of a soft matrix with hard particles. During plastic deformation of the system, the soft matrix plastically flows, but the hard particles do not. Thus, incompatible deformation between the matrix and hard particles occurs. When a dislocation by-passes the hard particle, it leaves a dislocation loop around the particle. As more and more dislocation loops pile up, the

result is unrelaxed strain surrounding the particle. As a result, internal stresses supported by the hard particle are produced in this area [Embury (1987), Brown and Stobbs (1971a)]. These stresses are referred to as back stresses. It should also be pointed out that dislocation loops can also disappear, causing plastic relaxation. This process of plastic relaxation relieves unrelaxed strain and reduces internal stresses.

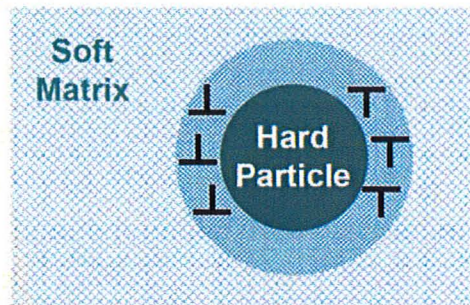


Figure 2.15 Schematic illustration showing the development of internal stresses due to incompatible deformation between hard particles and the soft matrix, adapted from Embury (1987)

Using an experimental material that comprised undeformable spherical silica particles in a soft copper matrix, Brown and Stobbs (1971b) showed that the value of unrelaxed strain linearly increases with the square root of the macroscopically imposed plastic strain provided that the plastic relaxation process around hard particles is not significant. Brown and Stobbs (1971b) also proposed a microscopic model describing the development of internal stresses, where the value of internal stresses linearly

increases with the volume fraction of hard particles and the square root of plastic strain:

$$\sigma_B = f\mu\varepsilon_p^* = \alpha f\mu \left(\frac{8b\varepsilon_p}{\pi r_0} \right)^{\frac{1}{2}} \quad (2.2)$$

where, σ_B is the internal stress, ε_p is the macroscopic plastic strain, ε_p^* is the unrelaxed strain, f is the volume fraction of hard particles, b is the burger's vector, μ is the shear modulus of the matrix, r_0 is the particle radius and α is a constant associated with the particle shape and size.

The internal stresses are directional in that they impede forward plastic flow, but aid reverse plastic flow, which is why they are also referred to as “back stresses”. Hereinafter, only the term “back stresses” will be used. Since these back stresses must be overcome during forward loading, they increase the forward flow stress. This contribution to the overall work hardening of a material is called kinematic hardening.

2.3.2 Measurement of Back Stresses

Back stresses in two-phase materials have been conventionally investigated using the Bauschinger test, which is schematically shown in Figure 2.16. The sample is loaded to a pre-set strain, unloaded, and then compressed to obtain both a forward flow curve and a reverse flow curve. To compare the forward curve and the reverse curve more easily, the reverse curve is usually reflected to the same quadrant as the forward flow

curve. By comparing the extrapolated flow curve (i.e. the flow curve if the loading was continued without interruption) and the reflected reverse curve, two important features can be observed [Orowan (1959)]:

- 1) part of the hardening in the forward direction is permanently removed in the reverse flow, which gives rise to a discrepancy between the forward flow curve and the reflected reverse flow curve, termed permanent softening ($\Delta\sigma$),
- 2) yielding during reverse flow is gradual, which means that the absolute value of the elastic limit is reduced in reverse flow. This reduction of the reverse elastic limit was termed transient softening. It is what was originally observed by Bauschinger, and named the Bauschinger effect.

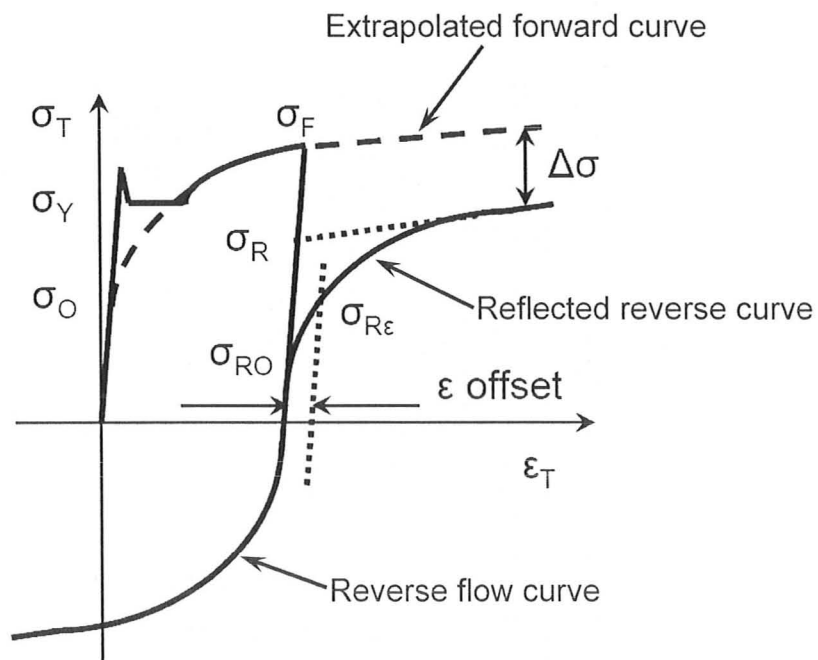


Figure 2.16 Schematic illustration of the Bauschinger test

Since back stresses impede forward flow, the forward flow stress (σ_F) can be expressed as a linear sum of three terms [Ibrahim (1974)]:

$$\sigma_F = \sigma_0 + \sigma_{for} + \sigma_B \quad (2.3)$$

where σ_0 is an initial yield stress, σ_{for} is the contribution of dislocation forest hardening (isotropic hardening), and σ_B is the back stress. It must be pointed out that σ_0 is different from the initial macroscopic yield stress (σ_Y), where σ_Y is generally affected by transient strengthening effects associated with initial dislocation locking and σ_0 excludes transient sources of flow resistance [Bate and Wilson (1986), Wilson (1965)]. Ibrahim (1974) determined σ_0 by extrapolating the part of the stress-strain curve corresponding to homogeneous deformation back to zero plastic strain, as shown in Figure 2.16. Assuming that the effect of changes in σ_{for} during forward and reverse flow can be neglected and that directional back stresses are not significantly relaxed during unloading, the reverse flow stress (σ_R) can be expressed using the equation:

$$\sigma_R = \sigma_0 + \sigma_{for} - \sigma_B. \quad (2.4)$$

Using equations (2.3) and (2.4), the value of back stresses can be derived [Ibrahim (1974)] as:

$$\sigma_B = \frac{\sigma_F - \sigma_R}{2}. \quad (2.5)$$

This is in agreement with Atkinson et al. (1974), who argued that the value of the back stress equals half of the permanent softening ($\Delta\sigma$), as shown in Figure 2.16.

The overall work hardening contains two contributions, σ_{for} from isotropic

hardening and σ_B from kinematic hardening. The fraction of the kinematic component within the overall work hardening, termed the Bauschinger Effect Ratio (B.E.R.), can be expressed as [Moan (1977)]:

$$B.E.R. = \frac{\sigma_B}{\sigma_{for} + \sigma_B} = \frac{\sigma_B}{\sigma_F - \sigma_0} . \quad (2.6)$$

Wilson (1965) first estimated back stresses in the matrix using X-ray diffraction and showed that the ratio between the magnitudes of back stresses and permanent softening was about 0.53. If using the methodology of Ibrahim (1974), the reverse flow stress (σ_R) is determined by extrapolating the part of the reflected reverse flow curve parallel to the extrapolated forward flow curve back to zero reverse plastic strain (Figure 2.16), the back stress is found to be exactly one half of the permanent softening, in excellent agreement with the measured value of Wilson (1965).

The disadvantage of using permanent softening to determine back stresses is that a large reverse flow is needed, which is not always practical to perform experimentally. Moan (1977) used an offset strain to obtain an offset reverse flow stress, σ_{Re} , and used equation (2.5) to calculate back stresses with σ_R replaced by σ_{Re} . Determination of σ_{Re} is illustrated in Figure 2.16. The advantage of this method is that only a very small reversal is required. Goel et al. (1983) also used this method to investigate the Bauschinger effect in a dual phase steel. As can be seen in Figure 2.16, the offset strain method over-

estimates the value of back stresses. However, Lloyd (1977) showed that the variation of back stresses with pre-strains was not affected. Note that σ_{R0} in Figure 2.16 is the reverse elastic limit, but it is very hard to determine because of the gradual elastic-plastic transition seen during reverse loading. As such, this quantity is not very useful.

Sinclair (2001) and Spencer (2004) used loading/unloading/reloading tests to measure back stresses. There was no compression used during their experiments. This method was used in the present research work, and it will be explained in detail in Chapter 4.

2.3.3 Back Stresses in Hard Phase Dispersed Steels

Uko (1978) investigated the Bauschinger effect of some spheroidized plain carbon steels and measured back stresses using the permanent softening method. These steels had a soft ferrite matrix with hard spherical Fe_3C particles. Other properties of the steels are shown in Table 2.2. The work of Uko (1978) showed that the development of back stresses in these steels agreed well with the model of Brown and Stobbs (1971b), i.e. back stress linearly increased with the square root of pre-strain (Figure 2.17 a)) and linearly increased with the volume fraction of hard particles (Figure 2.17 b)).

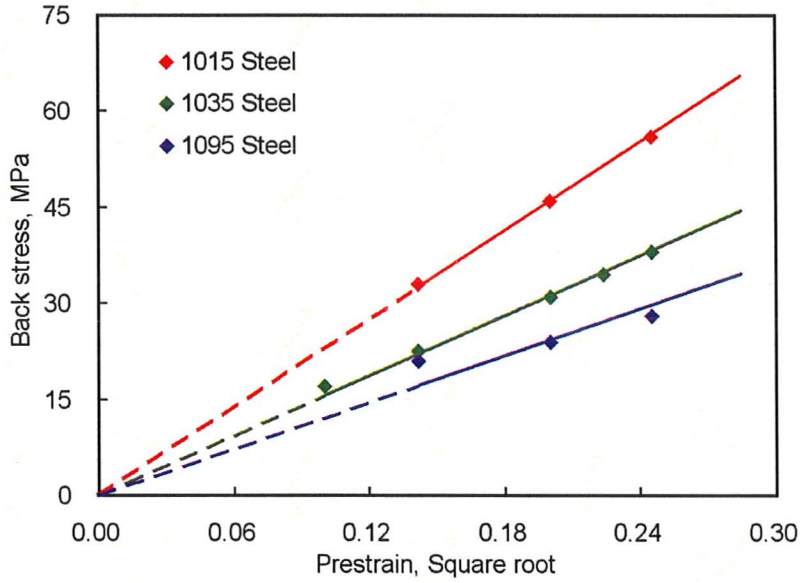
Goel et al. (1983) studied the Bauschinger effect of a dual phase steel. They measured back stresses using the offset strain method (0.002 offset). Their results

showed that back stresses increased initially with the volume fraction of martensite. A decrease in back stresses was observed when the volume fraction of martensite exceeded ~20%. They attributed this decrease to the relaxation effect resulting from the martensite islands being too closely spaced. Their data is shown in Figure 2.18.

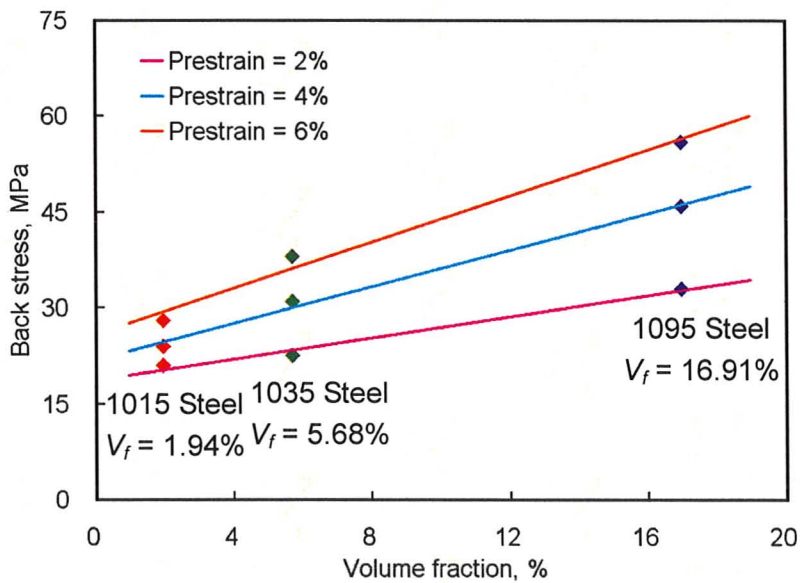
Table 2.2 Property parameters of the plain carbon steels used by Uko (1978)

Steel	wt.% Carbon	vol.% Fe ₃ C particles	Average particle diameter (μm)
1015	0.15	1.94	0.84
1035	0.35	5.68	0.89
1095	0.95	16.91	0.72

Gerbase et al. (1979) evaluated back stresses in dual phase steels using the permanent softening method, and their results are shown in Figure 2.19. The results differ from those of Uko (1978) and Goel et al. (1983) in that the back stress rose very rapidly at small pre-strains (up to 0.01), and then remained at a roughly constant value. Gerbase et al. (1979) argued that back stresses saturated quickly due to strong relaxation mechanisms associated with the yielding or fracture of the non-ferritic phases. Thus, high strength of the hard phase is essential to maintain unrelaxed strain and develop back stresses.



a) back stresses as a function of the square root of pre-strains



b) back stresses as a function of the volume fraction of Fe_3C particles

Figure 2.17 Back stresses in spheroidized carbon steels, re-plotted using the data of Uko (1978)

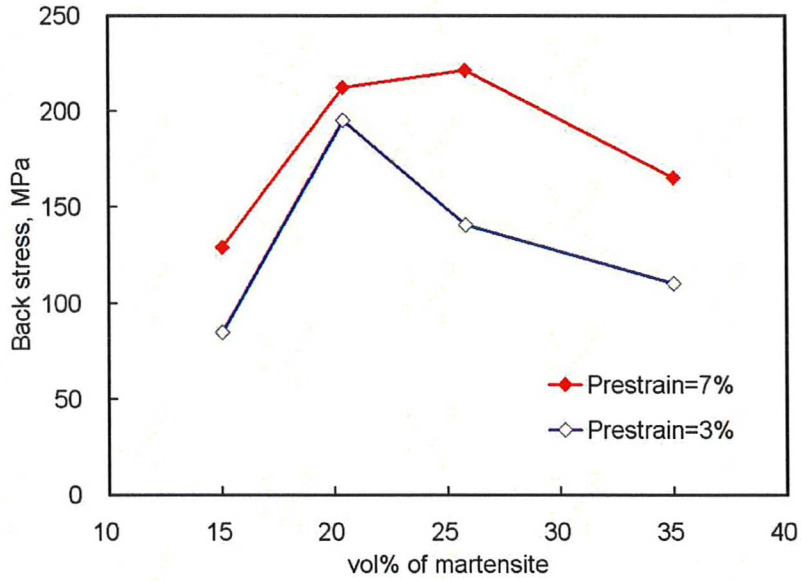


Figure 2.18 Back stresses in a dual phase steel, plotted using the data of Goel et al. (1983)

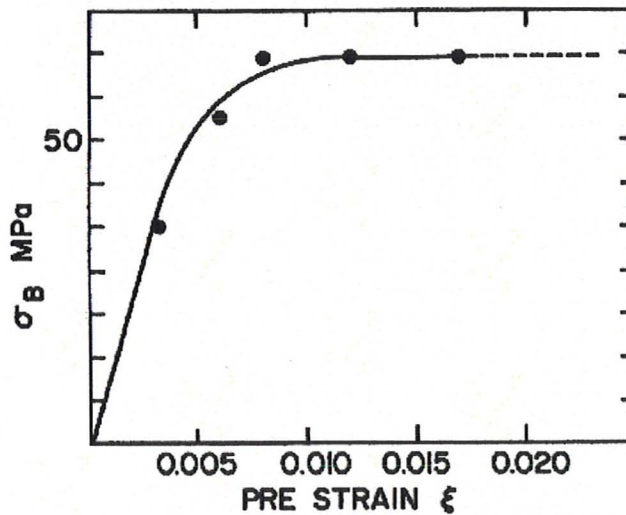


Figure 2.19 Back stresses in a dual phase steel as a function of pre-strains showing the saturation takes place at about $\epsilon=0.01$ [Gerbase et al. (1979)]

In TRIP-assisted steels, neutron diffraction [Jacques et al. (2006)] showed that retained austenite yields shortly after the Luder's plateau, but martensite is much stronger and can remain elastic up to the onset of necking. This means incompatible deformation must occur during plastic deformation of TRIP-assisted steels. The resulting back stresses will influence the flow stress and work hardening rate of TRIP-assisted steels. Furthermore, the influence of kinematic hardening on the overall work hardening of TRIP-assisted steels is expected to be more complicated than in spheroidized carbon steels and dual phase steels, where the volume fraction of hard phases remains constant during plastic deformation. TRIP-assisted steels comprise an evolving microstructure, in which the amounts of retained austenite and martensite change with applied strain. For this reason, back stresses in TRIP-assisted steels need to be studied in detail and this is one of the objectives of this thesis, as described in Chapter 3.

2.4 Models Characterizing the Evolution of $d\sigma/d\varepsilon$

It was stated in §2.2 that a material must have a sustained work hardening rate ($d\sigma/d\varepsilon$) to achieve the highly desirable combination of high strength and excellent ductility. Plots of $d\sigma/d\varepsilon$ vs. ε or $d\sigma/d\varepsilon$ vs. σ have been widely used to illustrate the evolution of $d\sigma/d\varepsilon$. However, these plots do not fully characterize the dynamic

progression of $d\sigma/d\varepsilon$. The modified Swift equation, equation (2.7), has been frequently used to analyze the plastic flow of dual phase steels consisting of ferrite, martensite, and possibly retained austenite, which can also transform to martensite upon deformation [Reed-Hill et al. (1973), Cribb and Rigsbee (1979), Jha et al. (1987)].

$$\varepsilon = \varepsilon_0 + C\sigma^m \quad (2.7)$$

where ε is the true strain, σ is the true stress, ε_0 is the initial true strain at yielding, and C and m are material constants. The logarithmic form of equation (2.7), differentiated with respect to ε , is given by

$$\text{Ln}\left(\frac{d\sigma}{d\varepsilon}\right) = (1-m)\text{Ln}\sigma - \text{Ln}Cm. \quad (2.8)$$

For a system which obeys equation (2.7), it can be seen that a plot of $\text{Ln}(d\sigma/d\varepsilon)$ versus $\text{Ln}\sigma$ will have a slope of $(1-m)$, which is indicative of the decreasing rate of $d\sigma/d\varepsilon$. As pointed out by Cribb and Rigsbee (1979), the value of m can be used as a measure of a material's capability to resist processes such as dynamic recovery, which tend to decrease $d\sigma/d\varepsilon$.

It was shown that two or three stages of tensile deformation of dual phase steels could be distinguished using a $\text{Ln}(d\sigma/d\varepsilon)$ vs. $\text{Ln}\sigma$ plot [Reed-Hill et al. (1973), Cribb and Rigsbee (1979), Jha et al. (1987)]. Figure 2.20 shows the $\text{Ln}(d\sigma/d\varepsilon)$ vs. $\text{Ln}\sigma$ plot of a mill-produced dual phase steel [Cribb and Rigsbee (1979)]. This steel

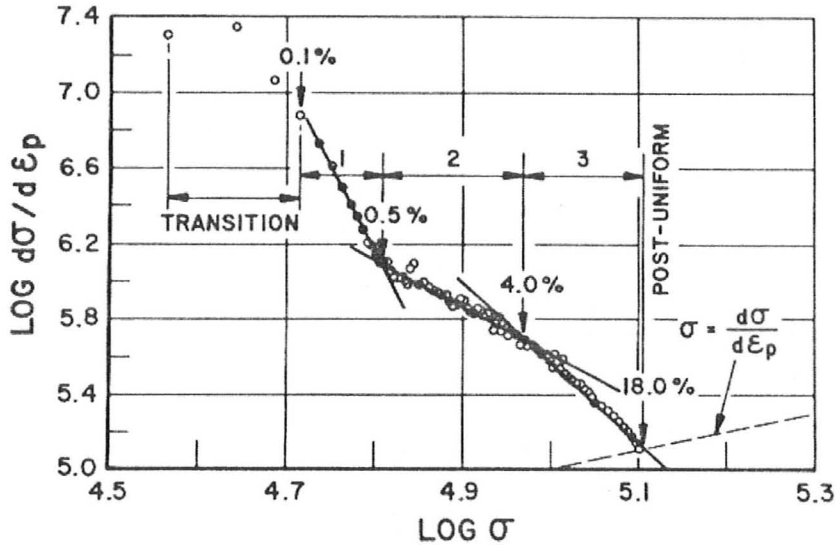


Figure 2.20 $\ln(d\sigma/d\varepsilon)$ vs. $\ln\sigma$ plot of a commercial dual phase steel exhibiting three work hardening stages [Cribb and Rigsbee (1979)]

exhibited a 380 MPa yield stress, a UTS of 690 MPa and a total elongation of approximately 0.27. Three stages of deformation in addition to the initial stage marked with “transition” can be observed in Figure 2.20. The transition stage is associated with multiple slip starting in the largest grains and spreading into neighbouring grains. Stage 1 arises from general yielding of the ferrite matrix. In Stage 2, the decrease in work hardening rates ($d\sigma/d\varepsilon$) is attenuated due to two mechanisms operating in the material. The first is incompatible deformation between the deforming ferrite and the rigid martensite and/or retained austenite particles. The incompatible deformation produces back stresses, which increase the flow stress and contribute to work hardening through

kinematic hardening. The second is the transformation of retained austenite to martensite, which is essentially the TRIP effect occurring in TRIP-assisted steels. This transformation leads to hardening mechanisms such as additional dislocation strengthening and composite strengthening mentioned in §2.2. As a result, decreases of the work hardening rate are further attenuated. The work hardening rate decreases more rapidly in stage 3. Several mechanisms could be operative in this stage. Further deformation gives rise to dislocation cross-slips and dynamic recovery, resulting in dislocation annihilation. Decohesion between the ferrite and martensite could also occur as a result of void nucleation and higher internal stresses. During this stage, the work hardening rate decreases until the onset of necking where work hardening is not sufficient to support the increase in flow stress.

As a comparable case, TRIP-assisted steels typically contain ferrite, retained austenite, and a minority of martensite in addition to bainitic ferrite. Ferrite is the principal source of plastic deformation; martensite and transforming retained austenite are second phases dynamically altering the work hardening rate of the material. Stage 2 (Figure 2.20) is an important process for TRIP-assisted steels in order to maintain high work hardening rates and achieve the desired balance between strength and ductility since considerable retained austenite to martensite transformation takes place in this stage [e.g. De Cooman (2004)].

CHAPTER 3: RESEARCH OBJECTIVE

Since cold rolling is widely used in the production of thinner-gauge steel strip for light-weight vehicle design, this research will focus on two cold-rolled TRIP-assisted steels heat treated through routes compatible with the continuous galvanizing process. In other words, the isothermal bainitic transformation temperature is fixed at 465 °C, which is a widely used strip entry temperature to the molten zinc bath. To make the steels galvanizable, Si was partially or completely replaced with Al. Bellhouse et al. have successfully galvanized the steels investigated in the present work and have determined several thermal cycles which produced the desired combination of strength and ductility for the alloys.

The aim of the present work is to measure the mechanical properties of two galvanizable Al containing TRIP-assisted steels and relate them to the processing parameters (i.e. intercritical annealing temperature and duration of isothermal bainitic transformation) and phase transformation during plastic deformation. More specifically, this work will:

- 1) Quantitatively characterize the phase constituents of the steels resulting from

the experimental heat treat parameters.

2) Follow the microstructural evolution as a function of applied strain and, in particular, the transformation of retained austenite to martensite.

3) Investigate the work hardening behaviour of these steels in terms of the incremental strain hardening coefficient and instantaneous work hardening rate with the contribution of kinematic hardening taken into account.

4) Link the microstructural evolution during plastic deformation to the work hardening behaviour of the steels.

5) Identify damage mechanisms and fracture modes of the steels.

CHAPTER 4: EXPERIMENTAL METHODS

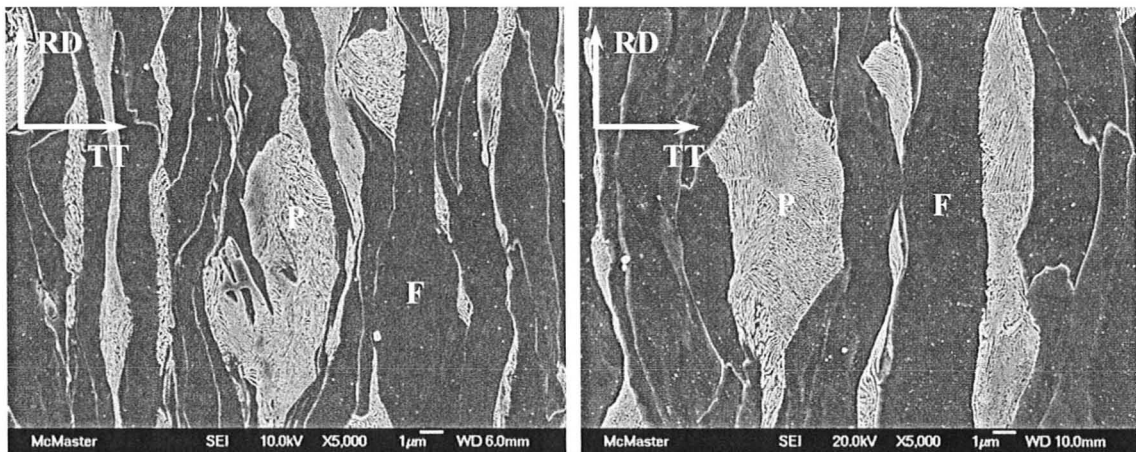
4.1 Steels Investigated

The as-received steels used in this research were fabricated at the CANMET Materials Technology Laboratory through hot-rolling, sandblasting and final cold rolling to approximately 1.6 mm thickness. The hot rolling start and finish temperatures were 1250 °C and 850 °C, respectively. These as-received steels were designated 1.5Al and 1.0Al, respectively, referring to their Al contents. The chemical composition of the experimental alloys, as determined by the supplier, is summarized in Table 4.1. As can be seen from Table 4.1, the C and Mn contents of the experimental alloys were relatively constant at 0.20 wt.% and 1.5 wt.%, respectively, and the total Al + Si content was approximately 1.5 wt.%. Although conventional TRIP-assisted steels typically contain 1.0 ~ 1.5 wt.% Si [Matsumura et al. (1987)], Al was either partially or completely substituted for Si in the present alloys with the specific objectives of improving their galvanizability, and both of the alloys investigated had previously been successfully galvanized by Bellhouse and coworkers [Bellhouse et al. (2007), Bellhouse and

McDermid (2008)]. The microstructure of as-received steels consists of ferrite and pearlite, which is presented in Figure 4.1.

Table 4.1 Chemical compositions of as-received steels (wt.%)

Designation	C	Mn	Si	Al	Ti	S	P	O	N
1.0Al	0.20	1.52	0.45	1.0	0.021	0.0025	0.005	0.0020	0.0027
1.5Al	0.20	1.50	<0.010	1.45	0.022	0.003	0.005	0.0036	0.0026



a) 1.0Al steel

b) 1.5Al steel

Figure 4.1 Microstructure of as-received steels
(RD: rolling direction, TT: through thickness, P: pearlite, F: ferrite)

4.2 Heat Treatments

4.2.1 Heat Treatment Facility

All experimental heat treatments were carried out using the McMaster Galvanizing Simulator (MGS), pictured in Figure 4.2. The MGS is able to fully simulate the industrial continuous galvanizing line (CGL). It comprises an atmosphere-controlled column consisting of four sections (from top to bottom of the column): i) sample loading/cooling, ii) sample heating, iii) gas jet wiping and iv) zinc pot. The latter two sections were not used in this work. The loading/cooling section contains two parallel gas cooling plattens and controlled cooling is accomplished by a high velocity N_2/H_2 gas stream. The quartz lamp infrared (IR) furnace was used for all heat treatments. The heat treatment atmosphere was controlled through a series of mass flow controllers. The partial pressure of oxygen in the system was controlled through H_2O (g) additions to the process gas. The experimental atmosphere used throughout this work was 95 N_2 /5 H_2 (vol.%) with a -30 °C dew point. The thermal cycles were controlled using a type K (0.5 mm) thermocouple welded directly to the steel panel prior to loading, per Figure 4.3.

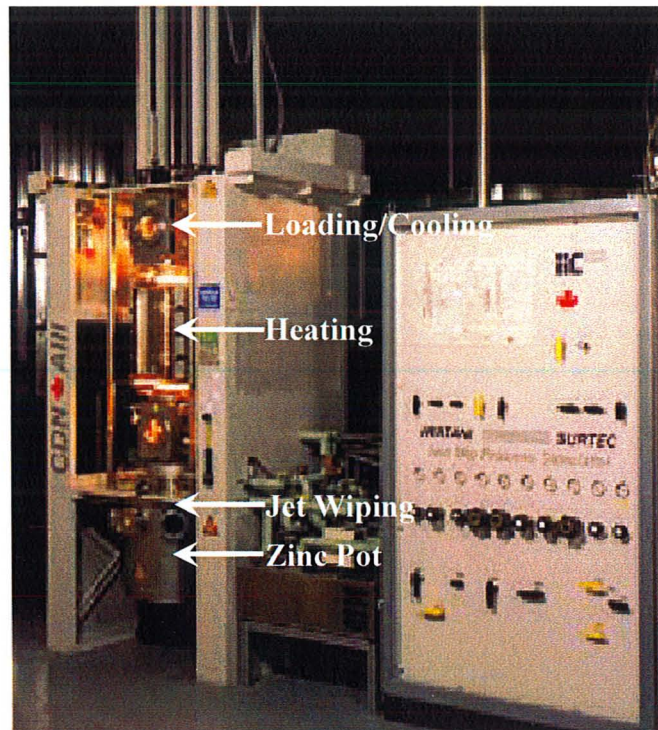


Figure 4.2 McMaster Galvanizing Simulator

The steel panels used for all experiments were 200 mm × 120 mm with the longitudinal axis parallel the rolling direction. It should be noted that the central 180 mm × 100 mm uniform temperature portion of the steel panel was used for subsequent microstructural or mechanical property evaluations, Figure 4.3. Prior to annealing, the steel panels were cleaned using a hot 2wt.% NaOH solution (80 ~ 90°C), rinsed with water, cleaned ultrasonically in iso-propanol and dried with warm air. In Figure 4.3, the direction of tensile samples used for tensile testing (§4.4) is also indicated.

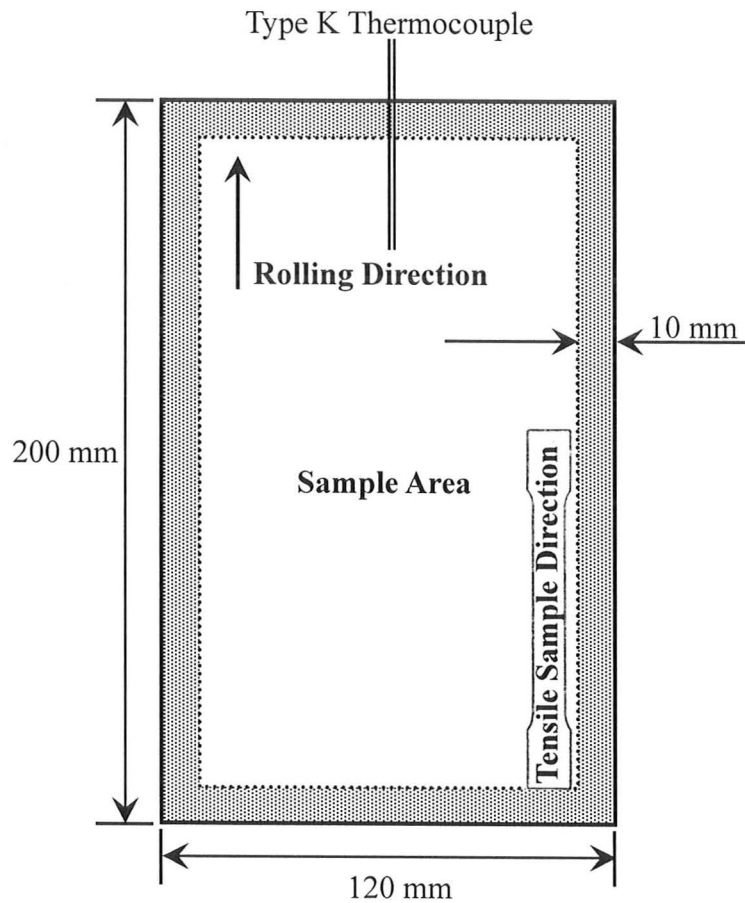


Figure 4.3 Geometry of the steel panel and the sample area for analysis

4.2.2 Heat Treatment Parameters

The optimum heat treatment parameters for the two alloys shown in Table 4.1 have been determined in the previous work of Bellhouse and McDermid (2007). All experimental heat treatments in the present work were based on these parameters, presented in Table 4.2.

Table 4.2 *The designation of heat treated steels and their parameters*

Designation	IA (°C)	IBT (s)	Designation	IA (°C)	IBT (s)
1.0Al_35% γ 60s	770	60	1.5Al_35% γ 60s	795	60
1.0Al_35% γ 120s	770	120	1.5Al_35% γ 120s	795	120
1.0Al_50% γ 60s	825	60	1.5Al_50% γ 60s	862	60
1.0Al_50% γ 120s	825	120	1.5Al_50% γ 120s	862	120

Two intercritical annealing (IA) temperatures were used: one lower temperature producing an intercritical annealing microstructure of 65% α + 35% γ and a higher temperature producing an intercritical annealing microstructure of 50% α + 50% γ . Using ThermoCalc® and the TCFE2 database [Bellhouse and McDermid (2007)], these two intercritical annealing temperatures were determined to be 770 °C and 825 °C, respectively, for the 1.0Al steel, and were determined to be 795 °C and 862 °C, respectively, for the 1.5Al steel. The intercritical annealing hold time was 120s in all cases. The isothermal bainitic transformation (IBT) temperature was 465°C in all cases. Two bainitic transformation hold times, 60s and 120s, were used. In all heat treatment cycles, the heating rate and the cooling rate were 10 °C/s and 20 °C/s, respectively. The intercritical austenite fraction and the bainitic transformation hold time of each heat treatment cycle, together with the Al content in the steel, were used to designate the

sample identity, per Table 4.2, where the experimental heat treatment matrix is summarized.

4.3 Sample Characterization

4.3.1 Scanning Electron Microscopy (SEM)

Microstructural characterization was performed using a JEOL 7000F SEM. As TRIP-assisted steels can contain ferrite, bainitic ferrite, retained austenite, and martensite in varying proportions, it is very important to distinguish all of these phases easily in order to properly assess the effect of experimental variables on the resultant microstructures. In particular, distinguishing martensite from retained austenite is essential to characterize TRIP-assisted steels as the two phases cannot be directly distinguished using SEM.

In the present research work, a tempering technique described by Girault et al. (1998) was used to distinguish retained austenite from martensite. All SEM samples were tempered at 250°C for 2 hours, during which the samples were buried within carbon powder to avoid oxidation and decarburization. As a result of this treatment, epsilon carbides precipitated within martensite. These carbides, which are sensitive to etching, make martensite distinguishable from retained austenite in the SEM.

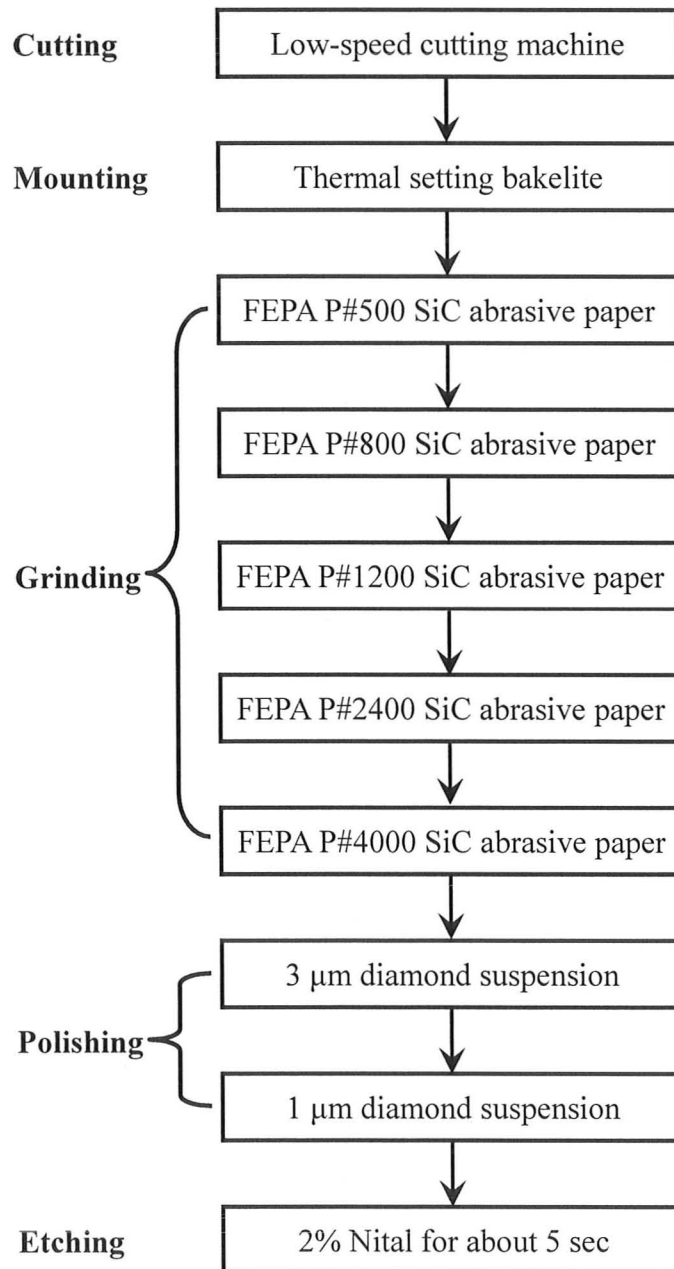
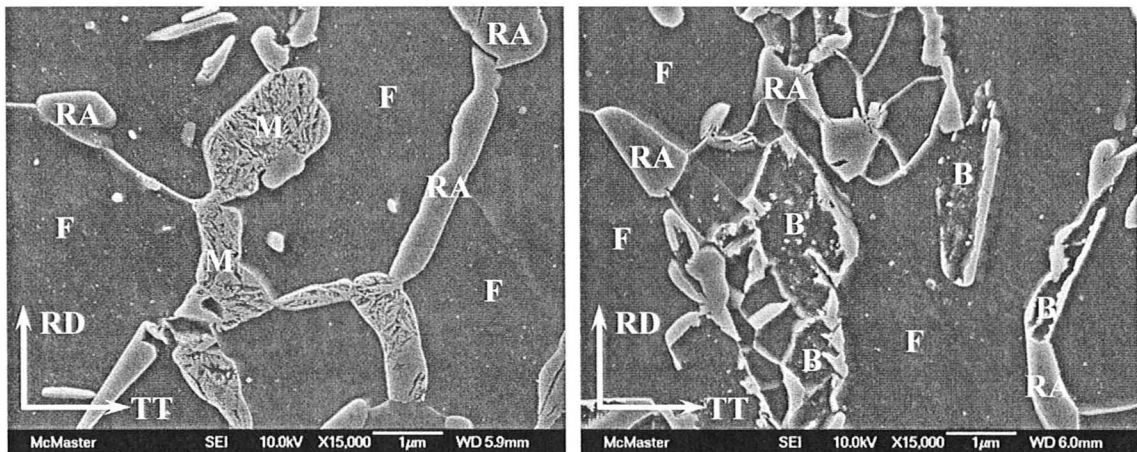


Figure 4.4 SEM sample preparation procedures

After tempering, samples were cut along the rolling direction and thickness direction using a low-speed cutting machine. The subsequent mounting, grinding, polishing and etching procedures used are shown in Figure 4.4. A 2% nitric acid in ethanol was used for etching throughout this work and the etching time was approximately 5 seconds.



a) Distinguishing martensite and retained austenite ($1.0Al_{35}\gamma_{60s}$) b) Distinguishing ferrite and bainitic ferrite ($1.0Al_{35}\gamma_{120s}$)

Figure 4.5 SEM micrographs showing distinguishable phases in TRIP-assisted steels after tempering at 250°C for 2 hours (M: martensite, RA: retained austenite, F: ferrite, B: bainitic ferrite, RA: rolling direction, TT: through thickness)

Micrographs were generally taken at the mid-thickness of the section with SEM settings of 10 keV accelerating voltage and 6 mm working distance. Figure 4.5 presents two micrographs to show how to distinguish the various phases in tempered samples.

Figure 4.5 a) gives the microstructure of a tempered 1.0Al_35% γ 60s steel, where retained austenite and martensite are easily distinguished. Bainitic ferrite was distinguished from polygonal ferrite based on its morphology, shown in Figure 4.5 b). From the two SEM micrographs, it can also be seen that the tempering heat treatment distinguished martensite while retained austenite was not affected.

4.3.2 X-ray Diffraction (XRD)

The volume fraction and lattice parameter of any retained austenite were determined using XRD (X-ray Diffraction). Diffraction frames were obtained using a SMART APEX II system with a Mo K α source ($\lambda=0.70930 \text{ \AA}$) and analyzed using GADDS (General Area Detector Diffraction System); the fraction and lattice parameter values were calculated using TOPAS. The analysis region was at the mid-thickness of the cross section in the traverse and thickness directions. All analysis surfaces were polished using a 1.0 μm diamond suspension. The $\{111\}$, $\{200\}$, $\{220\}$ and $\{311\}$ peaks of austenite and $\{110\}$, $\{200\}$ and $\{211\}$ peaks of ferrite were used for the analysis.

As already mentioned, significant amounts of martensite could exist in some samples, especially in strained samples. Martensite has a BCT structure, a distorted BCC structure. Due to this distortion, BCC peaks split. For example, $\{110\}\alpha$ splits into $\{101\}\alpha'$ and $\{110\}\alpha'$. $\{101\}\alpha'$ contributes to the intensity of $\{111\}\gamma$. For this reason,

martensite peaks were considered in the analysis [Bellhouse et al. (2007)]. From the determined lattice parameter, the carbon content of retained austenite was calculated using equation (4.1), which combines the equation of Ruhl and Cohen (1969) for C, Si and Mn and the equation of Dyson and Homes (1970) for Al.

$$a \left(\overset{\circ}{A} \right) = 3.572 + 0.0012(\text{wt.\%Mn}) - 0.00157(\text{wt.\%Si}) + 0.0056(\text{wt.\%Al}) + 0.033(\text{wt.\%C}) \quad (4.1)$$

4.3.3 Quantitative Image Analysis

Although X-ray diffraction has been widely used to determine the volume fraction of retained austenite, several errors can occur using XRD, which will be discussed in detail in Chapter 5. In the present work, quantitative image analysis was performed to confirm the XRD results for retained austenite and to quantify the volume fractions of martensite and bainitic ferrite, which are unable to be analyzed using X-ray diffraction. Another advantage of the quantitative image analysis was that retained austenite in different morphologies can be analyzed separately.

Quantitative image analysis was performed based on SEM micrographs in which each phase was able to be unambiguously identified as described in §4.3.1. Figure 4.6 shows that two morphologies of retained austenite can be readily identified. Lamellar retained austenite, represented by RA_L in Figure 4.6, was strongly associated with

bainitic ferrite and usually presented an elongated or acicular morphology. The other kind of retained austenite, represented by RA_B in Figure 4.6, was defined as blocky retained austenite and had a polygonal or equiaxed morphology. According to the literature, lamellar retained austenite has both a higher chemical stability due to its higher carbon content and a higher mechanical stability due to the effect of the surrounding bainitic ferrite [Jacques et al. (2001c), Timokhina et al. (2004)].

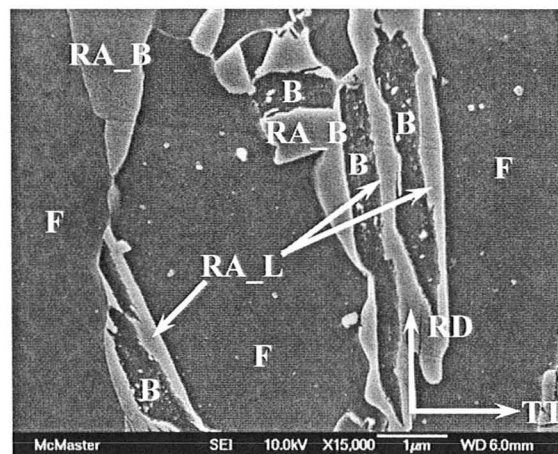


Figure 4.6 SEM micrograph showing retained austenite distinguishable in two morphologies, 1.0Al_35%γ60s
(RA_L: lamellar retained austenite, RA_B: blocky retained austenite, F: ferrite, B: bainitic ferrite, RD: rolling direction, TT: through thickness)

To have a statistical meaning, the SEM images analyzed were taken from 6 random fields per sample and the results averaged. Each image was $24\ \mu\text{m} \times 18\ \mu\text{m}$. The image analysis procedure comprised outlining the martensite, lamellar retained austenite, blocky retained austenite and bainitic ferrite phases on a transparent sheet overlaid on a

printed SEM micrograph using various colours, and analyzing the scanned drawing using a Northern Eclipse® image analysis software program. Each phase, represented by a specific colour, can be analyzed individually.

Figure 4.7 through Figure 4.9 show how the image analysis procedure was performed. Figure 4.7 shows two SEM micrographs of the 1.0Al_35% γ 60s steel: a) as annealed and b) strained by $\epsilon=0.05$. Blocky retained austenite, lamellar retained austenite, bainitic ferrite and martensite in the two micrographs are separated and shown individually in Figure 4.8 and Figure 4.9, respectively, where the corresponding area fraction for each phase measured using the software program is also indicated. The fraction of ferrite for each microstructure was determined by difference.

The size of blocky and lamellar retained austenite was also analyzed using image analysis. The average equivalent circular diameter was used to evaluate blocky retained austenite. Equivalent circular diameter is the diameter of a circle that would have the equivalent area as the analyzed object, schematically shown in Figure 4.10. The average thread length and thread width were used to evaluate lamellar retained austenite because most of the lamellar retained austenite was threadlike or bent, per the objects shown in Figure 4.11, which were taken from the bottom-left corner of Figure 4.9 b). Thread length, the length AB in Figure 4.11, and thread width, the length CD in Figure 4.11, give an estimate as to the true length and width of a thread-like object, respectively [Northern

Eclipse®]. For this size analysis, the objects cut by the edges were not included since these objects were not complete.

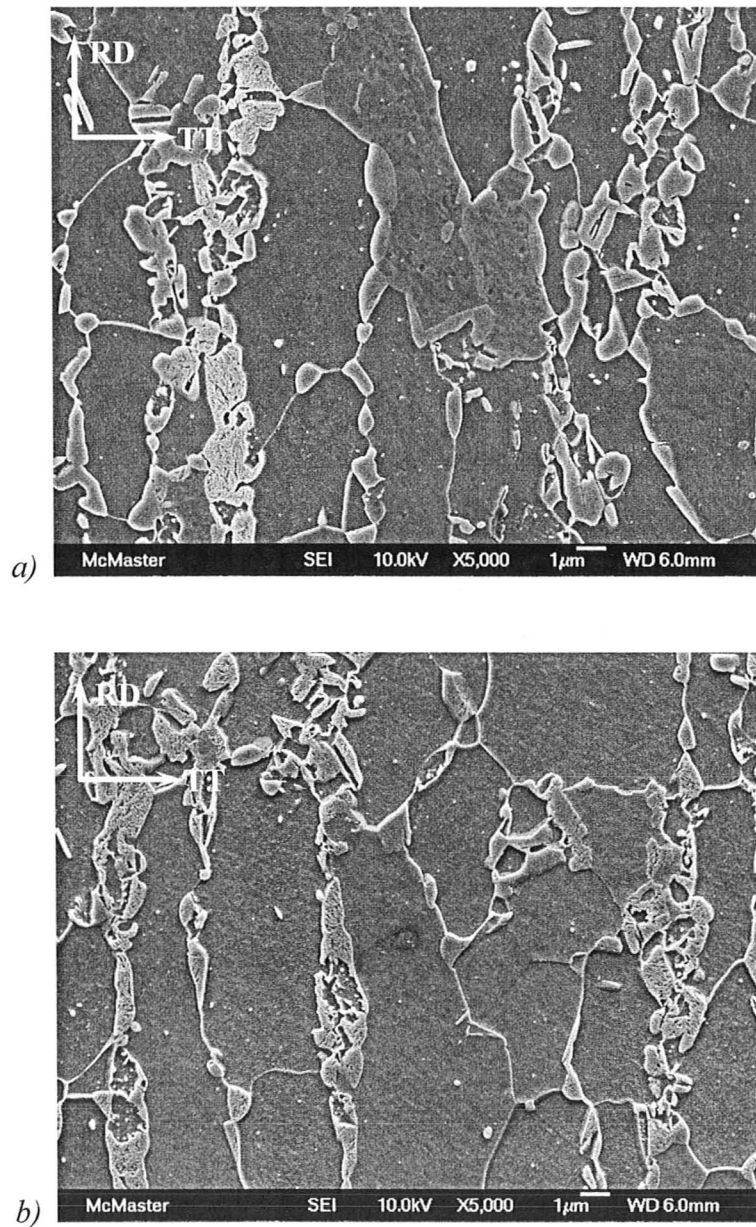
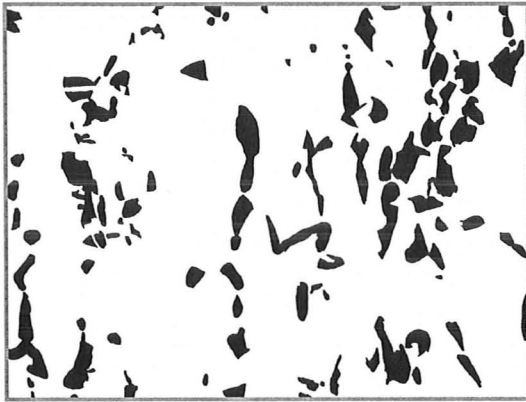
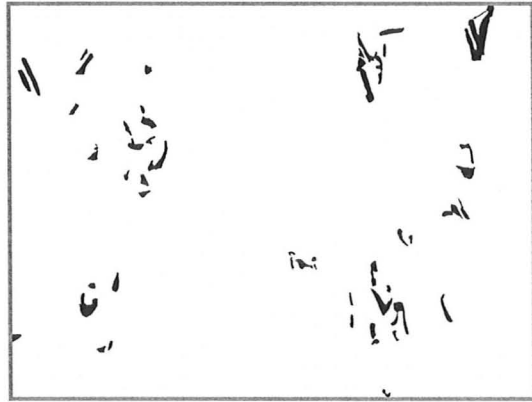


Figure 4.7 SEM micrographs of the 1.0Al_{35%}γ60s steel for image analysis: a) As annealed, b) $\epsilon = 0.05$, (RD: rolling direction, TT: through thickness)



a) Blocky retained austenite, 15%



b) Lamellar retained austenite, 2%

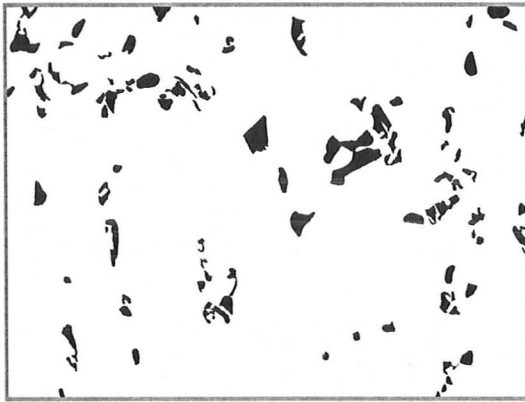


c) Bainitic ferrite, 5%

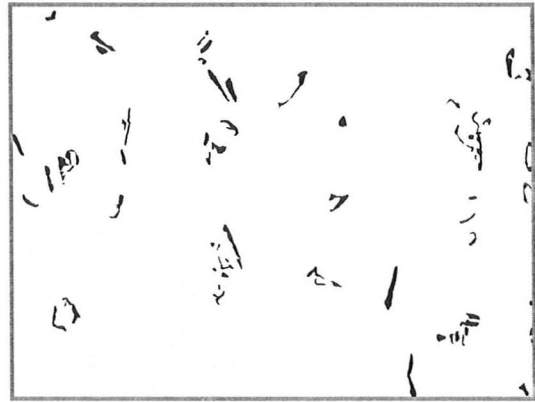


d) Martensite, 4%

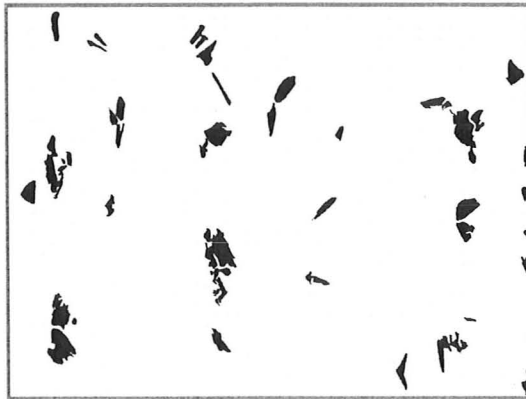
Figure 4.8 Separated phases of the microstructure shown in Figure 4.7 a)



a) Blocky retained austenite, 6%



b) Lamellar retained austenite, 2%



c) Bainitic ferrite, 4%



d) Martensite, 8%

Figure 4.9 Separated phases of the microstructure shown in Figure 4.7 b)

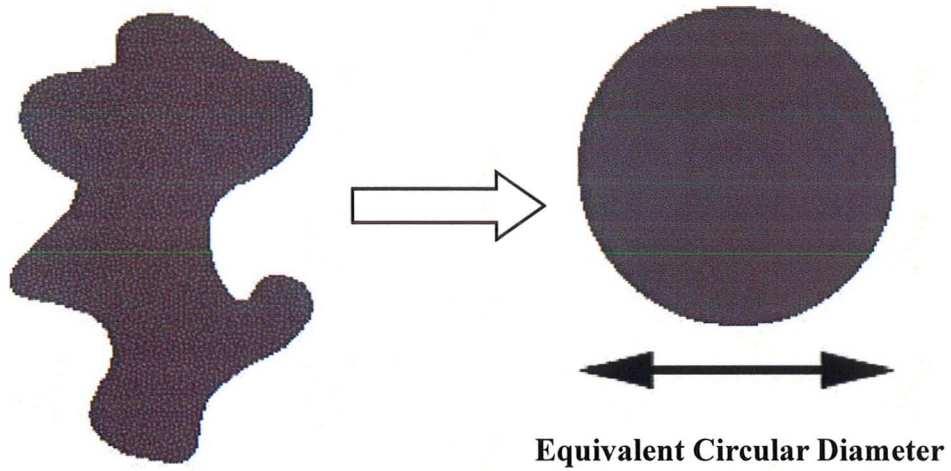


Figure 4.10 Schematic definition of equivalent circular diameter

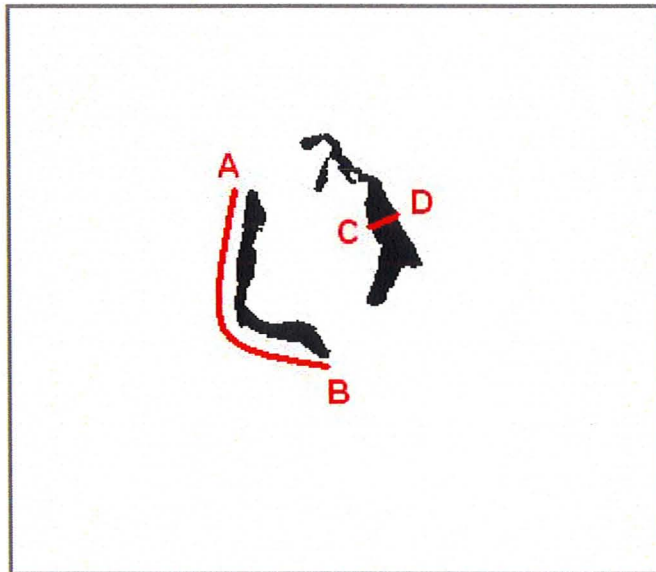


Figure 4.11 Schematic definition of thread length (AB) and thread width (CD)

4.4 Tensile Testing

All tensile testing was performed using a 10 kN Instron 5566 machine. The samples used throughout were ASTM E 8M-04 sub-size samples, per Figure 4.12. The sample gauge length was 25 mm and the width 6 mm. The samples were machined along the rolling direction of the steel panels, Figure 4.3, by means of EDM (Electrical Discharge Machining) to avoid any effect of surface deformation on retained austenite transformation. The engineering strain was measured using an extensometer attached to the gauge length of the tensile sample. The measured engineering stress - engineering strain curves prior to necking were converted to true stress - true strain curves for further analysis. In this case, the point of uniform elongation or the start of necking was determined using the Considère criterion, described as follows.

The condition of instability leading to local necking is

$$dP = \sigma dA + A d\sigma = 0. \quad (4.2)$$

P : load; A : instantaneous cross-section; σ : true stress

As well known, the constant volume of the gauge section can be assumed during plastic deformation. With this assumption and equation (4.2), the following equation at the point of tensile instability can be derived.

$$\frac{d\sigma}{d\varepsilon} = \sigma \quad (4.3)$$

ε : true strain

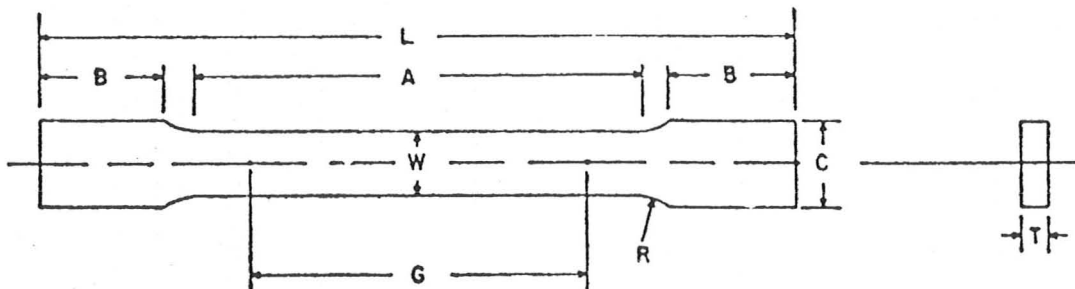
The incremental work hardening coefficient, n_{incr} , is defined as

$$n_{incr} = \frac{d(Ln\sigma)}{d(Ln\varepsilon)} = \frac{\varepsilon}{\sigma} \frac{d\sigma}{d\varepsilon} \quad (4.4)$$

Substituting the necking criterion given in equation (4.3) into equation (4.4) gives

$$\varepsilon_u = n_{incr} \quad (4.5)$$

ε_u : uniform elongation (the true strain at which necking occurs.)



G (Gage length): 25.0 ± 0.1 mm

W (Width): 6.0 ± 0.1 mm

R (Radius of fillet): 6 mm

L (Overall length): 100 mm

A (Length of reduced section): 32 mm

B (Length of grip section): 30 mm

C (Width of grip section): 10 mm

T (thickness): the thickness of as-received steel sheets

Figure 4.12 Geometry of the tensile sample [ASTM International]

4.4.1 Monotonic Tensile Tests

For monotonic tensile testing, the samples were tested to fracture. The crosshead speed was set at 1 mm/min. Based on the true stress - true strain curves, the incremental work hardening coefficient was calculated using equation (4.4).

4.4.2 Unloading/Reloading Tests

It has been mentioned that kinematic hardening is due to the development of back stresses in plastically deformed materials. Unloading/reloading tests were carried out to measure back stresses, and then determine their contribution to the kinematic hardening of the experimental TRIP-assisted steels. Figure 4.13 gives an example of the unloading/reloading test curve. The sample was loaded to a pre-set strain, unloaded to immediately above zero load, and then reloaded to the next pre-set strain. Loading/unloading cycles were typically conducted at pre-strains of 0.025, 0.050, 0.075, 0.100, 0.125, 0.150, 0.175 and 0.200, also shown in Figure 4.13.

Figure 4.14 shows a magnified view of the fourth loading/unloading/reloading cycle in Figure 4.13. The test undergoes the path of A→B→C→D→E→F. From this curve, it can be clearly seen that the unloading was not perfectly elastic and that the sample experienced significant reverse plastic flow. This is indicative of significant back

stresses being present in the material. Using this unloading/reloading loop, Figure 4.14 also illustrates how the forward flow stress (σ_F) and the reverse flow stress (σ_R) were defined in the present case. The true stress at B, where unloading starts, was defined as the forward flow stress. The solid line through B is the elastic unloading line, which is parallel to the linear elastic section of the true stress-true strain curve. This line was offset backward by 0.02% to where the dotted line is located. The dotted line intersects the unloading curve at C, which was designated as the elastic limit during the unloading cycle. The stress at this point was defined as the reverse flow stress. The back stress (σ_B) was then calculated using equation (4.5) [Sinclair (2001)].

$$\sigma_B = \frac{\sigma_F - \sigma_R}{2} \quad (4.5)$$

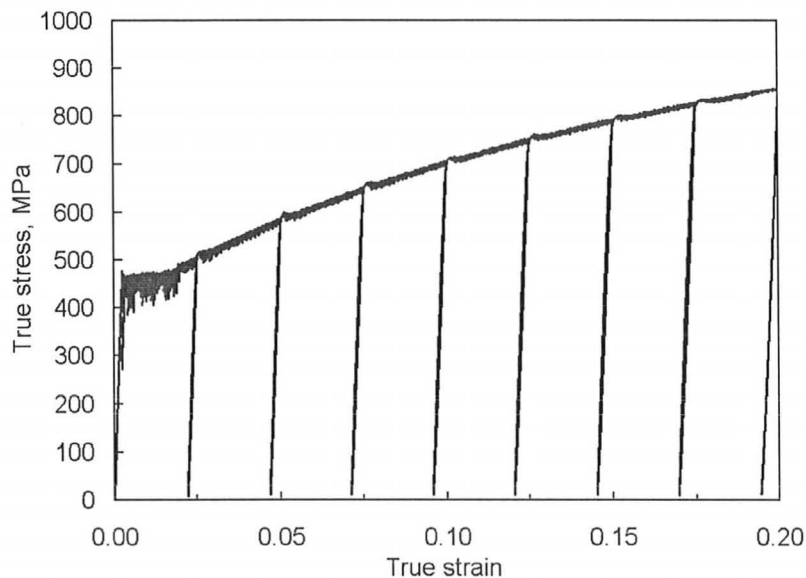


Figure 4.13 The unloading/reloading curve of the 1.5Al_{35%γ}120s steel

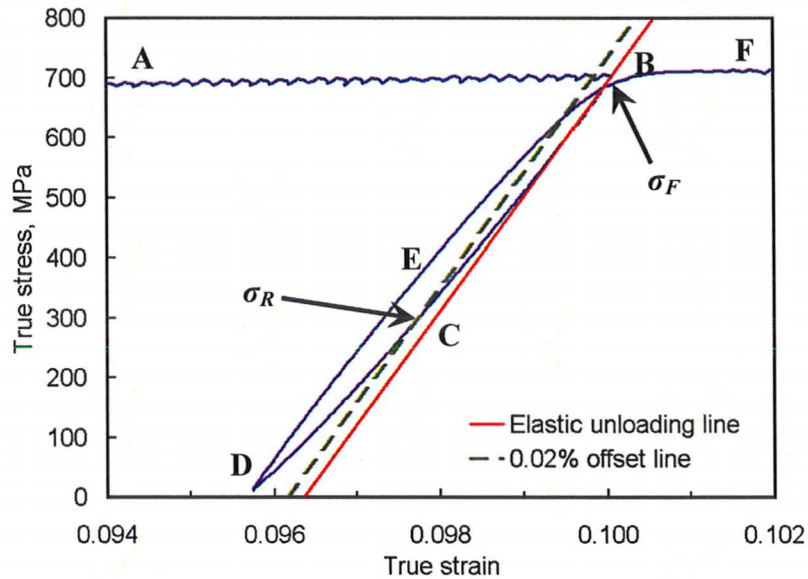


Figure 4.14 The loading/unloading/reloading cycle at the pre-set strain of 0.100 of the 1.5Al_{35%}γ120s steel (the fourth cycle in Figure 4.13)

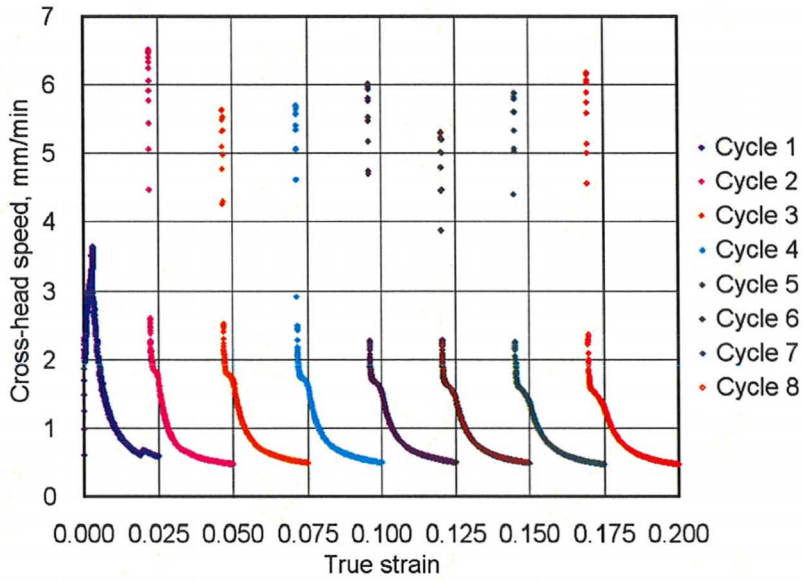
It is worthy of note that true back stresses were not being measured using the method shown in Figure 4.14 and equation (4.5). As mentioned in Chapter 2, the value of true back stresses was measured as one-half of the permanent softening in the Bauschinger effect test [Atkinson et al. (1974)]. To perform a complete Bauschinger effect test, the sample must be compressed sufficiently to obtain parallel forward and reverse flow curves, which is not possible when testing sheet materials as samples will buckle. Thus, there was no compression at all while performing the unloading/reloading tests in the present work. The obtained value of back stresses should be further over-

estimated. Spencer (2004) also used the unloading/reloading method to measure back stresses, and showed that applying various offset strains affected the magnitudes of back stresses only, but not the trends. A further consideration in the present work was that reverse plastic flow occurred in the forward quadrant and no reflection was applied. Thus, a minus sign should be applied to the reverse flow stress indicated in Figure 4.14. In other words, σ_R in equation (4.5) has a negative value.

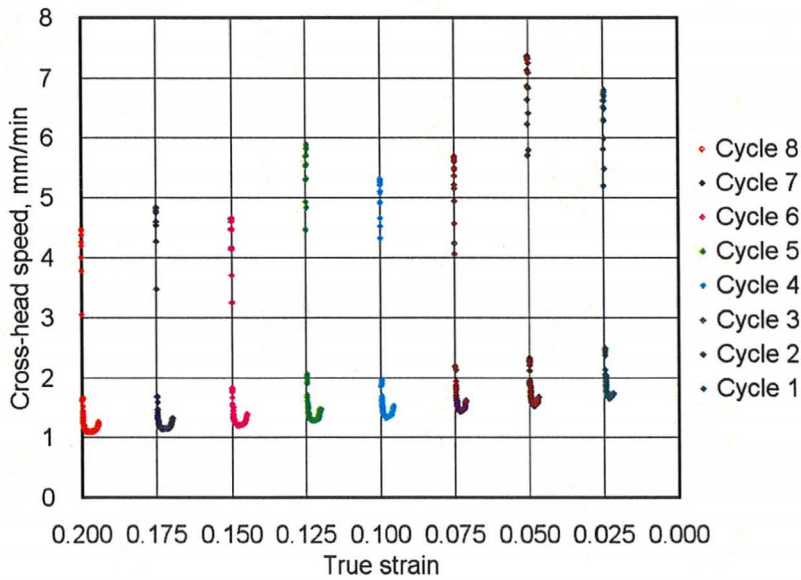
To conduct unloading/reloading tests, strain values at which unloading starts must be pre-set, Figure 4.13. The machine was set to strain-controlled mode, and the crosshead speed was unable to be fixed. In other words, the cross-head speed changed constantly during the test. As an example, Figure 4.15 shows how the crosshead speed evolves during the unloading/reloading test shown in Figure 4.13. Figure 4.15 a) shows the crosshead speed of the loading section for each cycle, and Figure 4.15 b) the cross-head speed of the unloading section. It can be seen that, for most of the test, the crosshead speed ranged from 0.5 to 2 mm/min.

4.4.3 Interrupted Tensile Tests

To investigate the microstructural evolution of each steel as a function of plastic strain, interrupted tensile tests were carried out. For each steel, five strain levels: 0.025, 0.050, 0.100, 0.150 and 0.200, were selected for the interruption. The fraction of retained



a) The cross-head speed of the loading section for each cycle



b) The cross-head speed of the unloading section for each cycle

Figure 4.15 The cross-head speed of the unloading/reloading test shown in Figure 4.13

austenite in the strained samples was measured using both the X-ray diffraction and image analysis techniques; the fraction of martensite was measured using the image analysis technique. Similar to the unloading/reloading test, an interruption strain must be pre-set for the interrupted test. The machine was also set to strain-controlled mode.

4.5 Examination of Fracture Mechanisms

To investigate fracture modes of the steels, the fracture surfaces of monotonic tensile samples were examined using SEM with the working distance set to 10-15 mm. The thickness section of 0.200 strained samples was also prepared for SEM observation to further investigate fracture mechanisms. These samples were tempered, cut, mounted, grinded, polished and etched according to the procedures described in §4.3.1.

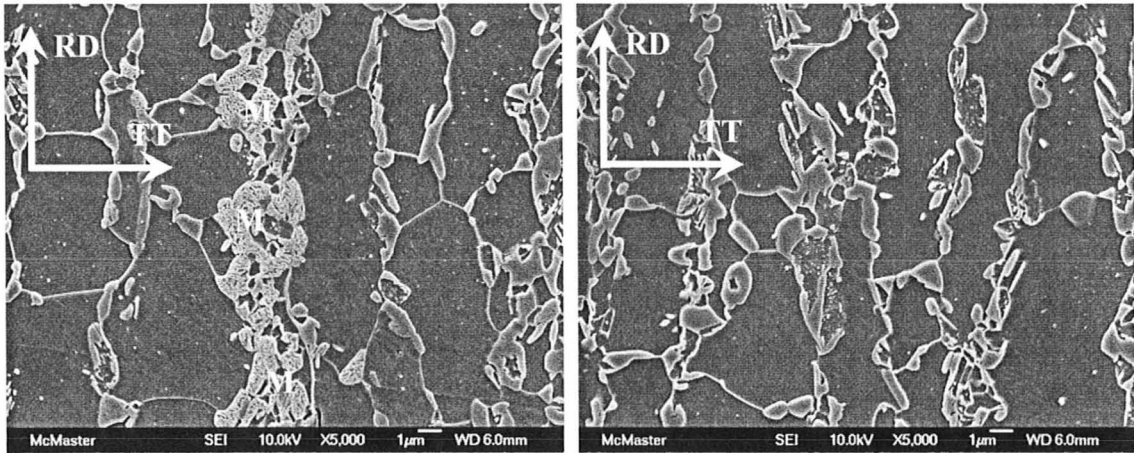
CHAPTER 5: EXPERIMENTAL RESULTS

5.1 As-annealed Steels

5.1.1 Microstructures

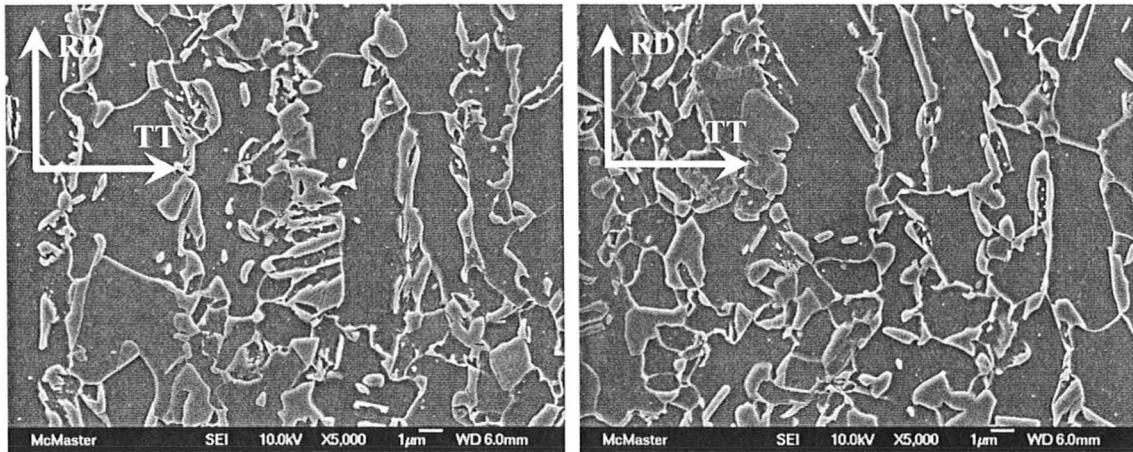
The microstructures of the steels produced through the thermal heat treatment cycles shown in Table 4.2 are presented in this section. In each SEM micrograph of Figure 5.1, ferrite, bainitic ferrite, retained austenite, and/or martensite can be distinguished according to the methods explained in §4.3.1. The microstructure of the 1.0Al_35% γ 60s steel (Figure 5.1 a)) exhibited the highest amount of martensite, which is marked with M on the micrograph.

Close examination of the eight SEM micrographs in Figure 5.1 indicates that the microstructures of the 1.0Al steels (Figure 5.1 a) - d)) exhibited a strongly banded structure, whereas the microstructures of the 1.5Al steels (Figure 5.1 e) - h)) were more homogeneous. Martensite appeared mainly in the banded region for the 1.0Al steels (Figure 5.1 a)). The banded structure is likely associated with Mn segregation during solidification of the as-received steels (Figure 4.1).



a) 1.0Al_35% γ 60s

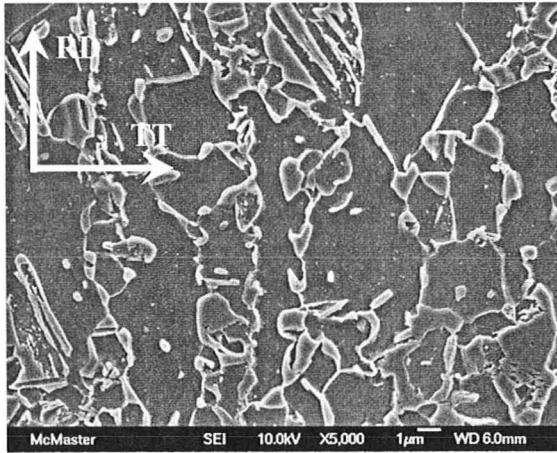
b) 1.0Al_35% γ 120s



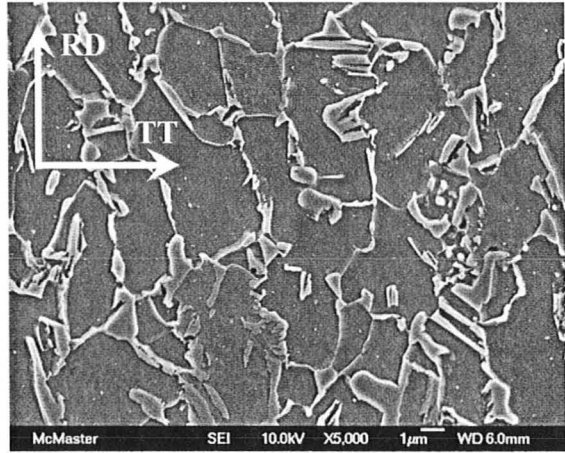
c) 1.0Al_50% γ 60s

d) 1.0Al_50% γ 120s

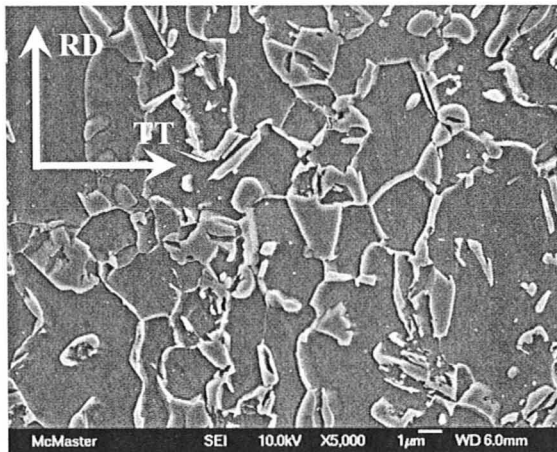
Figure 5.1 SEM micrographs of the as-annealed steels
(M: martensite, RD: rolling direction, TT: through thickness)



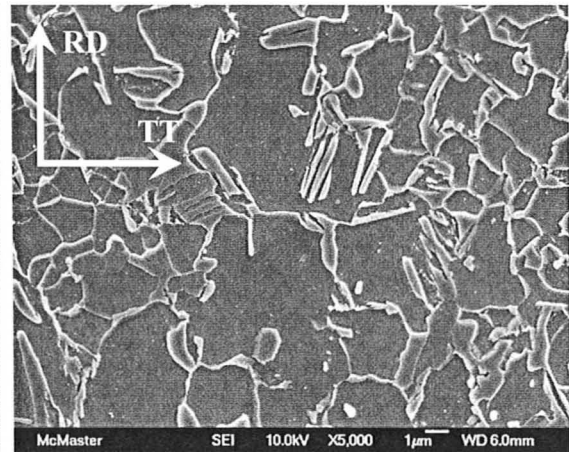
e) 1.5Al_35%γ60s



f) 1.5Al_35%γ120s



g) 1.5Al_50%γ60s



h) 1.5Al_50%γ120s

Figure 5.1 (cont'd) SEM micrographs of the as-annealed steels
(RD: rolling direction, TT: through thickness)

Table 4.2 showed that the steels were intercritically annealed at a temperature producing 65% ferrite + 35% austenite or 50% ferrite + 50% austenite. During cooling from the intercritical annealing to isothermal bainitic transformation temperatures and following hold at the IBT temperature (465°C), as well as subsequent quenching to room temperature, the intercritical austenite underwent phase transformations which produced either bainitic ferrite, retained austenite, or martensite. The cumulative fractions of these three phases based on image analysis of SEM micrographs for all steels are shown in Figure 5.2. It can be seen that the sum of retained austenite (blocky and lamellar), bainitic ferrite, and/or martensite volume fractions is significantly less than the equilibrium fraction of intercritical austenite at each intercritical annealing temperature. This difference between the equilibrium fraction of intercritical austenite and the cumulative fraction of transformed phases is assumed to be taken up by ferrite formation that took place during the thermal processes following intercritical annealing, per Figure 5.2.

Further examination of Figure 5.2 will show that about one-third to one-half of the intercritical austenite transformed to ferrite for the steels with 35vol.% equilibrium intercritical austenite and one-half or more of the intercritical austenite transformed to ferrite for the steels with 50vol.% equilibrium intercritical austenite. In other words, more intercritical austenite transformed to ferrite when a higher intercritical annealing temperature was used. The longer bainitic transformation hold time resulted in more

ferrite formation and less retained austenite in the 1.5 Al steels, but did not have a significant effect on ferrite formation and the amount of retained austenite in the 1.0Al steels. Overall, the cumulative fraction of retained austenite, bainitic ferrite, and martensite was largely independent of the intercritical annealing and isothermal bainitic transformation conditions. The only significant difference is the amount of ferrite formation. Comparing the 1.5Al and 1.0Al steels shows that stronger ferrite formation occurred in the 1.5Al steels, regardless of the heat treatment conditions. In addition, as also shown in Figure 5.1, the 1.0Al_35% γ 60s steel contained the largest amount of martensite.

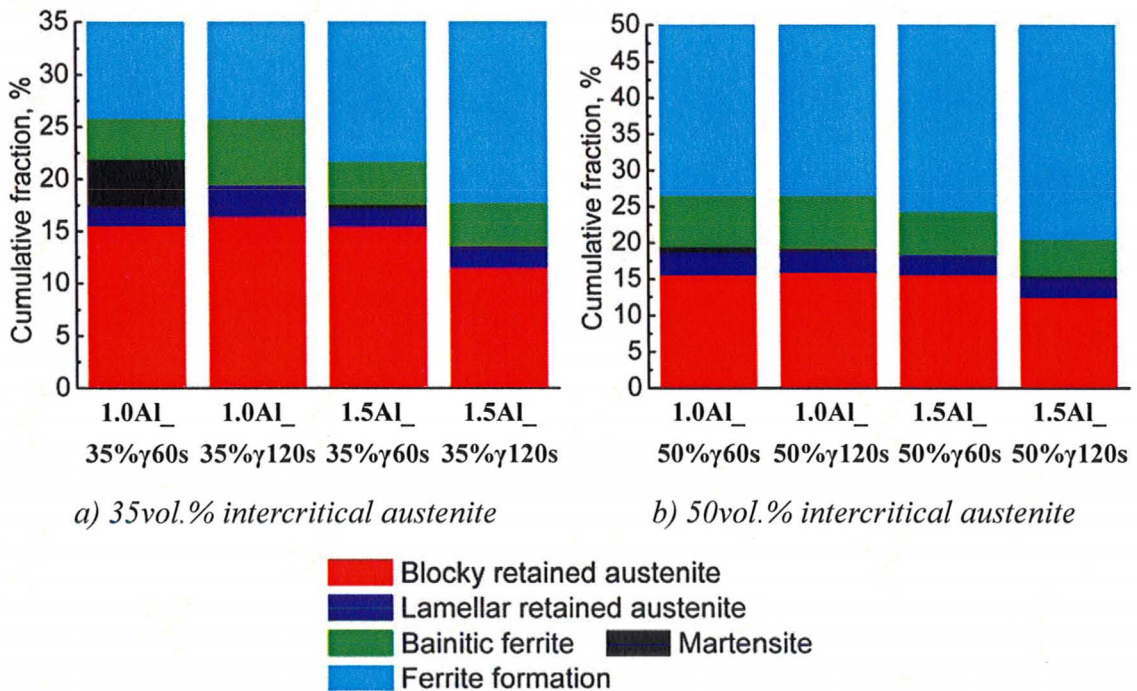


Figure 5.2 Phase constituents of the as-annealed steels excluding intercritical ferrite

5.1.2 Retained Austenite Characteristics

The retained austenite carbon content for all as-annealed steels is summarized in Table 5.1. These results were obtained through X-ray diffraction and equation (4.1) as described in §4.3.2. The data in Table 5.1 did not show a significant difference in the retained austenite carbon contents for all steels except for the 1.5Al_{35%}γ120s steel, which possibly contained retained austenite of slightly higher carbon content. Generally speaking, heat treatment conditions, either intercritical annealing or isothermal bainitic transformation, and alloy compositions did not have a significant effect on the carbon content of the retained austenite.

Table 5.1 *The carbon content of retained austenite (RA)*

Steel	wt% of C in RA	Steel	wt% of C in RA
1.0Al _{35%} γ60s	1.22	1.0Al _{50%} γ60s	1.19
1.0Al _{35%} γ120s	1.24	1.0Al _{50%} γ120s	1.24
1.5Al _{35%} γ60s	1.22	1.5Al _{50%} γ60s	1.29
1.5Al _{35%} γ120s	1.38	1.5Al _{50%} γ120s	1.30

The size of blocky and lamellar retained austenite, summarized in Table 5.2, was

obtained through image analysis. The equivalent circular diameter, thread length and thread width were defined in §4.3.3. From Table 5.2, it can be seen that the average retained austenite grain size was similar for all steels regardless of composition and thermal processing conditions. Table 5.2 also shows that the average grain size was in the micron to sub-micron range and the aspect ratio of the lamellar retained austenite was relatively constant for all steels.

Table 5.2 *The dimensions of retained austenite*

Steel	Blocky Retained Austenite	Lamellar Retained Austenite		
	Average equivalent circular diameter (μm)	Average Thread length (μm)	Average Thread width (μm)	Aspect ratio (Length/Width)
1.0Al_35% γ 60s	0.80	1.24	0.13	9
1.0Al_35% γ 120s	0.82	1.06	0.12	9
1.0Al_50% γ 60s	0.67	0.98	0.13	8
1.0Al_50% γ 120s	0.69	0.98	0.13	8
1.5Al_35% γ 60s	0.63	1.06	0.12	9
1.5Al_35% γ 120s	0.58	0.97	0.12	8
1.5Al_50% γ 60s	0.70	1.35	0.15	9
1.5Al_50% γ 120s	0.66	1.35	0.16	8

5.1.3 Monotonic Tensile Properties

Monotonic tensile tests were performed for each experimental alloy to determine true stress-true strain curves, and were then used to determine yield strength, true ultimate tensile strength and uniform elongation. To ensure that the tensile properties derived represented the true mechanical behaviour, three tensile tests were performed for each steel, as shown in Figure 5.3. It can be seen that the three tests for each steel were very repeatable. All tensile curves exhibited yield point elongation. Comparing the steels of the same alloy chemistry and thermal processing but with varying bainitic transformation hold times shows that the yield elongation increased with increasing the bainitic transformation hold time, i.e. from 60s to 120s, except for the 1.5Al_50% γ 60s and 1.5Al_50% γ 120s steels which exhibited similar yield elongations.

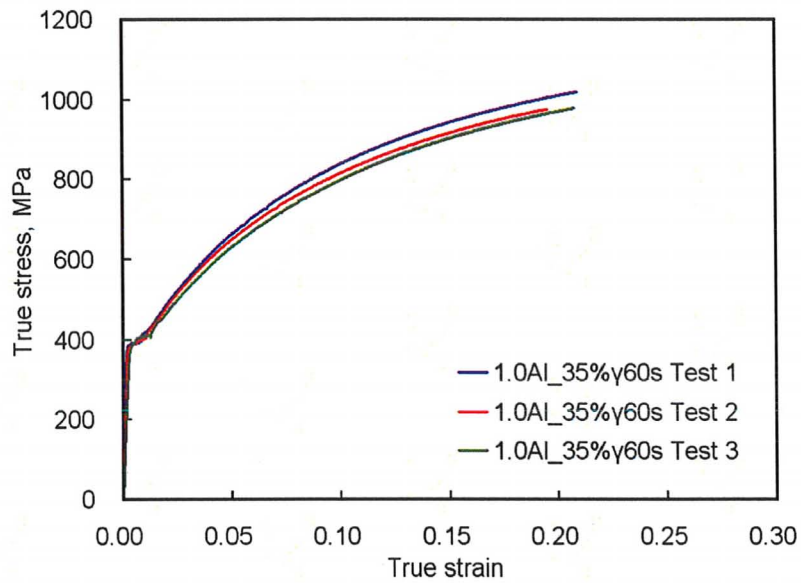
An average value of yield strength, true ultimate tensile strength (UTS) and uniform elongation (ϵ_u) was determined based on the three tests for each steel. Since the product of UTS and ϵ_u can be used to indicate the ability of a material to absorb deformation energy, an average of $UTS \times \epsilon_u$ for each steel was also calculated. These values are summarized in Table 5.3. It can be seen that the average yield strength exhibited a similar trend to the yield elongation, i.e. the yield strength increased with increasing the bainitic transformation hold time, except for the 1.5Al_50% γ 60s and

1.5Al_{50%}γ120s steels which exhibited comparable yield strengths.

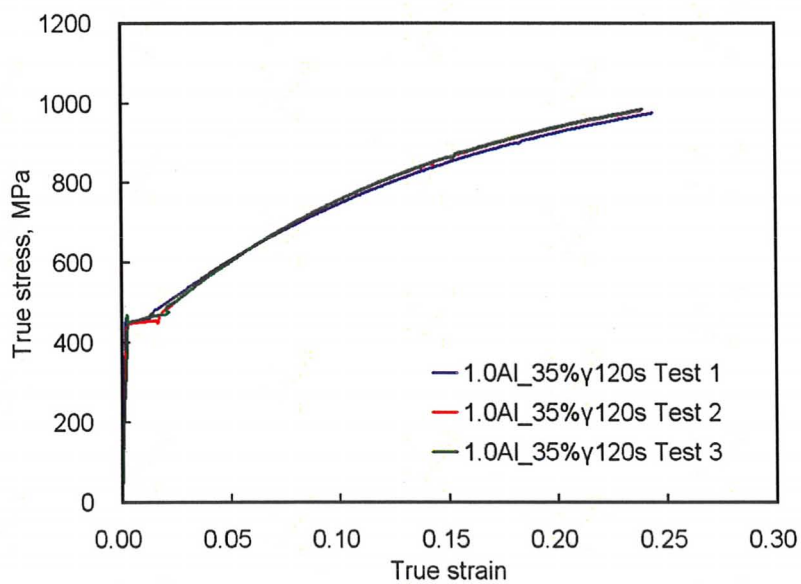
Table 5.3 Average yield strength, UTS, ϵ_u , and UTS \times ϵ_u of the experimental steels

Steel	Average yield strength (MPa)	Average UTS (MPa)	Average ϵ_u	Average UTS \times ϵ_u (MPa)
1.0Al _{35%} γ60s	384	991	0.21	203
1.0Al _{35%} γ120s	448	981	0.24	236
1.0Al _{50%} γ60s	410	965	0.23	219
1.0Al _{50%} γ120s	440	946	0.24	231
1.5Al _{35%} γ60s	428	910	0.22	200
1.5Al _{35%} γ120s	468	908	0.24	220
1.5Al _{50%} γ60s	425	885	0.27	235
1.5Al _{50%} γ120s	433	868	0.28	240

For the 1.0Al steels, the UTS of the 35% intercritical austenite steels was higher than that of the 50% intercritical austenite steels, but the ϵ_u was not significantly affected. The longer bainitic transformation hold time (120 s) slightly decreased the UTS, but the ϵ_u was not strongly affected, except for the 1.0Al_{35%}γ60s steel compared with the 1.0Al_{35%}γ120s steel. The UTS of the 1.5Al steels was generally lower than that of the

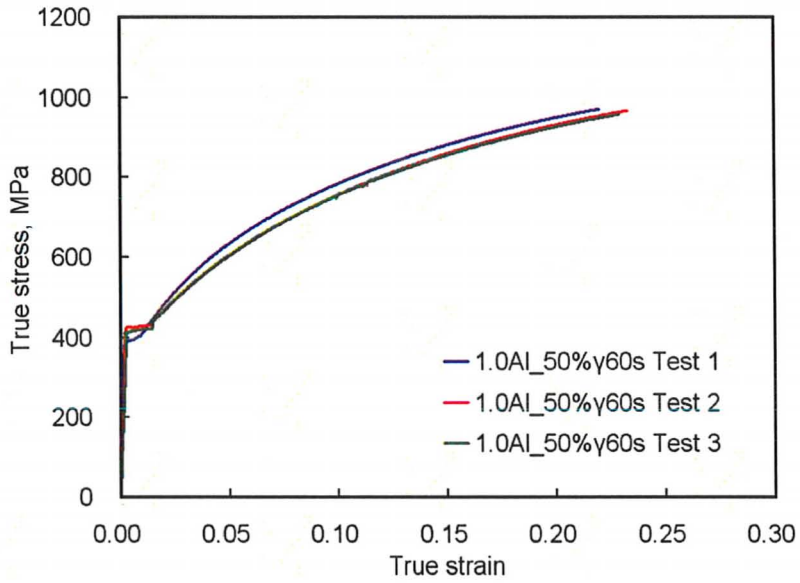


a) 1.0Al_35%γ60s

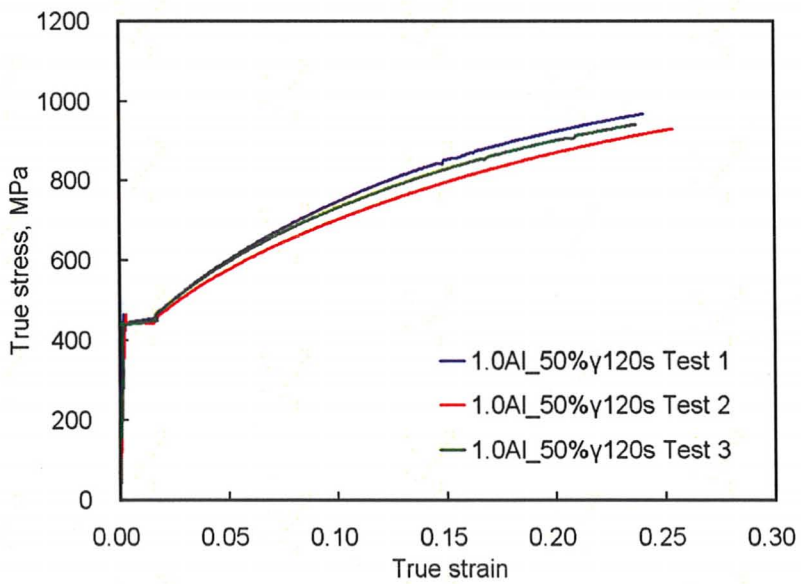


b) 1.0Al_35%γ120s

Figure 5.3 True stress-true strain curves of the as-annealed steels prior to the onset of necking

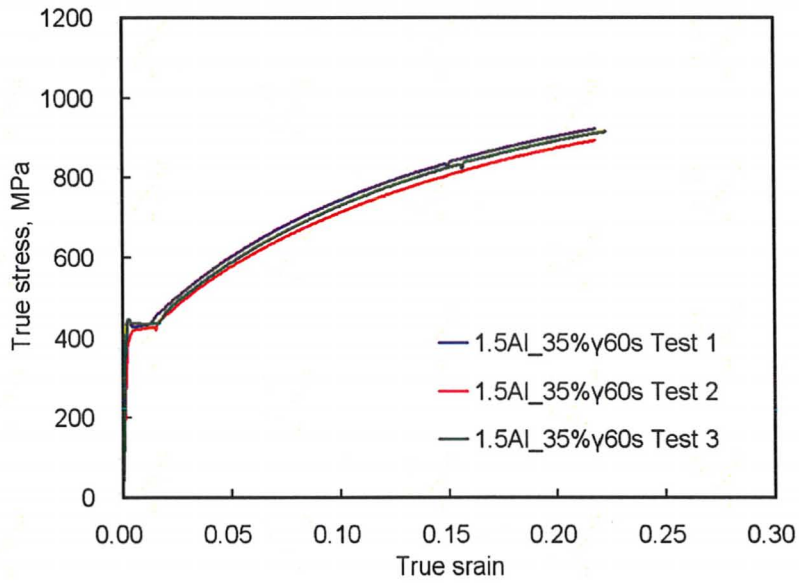


c) 1.0Al_50%γ60s

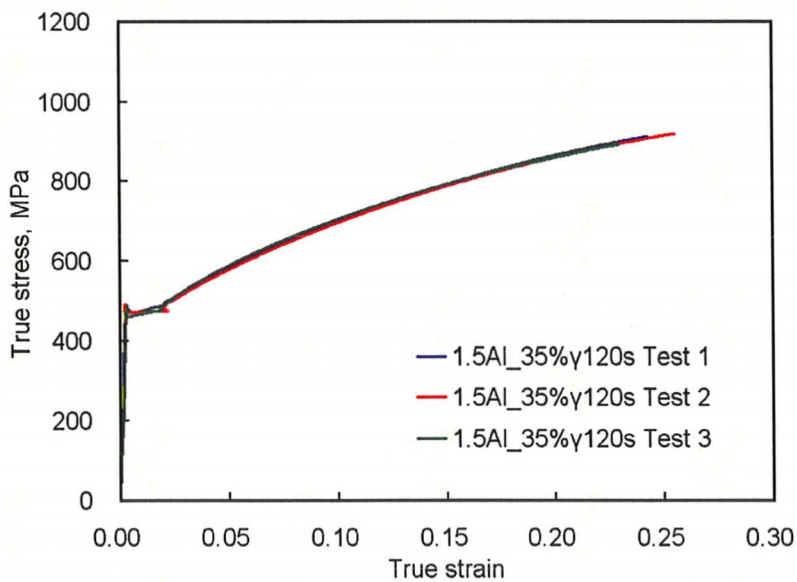


d) 1.0Al_50%γ120s

Figure 5.3 (cont'd) True stress-true strain curves of as-annealed steels prior to the onset of necking

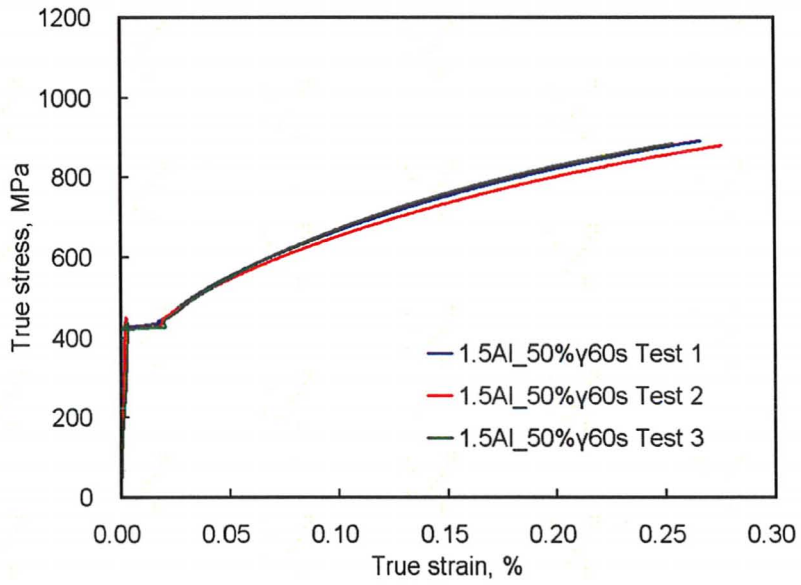


e) 1.5Al_35%γ60s

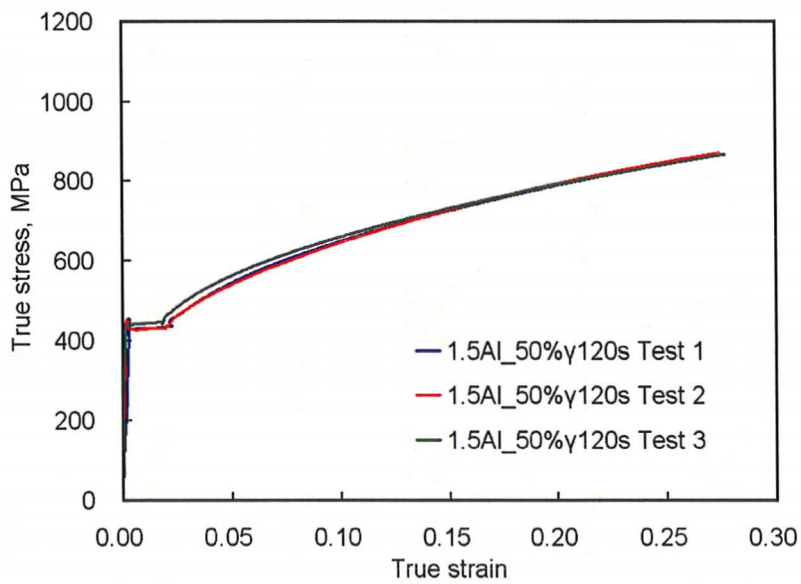


f) 1.5Al_35%γ120s

Figure 5.3 (cont'd) True stress-true strain curves of as-annealed steels prior to the onset of necking



g) 1.5Al_50%γ60s



h) 1.5Al_50%γ120s

Figure 5.3 (cont'd) True stress-true strain curves of as-annealed steels prior to the onset of necking

1.0Al steels. The ϵ_u of the 1.5Al steels with 50% intercritical austenite was larger than that of the 1.0Al steels, but it was not the case for the steels with 35% intercritical austenite. The higher intercritical annealing temperature (50% intercritical austenite) decreased the UTS and increased the ϵ_u of the 1.5Al steels. The effects of the bainitic transformation hold time on the UTS and ϵ_u of the 1.5Al steels were neither significant except for the UTS of the 1.5Al_50% γ 60s and 1.5Al_50% γ 120s steels.

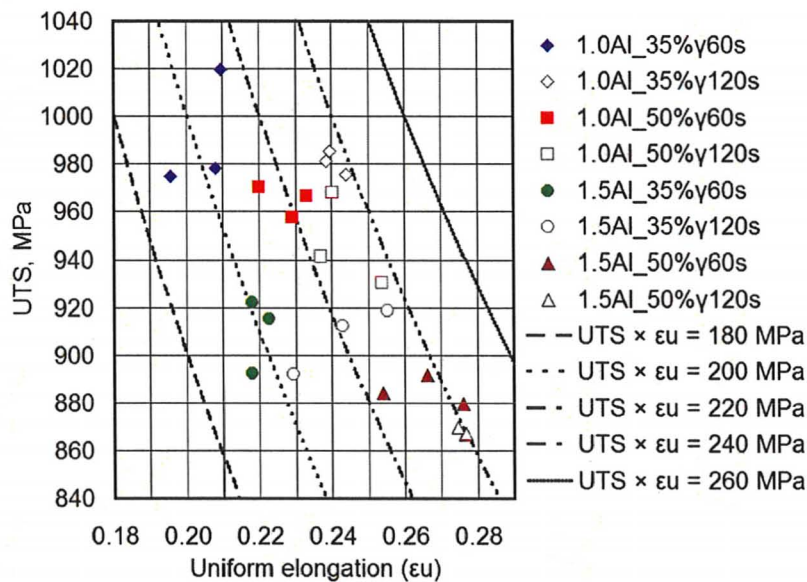
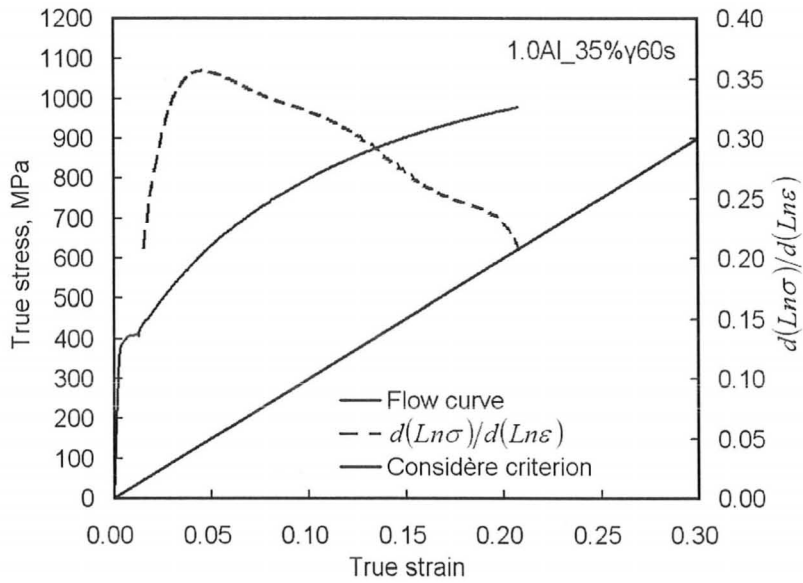


Figure 5.4 UTS and ϵ_u of the experimental steels

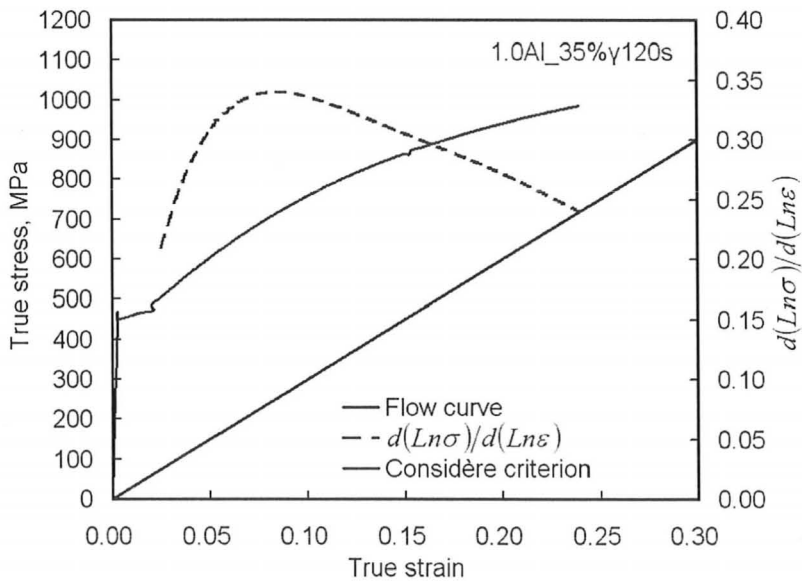
UTS and ϵ_u of the three tests for each steel are shown in Figure 5.4. Five products of UTS and ϵ_u (180 MPa, 200 MPa, 220 MPa, 240 MPa and 260 MPa) are shown as contours in Figure 5.4. As also shown in Table 5.3, the products of UTS and ϵ_u of most

steels ranged from 220 to 240 MPa. The 1.0Al_35% γ 60s and 1.5Al_35% γ 60s steels exhibited slightly lower $UTS \times \epsilon_u$, ~200 MPa. Among the three tests for each steel, the test that showed a $UTS \times \epsilon_u$ close to the average for the steel (Table 5.3) was chosen as the “representative” test of the steel for the following calculations and discussion.

The incremental work hardening coefficient ($n_{incr} = d(Ln\sigma)/d(Ln\epsilon)$) was calculated using the tensile curve of the “representative” test for each steel. The results are shown in Figure 5.5. It can be seen that the incremental work hardening coefficients evolved in different ways depending on the alloys and heat treatments. The two extremes are represented by the 1.0Al_35% γ 60s and 1.5Al_50% γ 120s steels (Figure 5.5 a) and h)), respectively. For the 1.0Al_35% γ 60s steel, n_{incr} increased and reached a peak value quickly, but the subsequent decrease was also rapid, leading to a smaller uniform elongation of the steel. By contrast, n_{incr} of the 1.5Al_50% γ 120s steel evolved more smoothly and remained relatively constant for increasing strain. Accordingly, the steel had a larger uniform elongation. To have a better balance between strength and ductility for TRIP-assisted steels, the latter n_{incr} evolution (1.5Al_50% γ 120s) is more desirable. This result is confirmed by comparing the products of $UTS \times \epsilon_u$ of the two alloys (Figure 5.4 and Table 5.3).

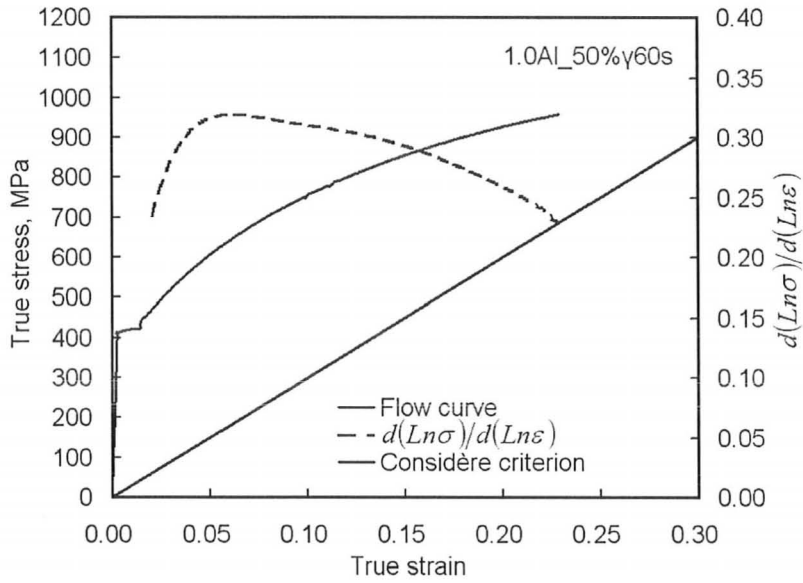


a) 1.0Al₃₅% γ 60s

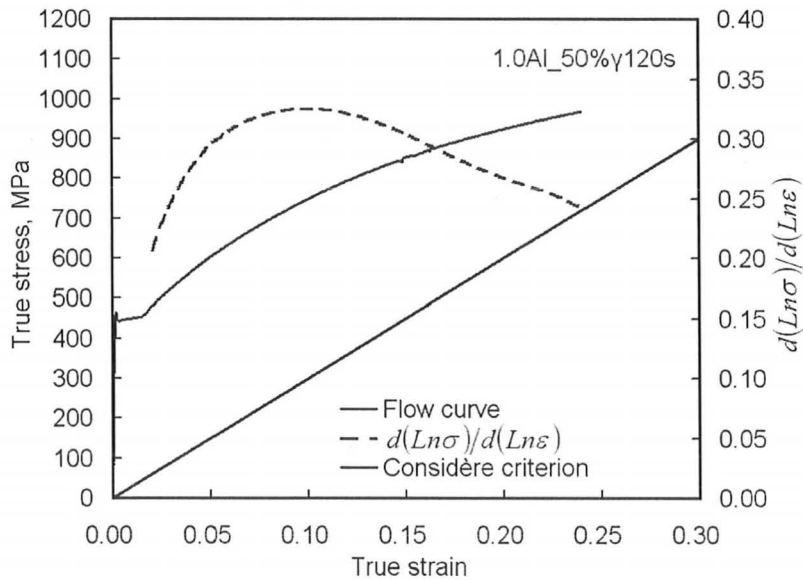


b) 1.0Al₃₅% γ 120s

Figure 5.5 Flow curves and incremental work hardening coefficients

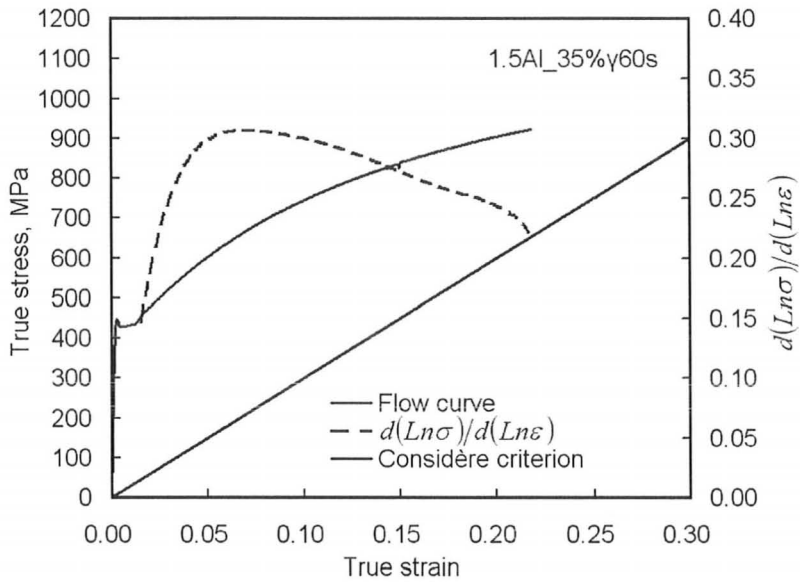


c) 1.0Al_{50%γ60s}

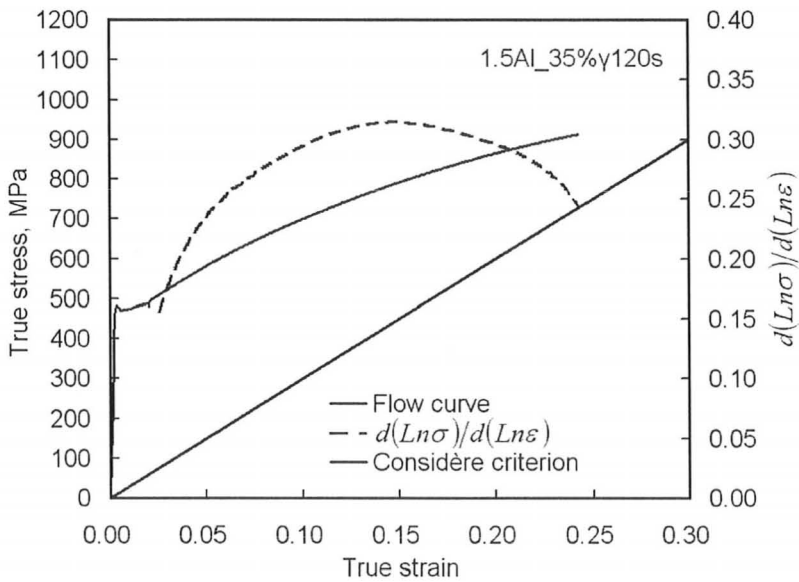


d) 1.0Al_{50%γ120s}

Figure 5.5 (cont'd) Flow curves and incremental work hardening coefficients

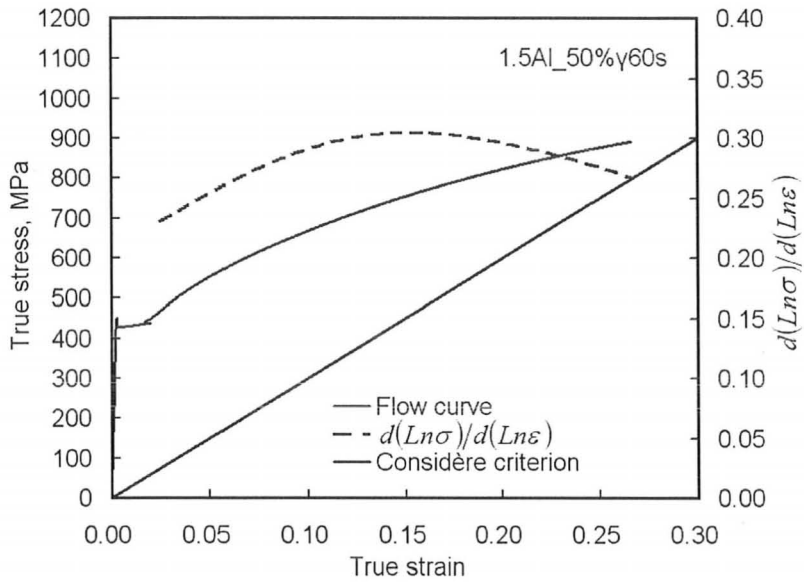


e) 1.5Al_35%γ60s

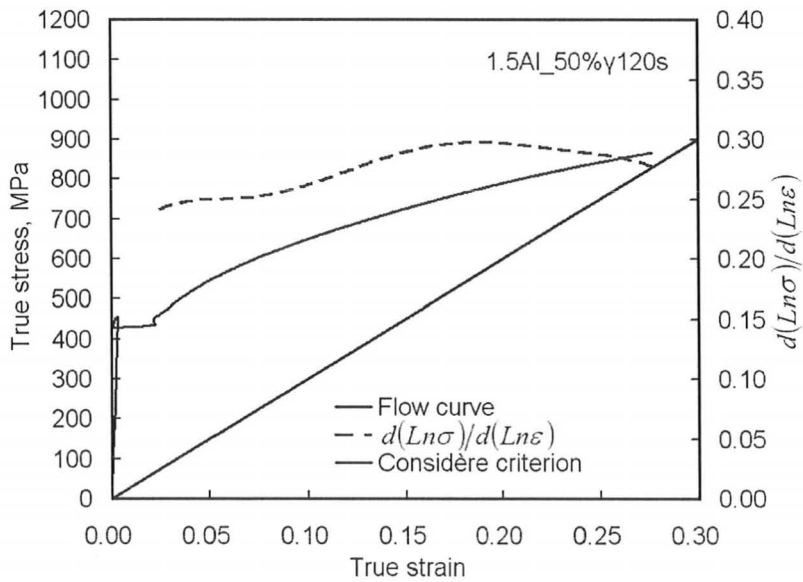


f) 1.5Al_35%γ120s

Figure 5.5 (cont'd) Flow curves and incremental work hardening coefficients



g) 1.5Al_50%γ60s



h) 1.5Al_50%γ120s

Figure 5.5 (cont'd) Flow curves and incremental work hardening coefficients

5.2 Strain-induced Martensite Transformation

5.2.1 Microstructural Evolution during Plastic Deformation

Retained austenite in TRIP-assisted steels transforms to martensite during plastic deformation. With the desired transformation occurring gradually with applied strain, a high work hardening rate is expected to be maintained in TRIP-assisted steels. Figure 5.6 gives an example of such microstructurally-observed transformation, where the 1.0Al_50% γ 60s steel was strained by $\epsilon=0.025$ and 0.050, respectively. Compared with the as-annealed 1.0Al_50% γ 60s steel (Figure 5.1 c)), Figure 5.6 shows that the fraction of martensite in the steel increased with increasing the strain. Figure 5.7 presents two SEM micrographs of the strained 1.0Al_50% γ 60s steel ($\epsilon=0.100$) at a lower and higher magnification, respectively. It can be seen that lamellar retained austenite (RA_L) was more resistant to plastic deformation since most of blocky retained austenite (RA_B) has previously transformed to martensite whereas lamellar retained austenite has not. Figure 5.8 gives an example of the microstructure of the 1.0Al_50% γ 120s steel strained to 0.200. It indicates that most of retained austenite has transformed to martensite, including lamellar retained austenite (Figure 5.8 b)).

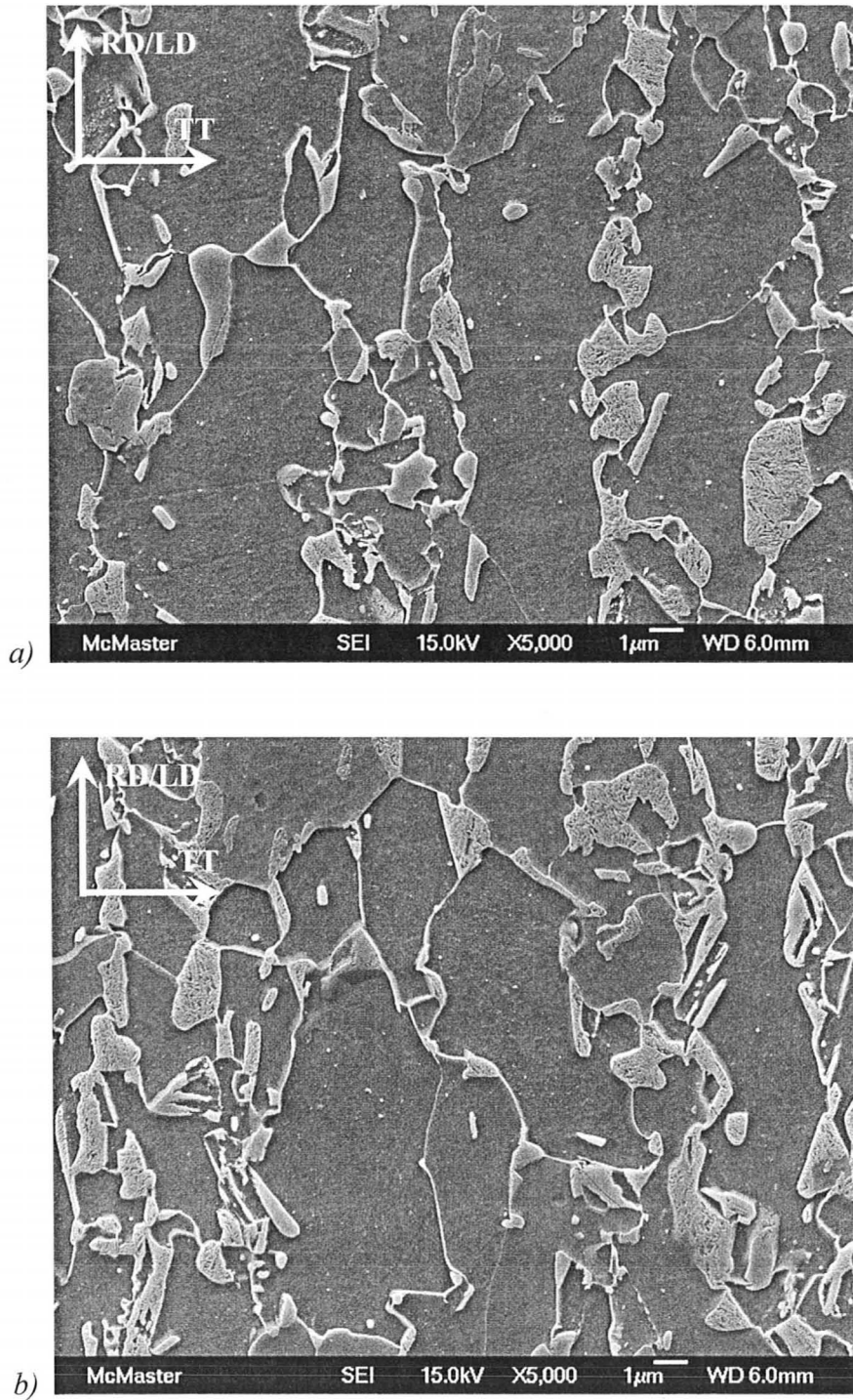
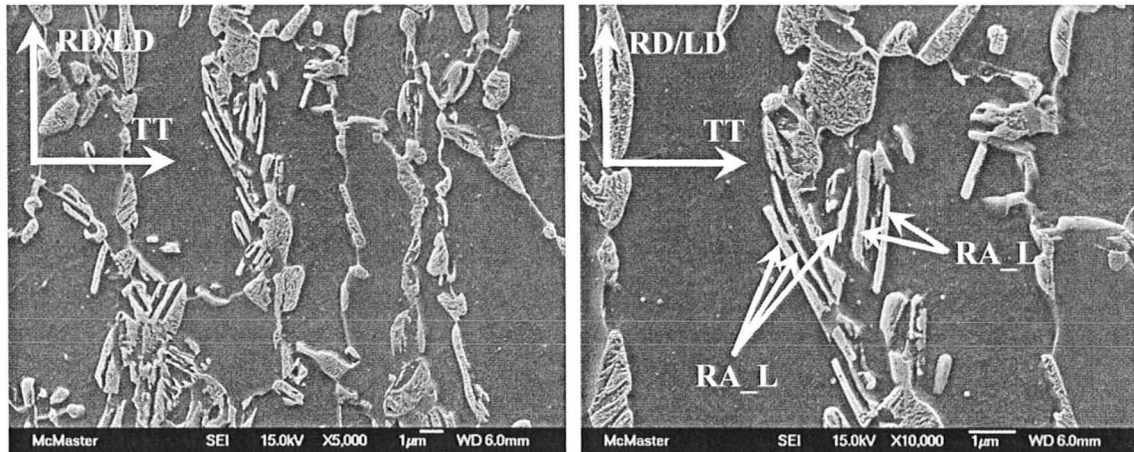


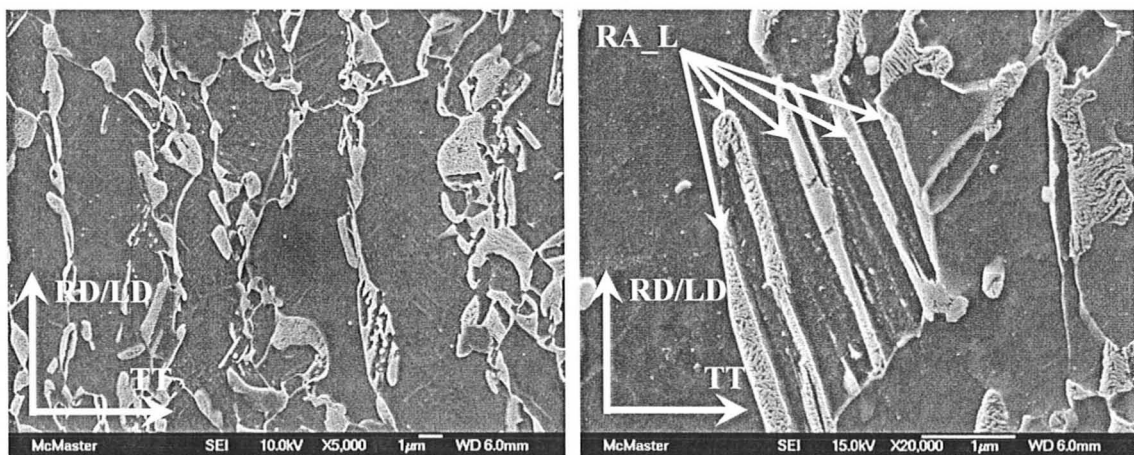
Figure 5.6 SEM micrographs of the strained 1.0Al_{50%}γ60s steel: a) $\epsilon=0.025$, b) $\epsilon=0.050$ (RD: rolling direction, LD: loading direction, TT: through thickness)



a) lower magnification

b) higher magnification

Figure 5.7 SEM micrographs of the strained 1.0Al_{50%}γ60s steel, $\epsilon=0.100$
 (RD: rolling direction, LD: loading direction, TT: through thickness,
 RA_L: lamellar retained austenite)

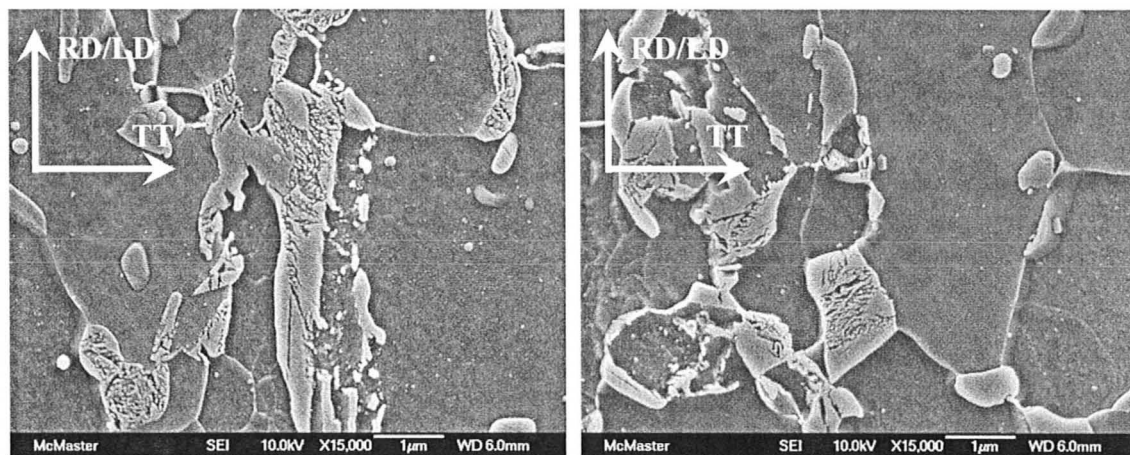


a) lower magnification

b) higher magnification

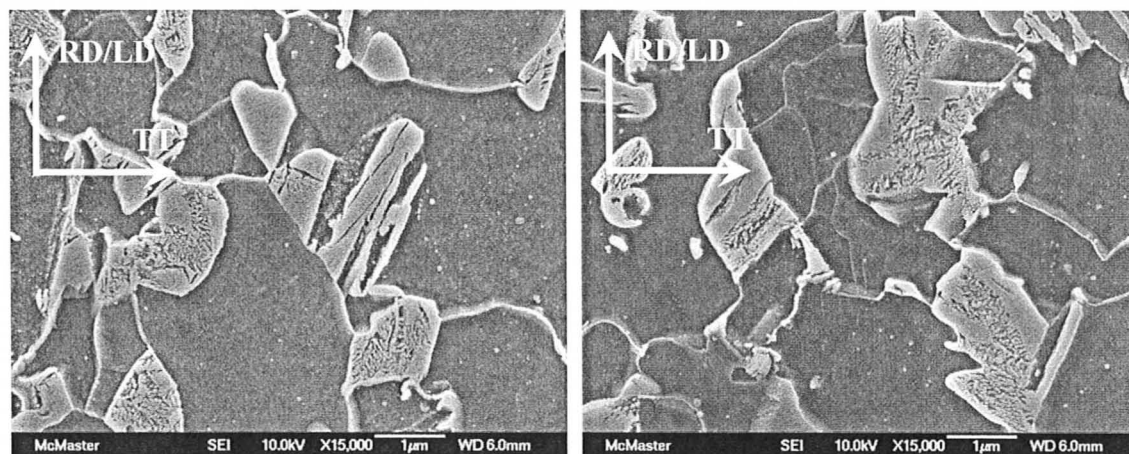
Figure 5.8 SEM micrographs of the strained 1.0Al_{50%}γ120s steel, $\epsilon=0.200$
 (RD: rolling direction, LD: loading direction, TT: through thickness,
 RA_L: lamellar retained austenite)

A difference in the observed evolution of the microstructures between the 1.0 and 1.5Al steels is that a significant quantity of partially-transformed retained austenite grains were observed in the 1.0Al steels (Figure 5.9), but such partially-transformed retained austenite grains were rarely observed in the 1.5Al steels (Figure 5.10). From this, it seems that step-by-step transformation inside some retained austenite grains contributed more to the continuous increase of martensite in the 1.0Al steels than in the 1.5Al steels during plastic deformation. Jacques et al. (2001d) also reported partially-transformed retained austenite grains in their 0.29C-1.42Mn-1.41Si (wt.%) TRIP-assisted steels. They stated that this step-by-step transformation in one retained austenite grain was due to the autocatalytic effect.



a) 1.0Al_35%γ60s

b) 1.0Al_35%γ120s



c) 1.0Al_50%γ60s steel

d) 1.0Al_50%γ120s

Figure 5.9 SEM micrographs of the strained 1.0Al steels showing partially-transformed retained austenite grains, $\epsilon=0.025$ (RD: rolling direction, LD: loading direction, TT: through thickness)

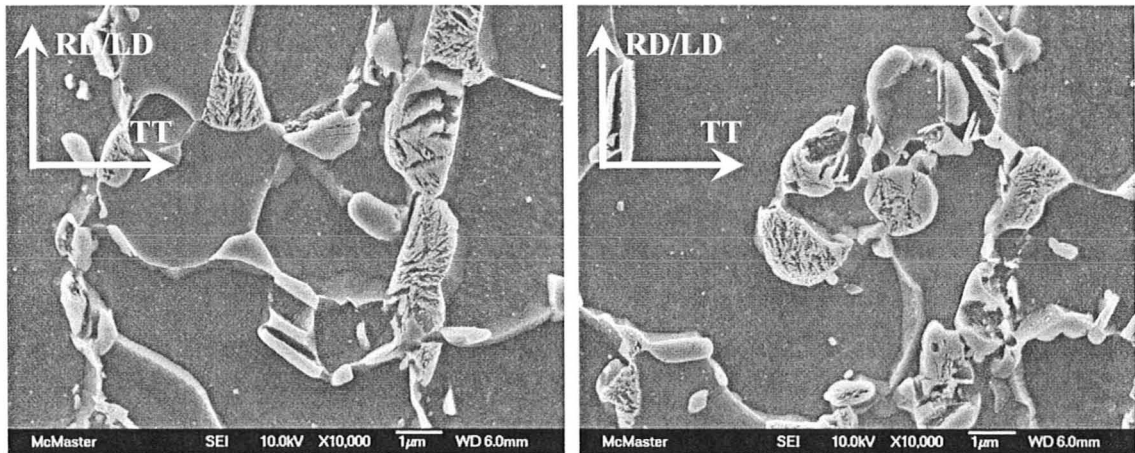
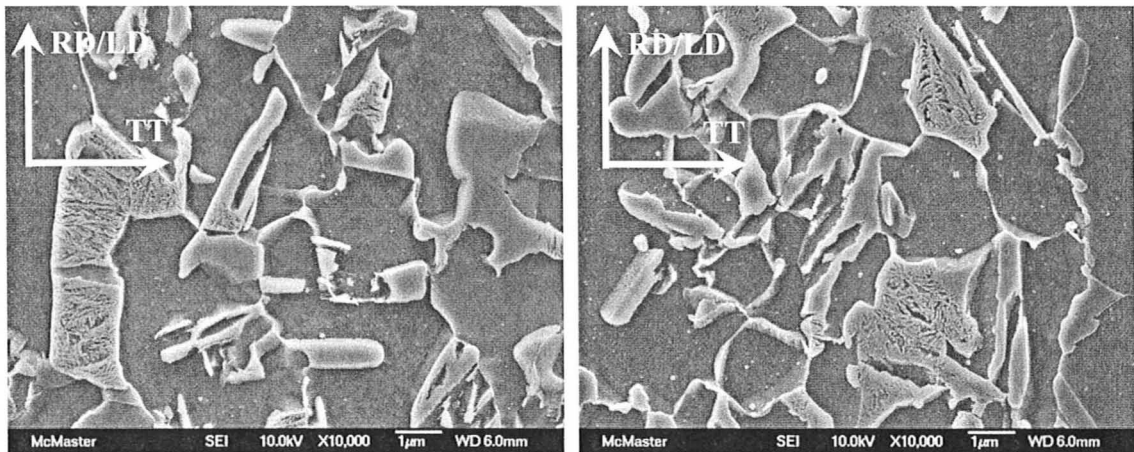
a) 1.5Al_35% γ 60sb) 1.5Al_35% γ 120sc) 1.5Al_50% γ 60sd) 1.5Al_50% γ 120s

Figure 5.10 SEM micrographs of the strained 1.5Al steels showing partially-transformed retained austenite grains were rarely observed, $\epsilon=0.025$ (RD: rolling direction, LD: loading direction, TT: through thickness)

5.2.2 Transformation of Retained Austenite to Martensite vs. Plastic Strain

Further to the last section, this section will quantitatively examine the phase transformation from retained austenite to martensite as a function of plastic strain using both X-ray diffraction and image analysis. The results of these two techniques are compared in Figure 5.11. As can be seen, the absolute values obtained through X-ray diffraction and image analysis did not coincide at lower strains, although it should be noted that the trends were similar. The TOPAS program gave the XRD errors which were relatively small, as shown in Figure 5.11, but these errors were not very reliable because several possible experimental errors occurring in the X-ray diffraction analysis made it difficult to quantify the total error in the XRD measurements [Zhao et al. (2001)].

The first drawback of X-ray diffraction when applied to TRIP-assisted steels is that the high carbon content in retained austenite could affect the integrated intensity of a diffraction peak [De Meyer et al. (1999b)]. For a randomly oriented sample, the integrated intensity from a diffraction peak is given by

$$I_{hkl} = KR_{hkl}V \quad (5.1)$$

where K is the instrument factor independent of the sample, V is the volume fraction of the analyzed phase, and R_{hkl} is a material specific factor. The composition of the analyzed phase affects the value of R_{hkl} . However, R_{hkl} values are usually calculated without

considering changes due to the high carbon concentration of retained austenite in TRIP-assisted steels. Moreover, carbon distribution is not homogeneous within the retained austenite phase. Secondly, when calculating the integrated intensity of a diffraction peak, it is difficult to take into account the effect of a crystallographic texture in the retained austenite phase of TRIP-assisted steels [De Meyer et al. (1999b)]. Thirdly, the stress condition on the sample surface causes broadening of the diffraction peaks from retained austenite, and consequently influences the calculated volume fraction [Zhao et al. (2001)]. By contrast, image analysis can avoid the above disadvantages. In addition, the image analysis technique allows differentiation between blocky retained austenite and lamellar retained austenite and also gives information about ferrite, bainitic ferrite and martensite. This suggests that image analysis is more advantageous. Thus, only the image analysis results will be discussed in the following sections. The drawback of image analysis is that it does not give information on the carbon content in retained austenite, which needs to be measured using X-ray diffraction, and also is subject to significant sampling errors. These latter were addressed somewhat through selection of six “random” fields in the present work.

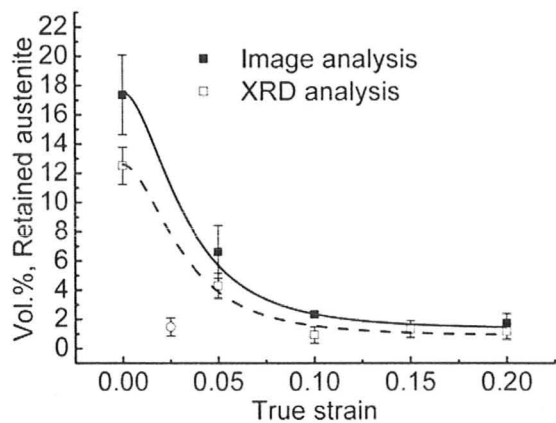
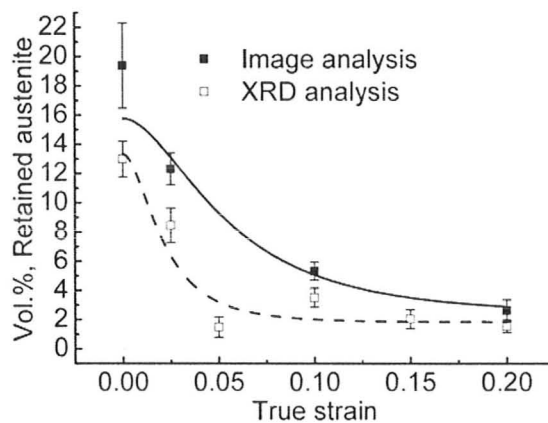
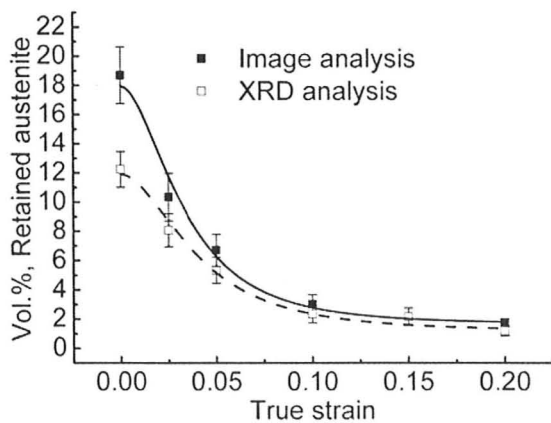
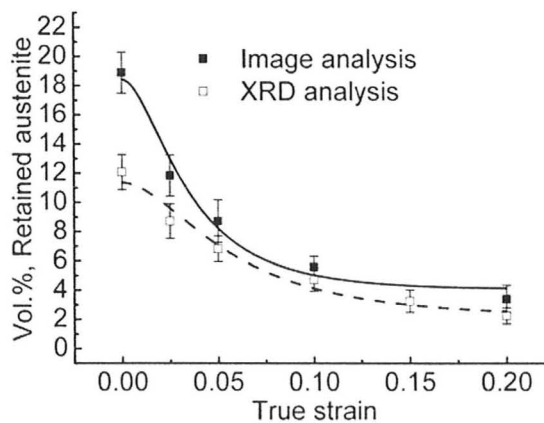
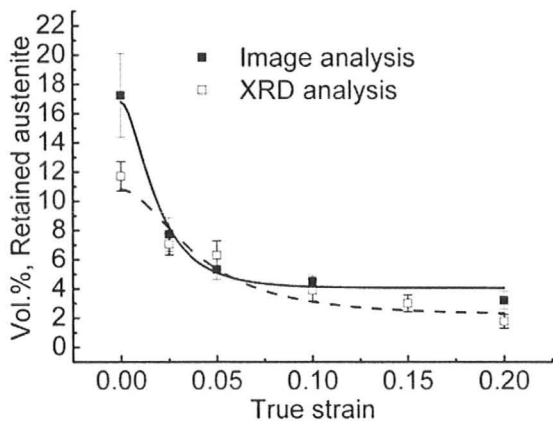
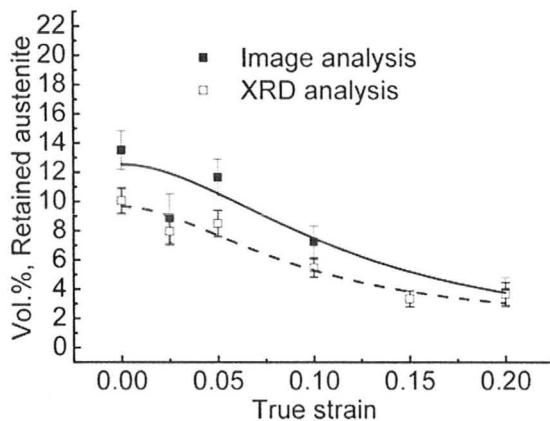
a) 1.0Al_35% γ 60sb) 1.0Al_35% γ 120sc) 1.0Al_50% γ 60sd) 1.0Al_50% γ 120s

Figure 5.11 Volume fraction of retained austenite as a function of strain

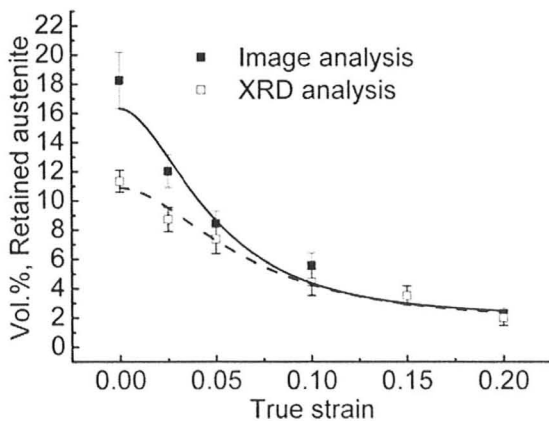
(The open circle in the graph of a) 1.0Al_35% γ 60s was not used for fitting because of too much scattering.)



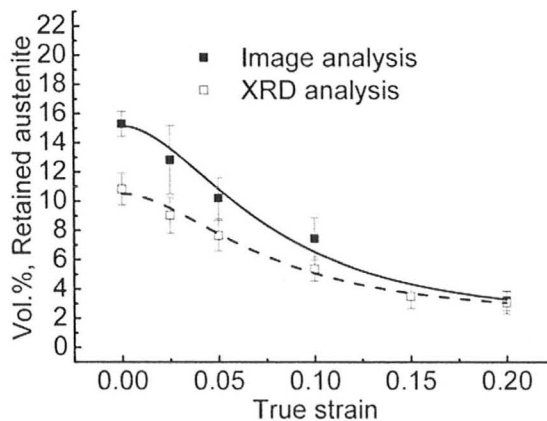
e) 1.5Al_35%γ60s



f) 1.5Al_35%γ120s



g) 1.5Al_50%γ60s



h) 1.5Al_50%γ120s

Figure 5.11 (cont'd) Volume fraction of retained austenite as a function of strain

Although discrepancies existed between the X-ray diffraction and image analysis results, Figure 5.11 shows that the volume fraction of retained austenite in the 1.0Al and 1.5Al steels generally evolved in different ways as a function of plastic deformation. The volume fraction of retained austenite in the 1.5Al steels evolved more smoothly except for the 1.5Al_35% γ 60s steel.

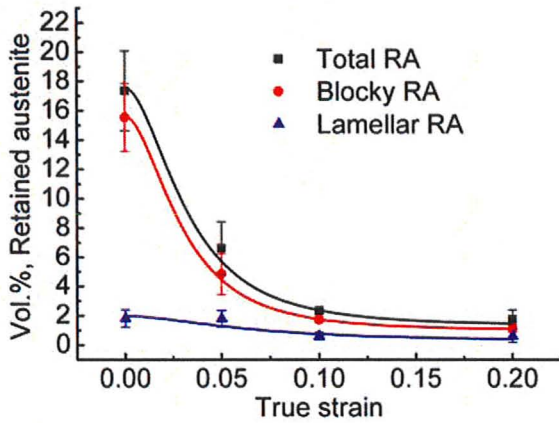
As has been pointed out, further information about retained austenite in two morphologies can be derived using image analysis. Figure 5.12 presents the evolution of the volume fraction of blocky and lamellar retained austenite, as well as the total (blocky + lamellar) retained austenite. It can be seen, for all steels, that the lamellar retained austenite was more resistant to plastic deformation than the blocky retained austenite, which implies a higher stability of the lamellar retained austenite. This is in agreement with what was observed in Figures 5.7 and 5.8. Although the lamellar retained austenite possessed a higher stability, which is desirable for an optimum TRIP effect, the amount of the lamellar retained austenite was very limited, as shown in Figure 5.12. Thus, the transformation of the blocky retained austenite made the primary contribution to the TRIP effect.

Several features of the transformation from retained austenite to martensite versus plastic deformation can be observed from Figure 5.12. For the 1.0Al steels, most of the retained austenite transformed before the 0.10 strain, after which little trans-

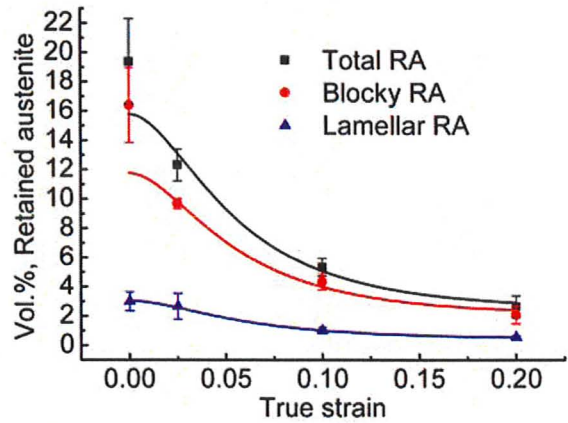
formation took place. Very little retained austenite was left in the 60s bainitic transformation hold time steels strained to 0.20 (1.0Al_35% γ 60s and 1.0Al_50% γ 60s); relatively more retained austenite was left in the 120s steels (1.0Al_35% γ 120s and 1.0Al_50% γ 120s). In all cases, the retained austenite transformation kinetics of the 1.0Al steels followed a sigmoidal curve. For the 1.5Al steels except for the 1.5Al_35% γ 60s sample, the retained austenite to martensite transformation did not take place as quickly as the case of the 1.0Al steels. Furthermore, the amount of untransformed retained austenite was significant for all heat treatments. Although the 1.5Al_35% γ 60s steel exhibited faster transformation kinetics compared with the other three 1.5Al steels, the amount of untransformed retained austenite was also significant.

Figure 5.13 shows the evolution of martensite as a function of strain, where each graph compares two steels which were heat treated with different bainitic transformation hold times, i.e. 60 s and 120 s. This evolution is actually the reverse one of retained austenite shown in Figure 5.12. Thus, a rapid decrease of retained austenite in Figure 5.11 corresponds to a rapid increase of martensite in Figure 5.13.

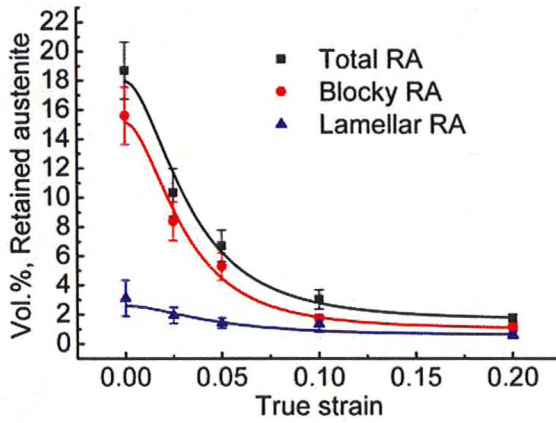
It should be noted that the transformation kinetics in all cases shown in Figures 5.11, 5.12 and 5.13 were fitted using the model of Olson and Cohen (1975). Detailed discussion concerning this modeling will be presented in Chapter 6.



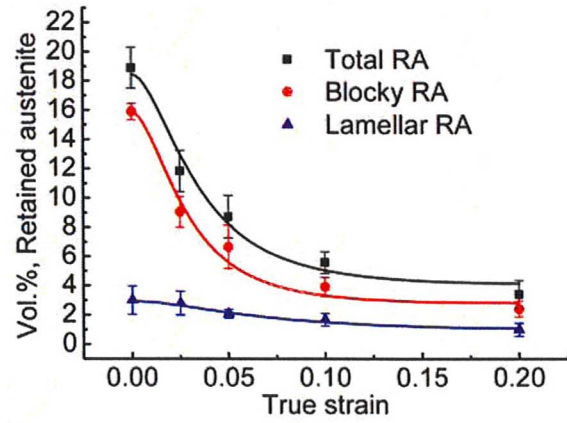
a) 1.0Al_35%γ60s



b) 1.0Al_35%γ120s

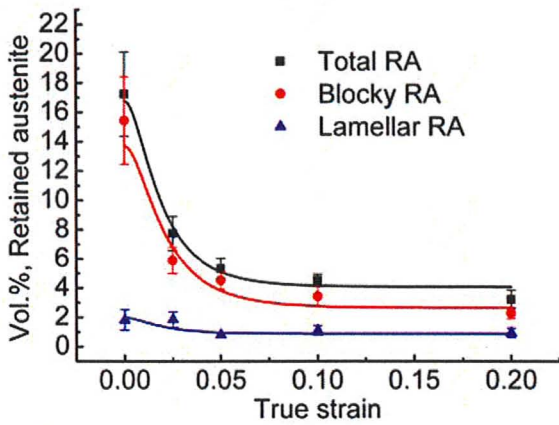


c) 1.0Al_50%γ60s

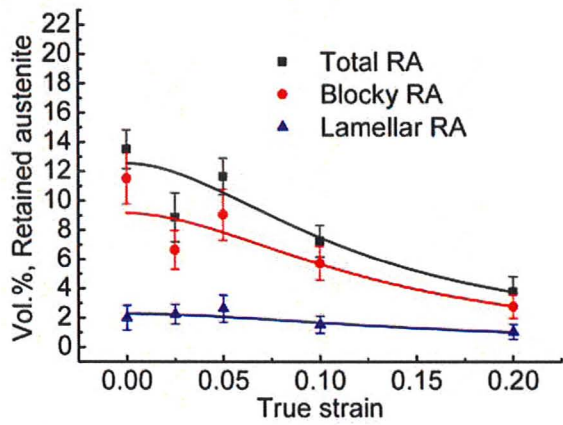


d) 1.0Al_50%γ120s

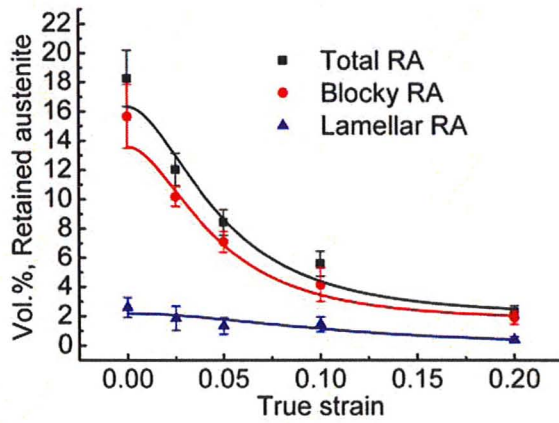
Figure 5.12 Volume fraction of total, blocky and lamellar retained austenite as a function of strain



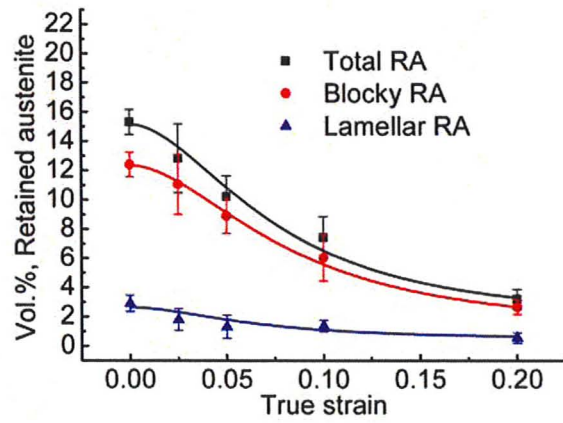
e) 1.5Al_35%γ60s



f) 1.5Al_35%γ120s

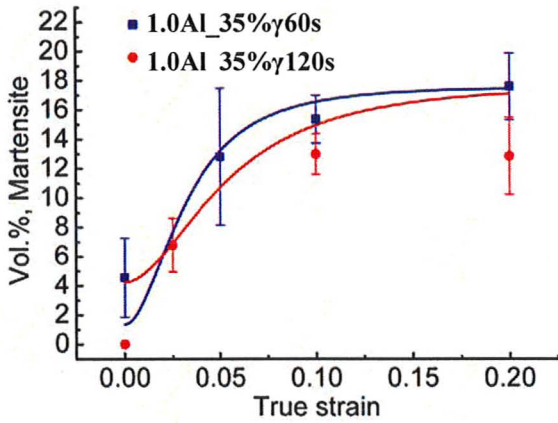


g) 1.5Al_50%γ60s

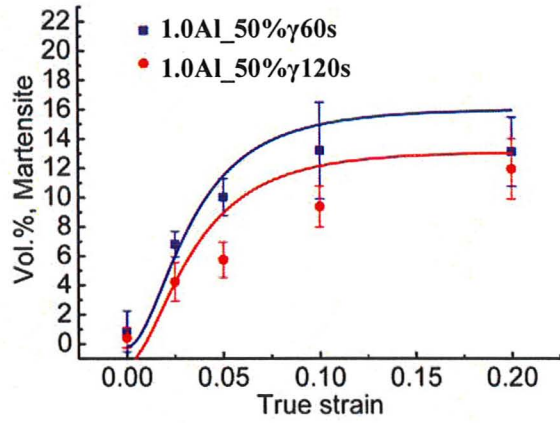


h) 1.5Al_50%γ120s

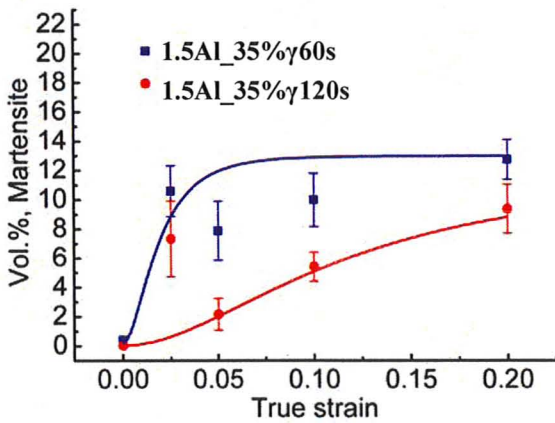
Figure 5.12 (cont'd) Volume fraction of total, blocky and lamellar retained austenite as a function of strain



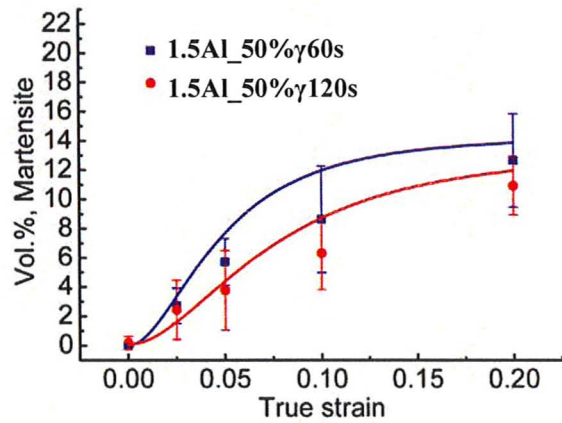
a) 1.0Al_35%γ60s and 1.0Al_35%γ120s



b) 1.0Al_50%γ60s and 1.0Al_50%γ120s



c) 1.5Al_35%γ60s and 1.5Al_35%γ120s



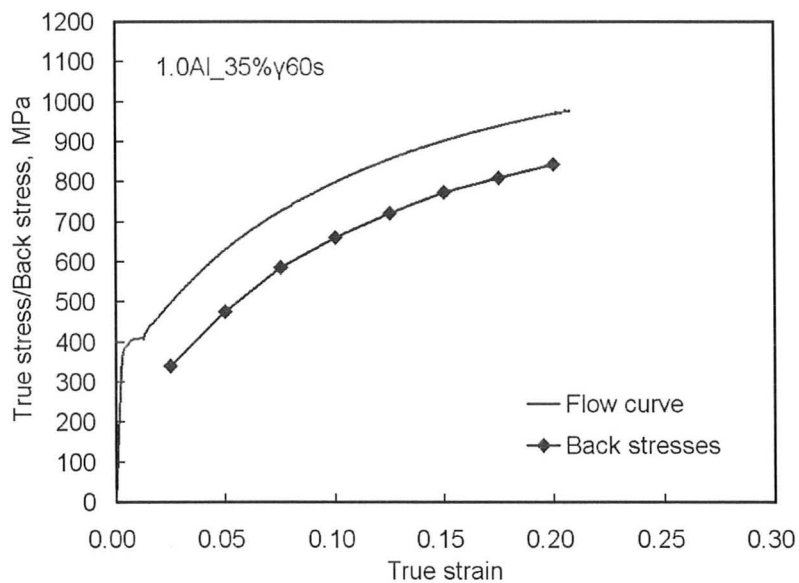
d) 1.5Al_50%γ60s and 1.5Al_50%γ120s

Figure 5.13 Volume fraction of martensite as a function of strain

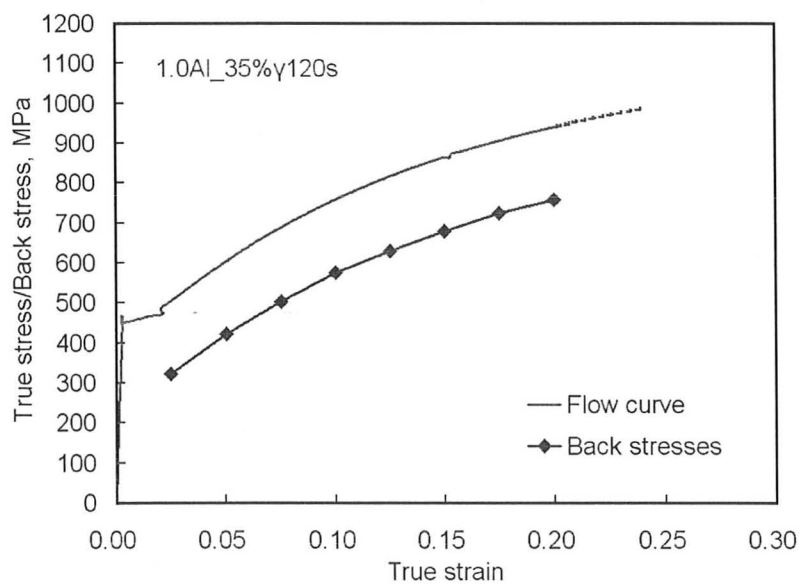
5.2.3 Kinematic Hardening

In §2.3, it was discussed that incompatible deformation occurring in plastically-deformed materials causes back stresses, which contribute a kinematic hardening component to the overall work hardening. In the special case of TRIP-assisted steels, the development of back stresses was expected to be more complicated due to the transformation of retained austenite to martensite accompanying the plastic deformation.

The back stresses measured using unloading/reloading tests for all experimental steels are presented in Figure 5.14, where the monotonic tensile flow curve (the true stress-true strain curve prior to the onset of necking) of the “representative” test for each steel was superimposed to compare the evolution of kinematic hardening and flow stress. It can be seen that, in all cases, the value of back stresses continuously increased with the flow stress up to strains as large as 0.20. No significant back stress saturation, which occurred in the dual phase steel shown in Figure 2.19, was observed at either lower or higher strains. It implies that, as expected, the development of back stresses in TRIP-assisted steels is very different from that of dual phase steels. This difference arises from the microstructural evolution of the TRIP-assisted steel, i.e. the TRIP effect. It is clear that kinematic hardening remained a significant contributor to the overall work hardening of the experimental TRIP-assisted steels at all stress/strain levels. This continuous

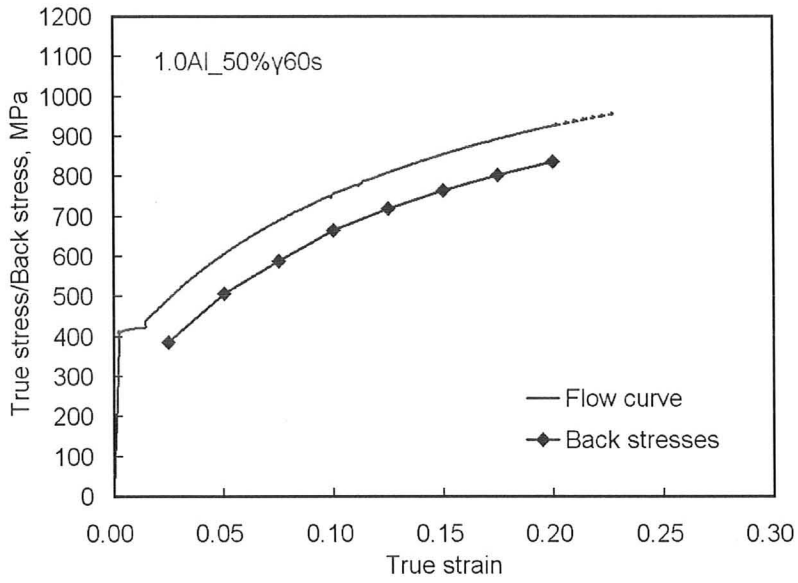


a) 1.0Al₃₅% γ 60s

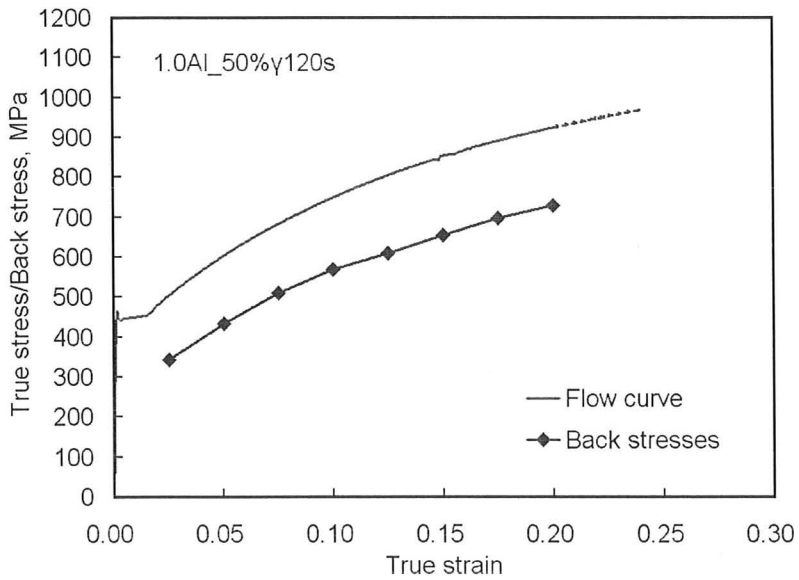


b) 1.0Al₃₅% γ 120s

Figure 5.14 Kinematic hardening (back stresses) vs. flow stresses

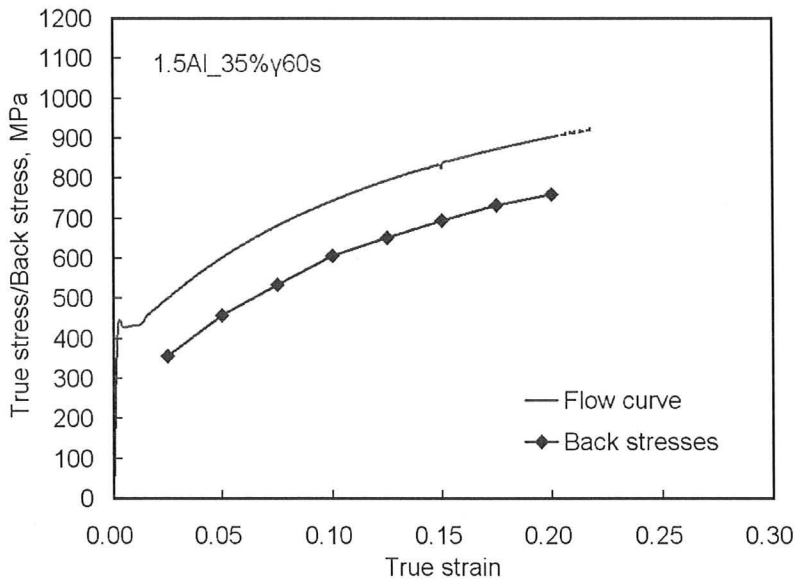


c) 1.0Al_50% γ 60s

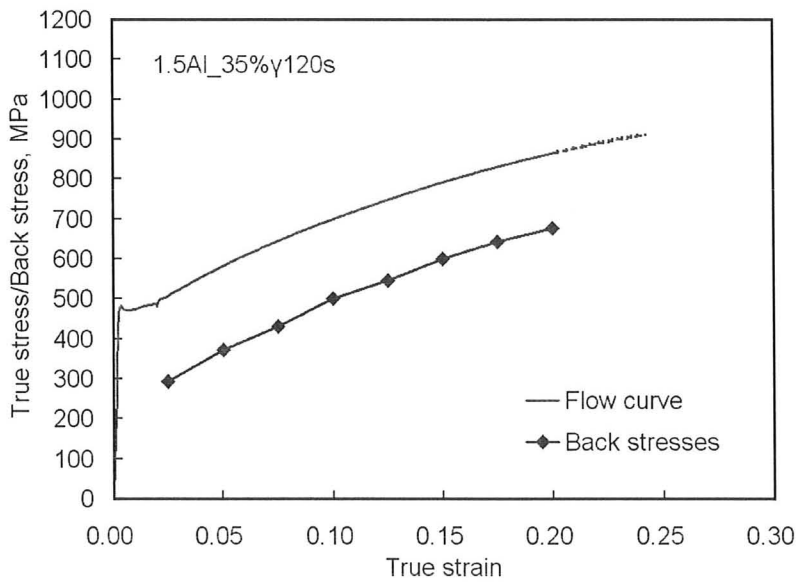


d) 1.0Al_50% γ 120s

Figure 5.14 (cont'd) Kinematic hardening (back stresses) vs. flow stresses

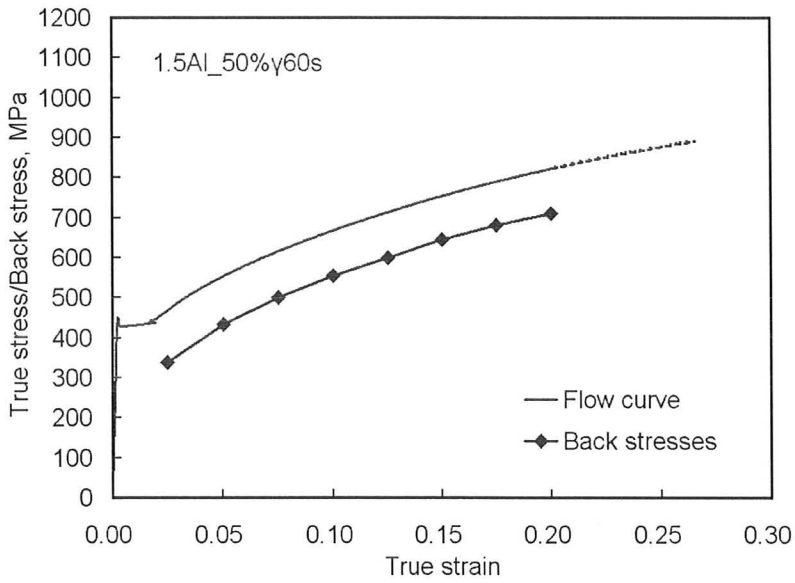


e) 1.5Al_35%γ60s

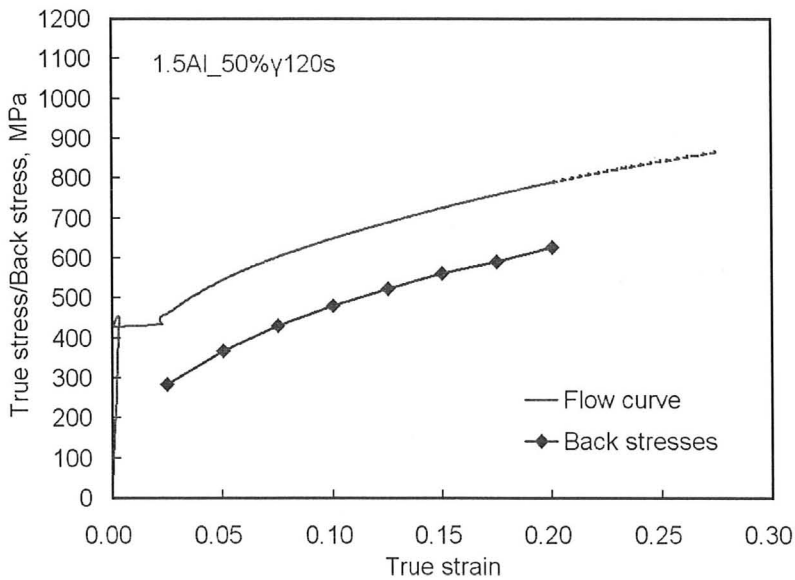


f) 1.5Al_35%γ120s

Figure 5.14 (cont'd) Kinematic hardening (back stresses) vs. flow stresses



g) 1.5Al_50%γ60s



h) 1.5Al_50%γ120s

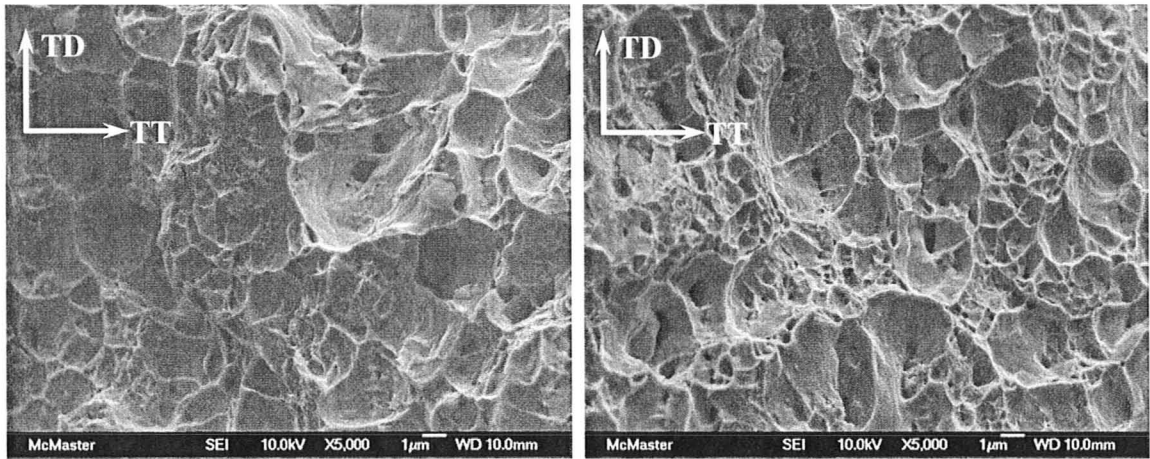
Figure 5.14 (cont'd) Kinematic hardening (back stresses) vs. flow stresses

contribution is desirable in that it helps maintain a relatively high work hardening rate, $d\sigma/d\varepsilon$, during plastic deformation of the TRIP-assisted steels, resulting in the desired combination of high strength and good ductility.

5.3 Fractography

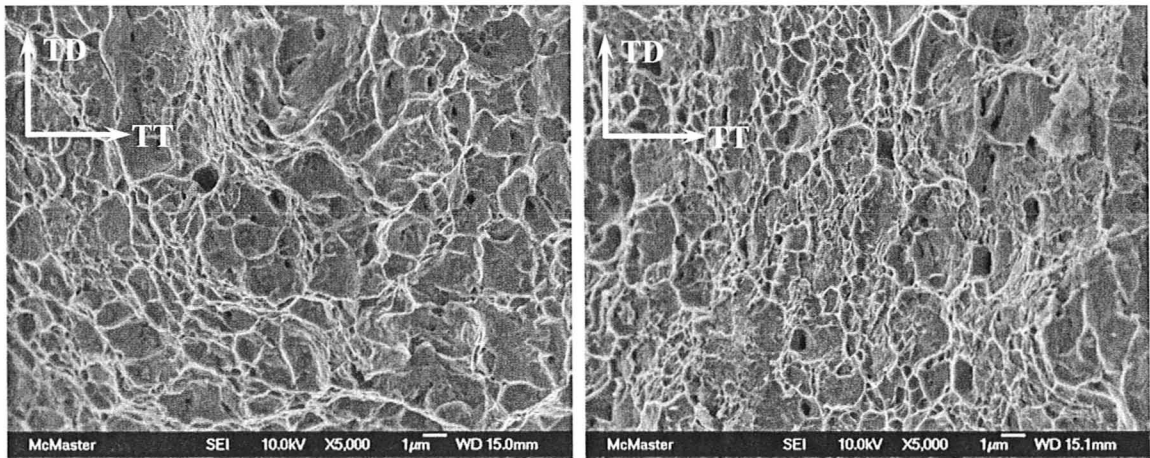
The fracture surface of the tensile samples were examined using SEM. Typical fractographs for all alloys are presented in Figure 5.15. It should be noted that all fractographs presented here were taken at the center of the fracture surface. These fractographs indicate that the dimple surface (ductile fracture) accounted for the majority of the fracture surface. Cleavage and decohesion (Figure 5.15 e)) surfaces were observed to be mixed with the dimple surface. Figure 5.16 presents two enlarged fractographs to show the dimple, cleavage and decohesion surfaces more clearly.

Figure 5.1 has shown that ferrite forms the matrix of the steels. Since ferrite is ductile, it tends to fail as the result of nucleation, growth and coalescence of microscopic voids, which results in dimpled fracture surface. These micro-voids can initiate at inclusions, grain boundaries or second-phase particles due to decohesion, and grow and coalesce along the interface. The decohesion shown in Figure 5.15 e) might be the case of micro-void nucleation, growth and coalescence around inclusions. During plastic



a) 1.0Al_35%γ60s

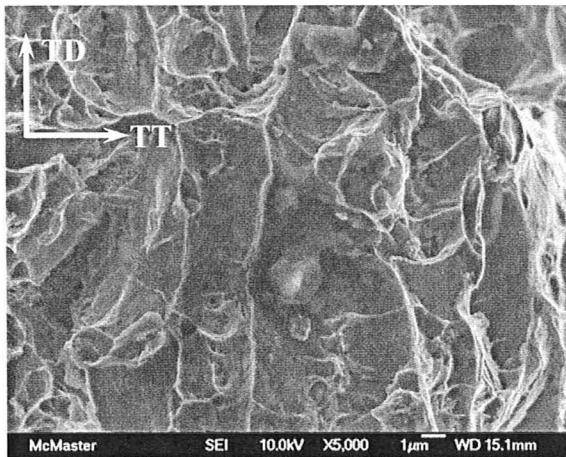
b) 1.0Al_35%γ120s



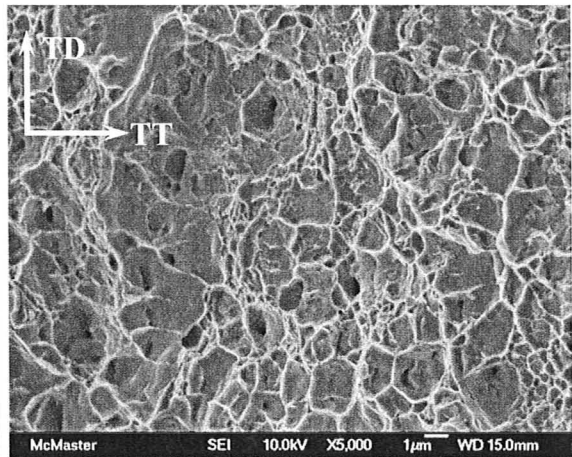
c) 1.0Al_50%γ60s

d) 1.0Al_50%γ120s

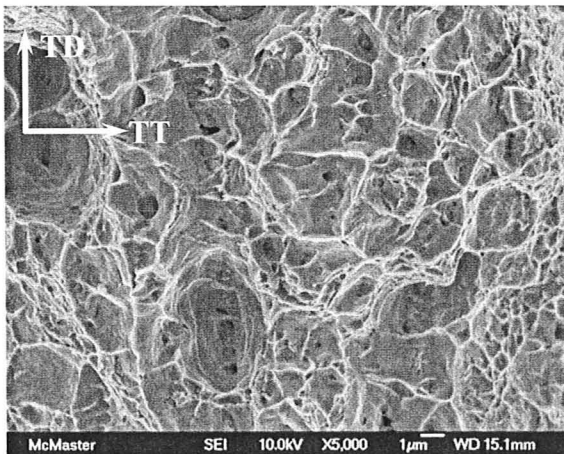
Figure 5.15 SEM micrographs of fracture surfaces
(TD: transverse direction, TT: through thickness)



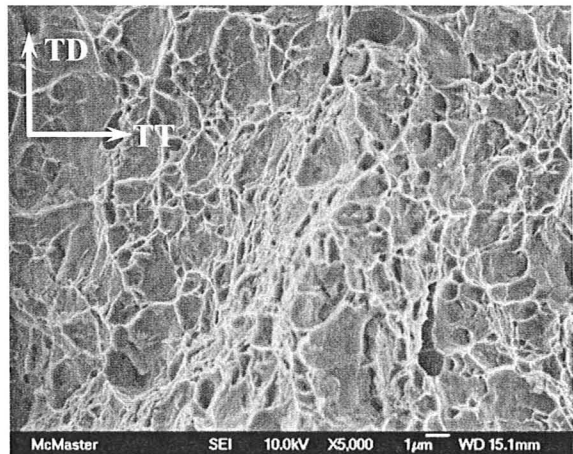
e) 1.5Al_35%γ60s



f) 1.5Al_35%γ120s

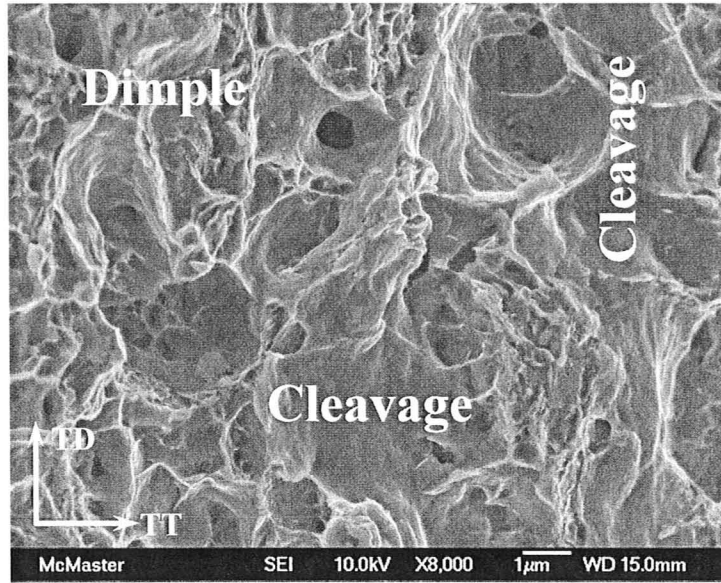


g) 1.5Al_50%γ60s

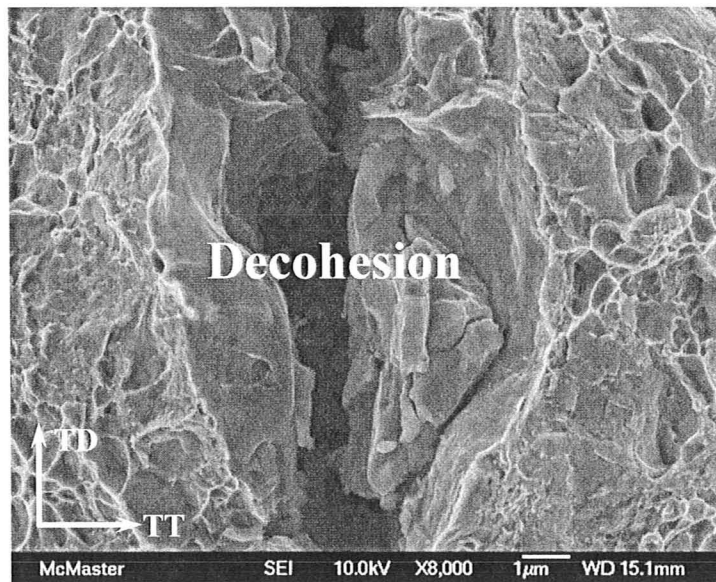


h) 1.5Al_50%γ120s

Figure 5.15 (cont'd) SEM micrographs of fracture surfaces
(TD: transverse direction, TT: through thickness)



a) 1.0Al_50%γ60s



b) 1.5Al_50%γ120s

Figure 5.16 Enlarged fractographs showing the dimple, cleavage and decohesion surfaces (TD: transverse direction, TT: through thickness)

deformation of TRIP-assisted steels, martensite, which is much harder than ferrite, continuously forms. Ferrite and martensite interfaces are often favoured sites for damage nucleation, as well as the growth and coalescence of voids [Jacques et al. (2001d), Lacroix et al. (2008)]. The decohesion shown in Figure 5.16 b) is an example of such a case. In addition to martensitic particles, retained austenite particles that did not transform to martensite at high strains can also be sites for damage nucleation, micro-void growth and coalescence. An example is given in Figure 5.17. The proportion of second phases controls the number of sites for damage nucleation, and is thus the main parameter dictating the fracture behaviour of the steels [Jacques et al. (2001d), Lacroix et al. (2008)].

The brittle martensite grains tended to fail by cleavage due to the strong stress/strain concentration resulting from incompatible deformation between the ductile ferrite matrix and the non-ductile martensite phase. Figure 5.16 a) shows that cracking of martensite grains occurred preferentially in a direction perpendicular to the loading direction [Jacques et al. (2001d)].

In the case of the 1.0Al steels, Figure 5.18 shows that cracks were easier to propagate along microstructural bands. This indicates that the banded structure is detrimental to the cracking resistance of alloys.

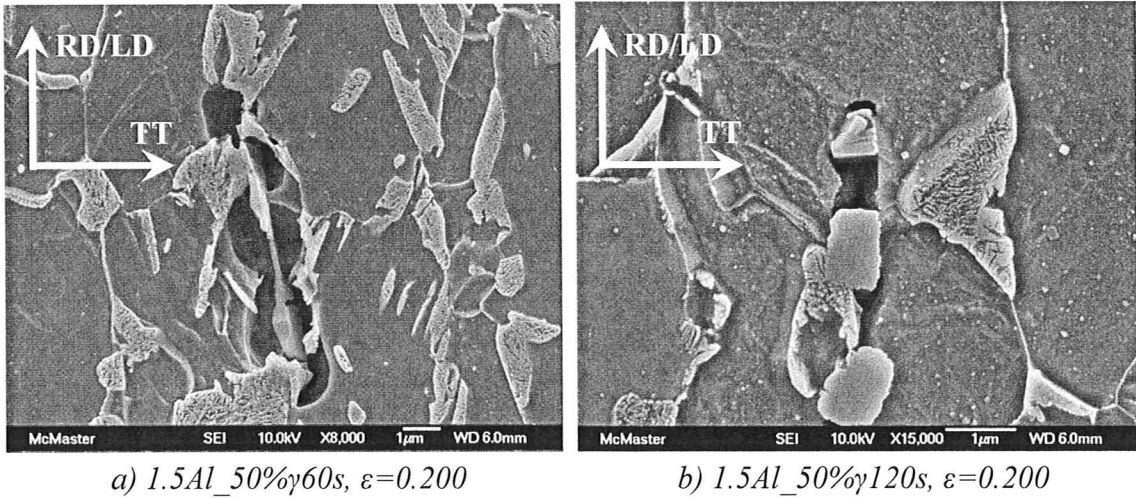


Figure 5.17 Decohesion at retained austenite particles
(RD: rolling direction, LD: loading direction, TT: through thickness)

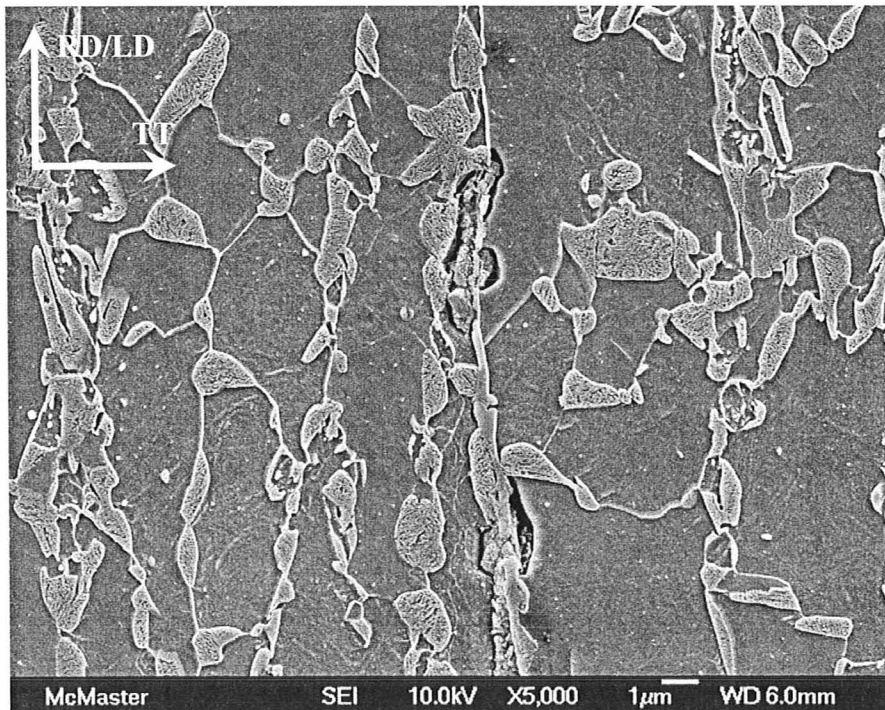


Figure 5.18 Cracking at a band region (1.0Al_35%γ60s, $\epsilon=0.200$)
(RD: rolling direction, LD: loading direction, TT: through thickness)

CHAPTER 6: DISCUSSION

Although the effects of heat treatment parameters and steel chemistry (i.e. the relative Si and Al contents) on the microstructure and mechanical properties of the steels investigated in the present work have been previously discussed by Bellhouse and McDermid (2007), a further discussion is given here. The current discussion will focus on the effects of heat treatment parameters and Al additions on the kinetics of phase transformations taking place during thermal processing (i.e. intercritical annealing and isothermal bainitic transformation) and during plastic deformation (i.e. strain-induced transformations of retained austenite to martensite). These phase transformations dictate the work hardening behaviour of the steels, which will be discussed by examining the evolution of incremental strain hardening coefficients and contribution of kinematic hardening (the development of back stresses). Finally, the enhanced work hardening behaviour of the TRIP-assisted steels is interpreted in that the decrease of work hardening rates, $d\sigma/d\varepsilon$, is attenuated due to the contribution of the TRIP effect. This process gives rise to the sustained work hardening behaviour of the TRIP-assisted steels with superior combination of high strength and good ductility achieved.

6.1 Effects of Heat Treatment Parameters and Steel Chemistry on Phase Transformation Kinetics

The kinetics of phase transformations taking place during thermal processing and plastic deformation will be discussed separately in two sub-sections.

6.1.1 Effects on Phase Transformation Kinetics during Thermal Processing

According to the Fe-C phase diagram, a higher intercritical annealing temperature produces a larger amount of equilibrium intercritical austenite containing a lower carbon content, which should lead to weaker carbon enrichment of the final retained austenite. Based on this interpretation, Jacques et al. (1998) suggested that annealing at a lower temperature would be preferable. However, this is not what was observed in the present work. The reason is that significant ferrite formation occurred during quenching from the intercritical annealing to isothermal bainitic transformation temperatures and also possibly at the beginning of the isothermal bainitic transformation stage. Figure 5.2 showed that a larger amount of intercritical austenite transformed to ferrite in the case of a higher intercritical annealing temperature, and the ultimate fraction of retained austenite was not significantly affected. Furthermore, the retained austenite carbon

content was not significantly affected by the intercritical annealing temperature (Table 5.1).

To show the effect of the intercritical annealing temperature more clearly, the data in Figure 5.2 was re-plotted in Figure 6.1. It clearly shows that the difference between the lower and higher intercritical annealing temperatures was just the amount of ferrite formation. This result was also reported by Sakuma et al. (1991). The results of the present work indicate that one-third to one-half (in case of 35vol.% equilibrium intercritical austenite) or more than one-half (in case of 50vol.% equilibrium intercritical austenite) of the intercritical austenite transformed to ferrite. It is also noteworthy that these results are comparable with those reported by Suh et al. (2007). In the work of Suh et al. (2007), a TRIP-assisted steel of 0.15C-1.47Mn-0.3Si-0.98Al (wt.%), which is close to the composition of the 1.0Al steel in the present research, was studied. It was shown that when the steel was intercritically annealed at 830°C for 120s, producing an equilibrium intercritical microstructure of about 55% ferrite + 45% austenite, followed by cooling at 20°C/s to the isothermal bainitic transformation temperature of 450°C, where the hold time was 120s, nearly 50% of the intercritical austenite was observed to transform back to ferrite. It should be noted that these heat treatment parameters are very similar to those in the present work, indicating that the results can be directly compared to those presented here. It is implied that the cooling rate of 20 °C/s was not sufficient to

avoid the transformation from intercritical austenite to ferrite in the present case. The dilatometric experiments of Soliman and Palkowski (2008) indicated a cooling rate of 50 °C/s suppressed the ferrite formation in case of 0.278C-0.48Mn-0.852Si-0.228Al-0.401 Mo (wt.%) and 0.254C-1.37Mn-0.869Si-0.643Al-0.383Mo steels.

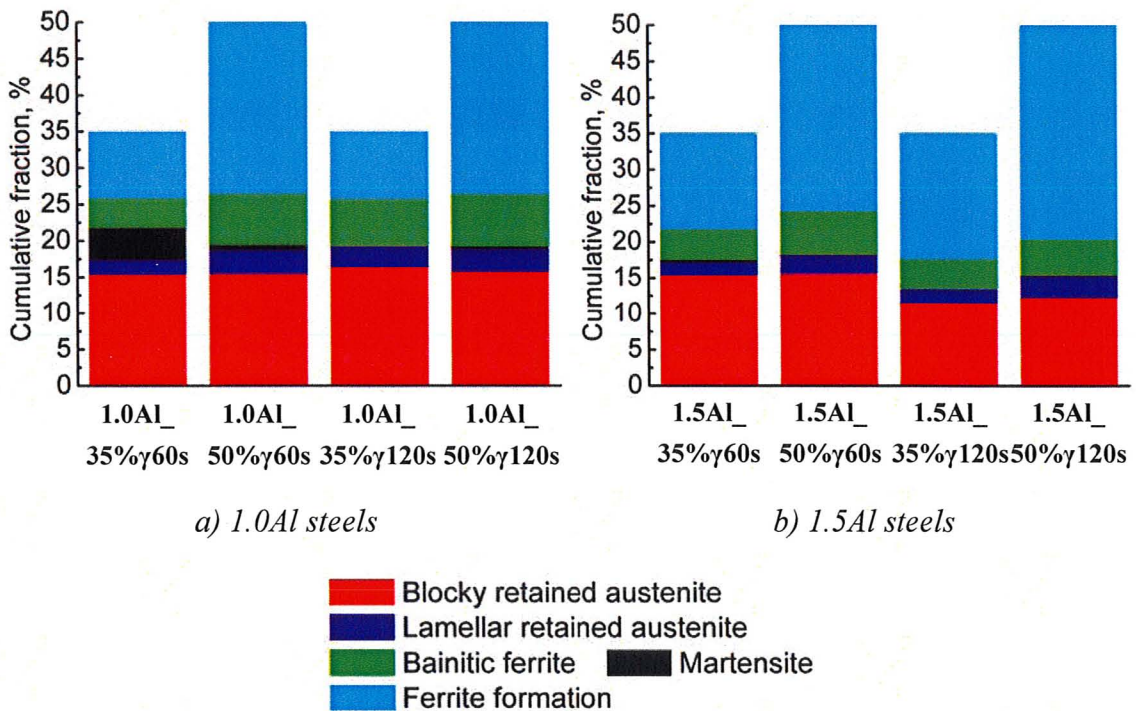


Figure 6.1 Phase constituents of the as-annealed steels excluding intercritical ferrite showing the effect of intercritical annealing temperatures

The fact that the final retained austenite carbon content was not significantly affected by the intercritical annealing temperature (Table 5.1) implies that the remaining austenite was enriched with carbon during ferrite formation. This process has a similar

effect to the carbon enrichment occurring during the isothermal bainitic transformation.

Nevertheless, the carbon enrichment during the ferrite formation could affect the subsequent bainitic transformation kinetics. With the same amount of the equilibrium intercritical austenite, more ferrite formation causes further carbon enrichment of the remaining austenite, and consequently the driving force for the subsequent bainitic transformation will be reduced.

Comparing the 1.0Al and 1.5Al steels of the same heat treatment conditions indicates that more ferrite formation occurred in the 1.5Al steels (Figure 5.2). This is in agreement with the results reported in the literature, i.e. Al additions encouraged the formation of “new” ferrite [Garcia-Gonzalez (2005), Suh et al. (2007)]. It implies that, under the same thermal processing conditions, the austenite before the start of bainitic transformation in the 1.5Al steels experiences more carbon enrichment than that in the 1.0Al steels. The different extents of carbon enrichment in the remaining austenite could lead to different transformation kinetics in the 1.0Al and 1.5Al steels during the isothermal bainitic transformation stage.

In Figure 6.1, it can be seen that the bainitic transformation hold times, i.e. 60 s and 120 s, did not have a significant effect on the volume fraction of retained austenite in the 1.0Al steels, but the effect was noticeable in the 1.5Al steels. The longer bainitic transformation hold time (120 s) gave rise to a lower volume fraction of retained

austenite in the 1.5Al steels in case of the same intercritical annealing temperature. This result seems contrary to the result reported in the literature that Al additions result in faster bainitic transformation kinetics [Mertens et al. (2003), Jacques et al. (2001a)]. If the bainitic transformation in the 1.5Al steels were more rapid, the remaining austenite acquired carbon more quickly, and consequently the bainitic transformation should have stopped earlier. Mahieu et al. (2002a) also argued that a shorter bainitic transformation hold time was required for a higher Al alloyed TRIP-assisted steel compared with a lower Al steel.

In the present work, the bainitic transformation kinetics seems slower in the 1.5Al steels than in the 1.0Al steels. This is possibly associated with the ferrite formation occurring subsequently to the intercritical annealing. It has been pointed out that the 1.5Al steels exhibited more transformation of intercritical austenite to ferrite. This process could lead to more carbon enrichment in the austenite of the 1.5Al steels before the start of bainitic transformation. Thus, the bainitic transformation kinetics of the 1.5Al steels can be reduced. In the work of Jacques et al. (2001a), all equilibrium intercritical austenite transformed to bainite, retained austenite and/or martensite. Mahieu et al. (2002a) did not report ferrite formation either. This is likely because they used very high cooling rates when quenching from the intercritical annealing to isothermal bainite transformation temperatures. The cooling rates of Jacques et al. (2001a) and Mahieu et al.

(2002a) were 70 °C/s and 50 °C/s, respectively. As discussed previously, it is possible to avoid ferrite formation when high cooling rates are used [Soliman and Palkowski (2008), Brandt (1997)]. Mertens et al. (2003) also reported the faster bainite transformation kinetics in high Al steels, but the cooling rate was not reported.

Table 5.1 also indicates that the bainitic transformation hold time had very little effect on the retained austenite carbon content for a given alloy. However the formation of martensite was clearly influenced by the bainitic transformation hold time. The longer hold time, 120s, gave rise to less martensite because the remaining austenite was more highly enriched with carbon before quenching to room temperature. This effect was particularly significant for the 1.0Al_35% γ 120s steel compared with the 1.0Al_35% γ 60s steel. The large amount of banded martensite phase in the 1.0Al_35% γ 60s steel was clearly observed in its microstructure (Figure 5.1 a)). Note that both the 1.5Al_50% γ 60s and 1.5Al_50% γ 120s steels contained a small fraction of martensite. Generally speaking, a longer bainitic transformation hold time is still desirable since it produces less martensite, although the retained austenite carbon content is not significantly increased.

6.1.2 Effects on Phase Transformation Kinetics during Plastic Deformation

In §5.2.2, it was mentioned that the experimental data of the strain-induced transformations (Figures 5.11, 5.12 and 5.13) was fitted using the model of Olson and

Cohen (1975). This model, expressed in equation (6.1), describes the kinetics of strain-induced transformation from austenite to martensite. According to Olson and Cohen (1975), strain-induced martensite nucleates at the intersections of shear bands within austenite grains. The transformation kinetics are governed by three parameters: n , α and β (see equation 6.1). α describes the rate of shear-band formation and is a function of the stacking fault energy (SFE) of austenite, the strain rate and the temperature. The parameter α decreases with the increasing SFE, and the SFE is a function of the austenite composition and temperature. The β parameter is proportional to the probability that a shear-band intersection will generate a martensite embryo, and this probability is temperature dependent through its relationship to the chemical driving force for the transformation from austenite to martensite, $\Delta G^{\gamma \rightarrow \alpha'}$. Smaller α and β parameters reduce the kinetics of strain-induced transformation. The extent to which the transformation becomes saturated at a given temperature is influenced by β only. A higher value of the β parameter leads to a higher saturation [Krizan and De Cooman (2008)]. In equation 6.1, n represents a coefficient related to the orientation of shear bands and is slightly temperature dependent, increasing with the increase of temperature. Olson and Cohen (1975) showed that n equals 2 in case of a random orientation of shear bands.

$$\begin{aligned}
 f_{RA} &= ce^{-\beta(1-e^{-\alpha\epsilon})^n} \\
 f_M &= d - ce^{-\beta(1-e^{-\alpha\epsilon})^n}
 \end{aligned}
 \tag{6.1}$$

f_{RA} is the volume fraction of retained austenite, f_M is the volume fraction of martensite and ε is the plastic strain.

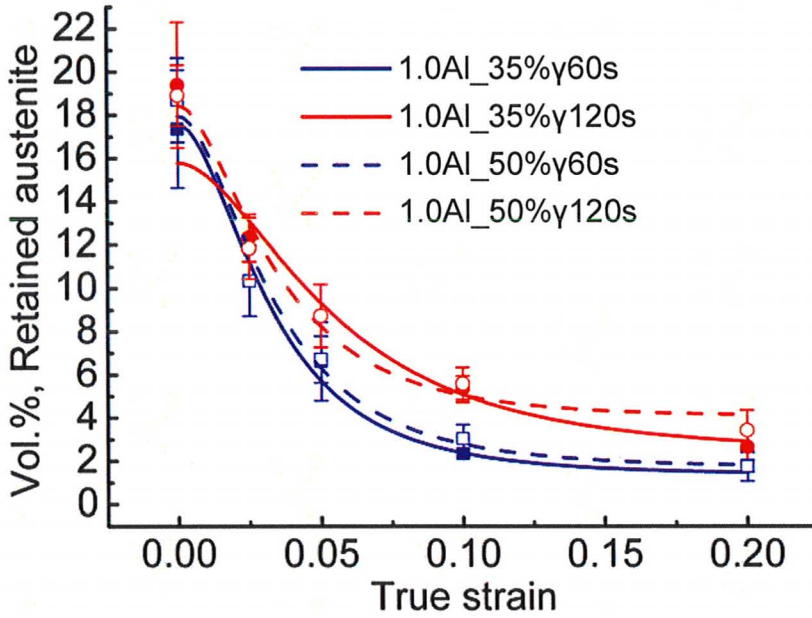
To apply the model to the present work, two additional constants were introduced, which are c and d (see equation 6.1), as the initial fraction of retained austenite was not 1. In the present case, the parameter c depends on the fraction of retained austenite in a given steel. The parameter d is assumed to be the sum of the volume fractions of retained austenite and martensite. During plastic deformation, the decrease of retained austenite is assumed to be equal to the increase of martensite. Thus, the sum of retained austenite and martensite remains constant. The values of c and d will not affect the kinetics of strain-induced transformation for a given steel. Samek et al. (2006) showed that the value of n was close to 2 in the case of TRIP-assisted steels. This value was used in the present work, and also has been used elsewhere [Krizan and De Cooman (2008), De Cooman (2004)]. The parameters α and β were obtained through fitting the blocky, lamellar and total retained austenite volume fractions obtained via image analysis for each steel. The values obtained are summarized in Table 6.1. The calculated curves for the total retained austenite and martensite shown in §5.2.2 are compared in Figures 6.2 and 6.3, respectively.

From Table 6.1, it can be seen that both α and β parameters of the lamellar retained austenite were generally smaller than those of the blocky retained austenite for

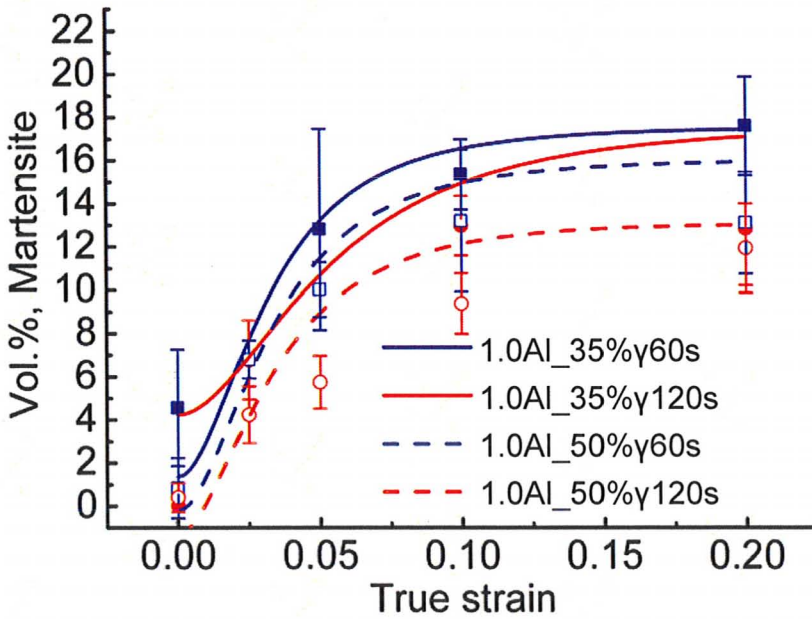
the 1.0Al steels. In the case of the 1.5Al steels, the values of α were similar when comparing the blocky and lamellar retained austenite; the β parameters of the lamellar retained austenite were generally smaller than those of the blocky retained austenite. In both the 1.0Al and 1.5Al steels, the lamellar retained austenite exhibited slower transformation kinetics, as shown in Figure 5.12 and the SEM micrographs of Figures 5.7 b) and 5.8 b). Comparing α and β parameters of the total and blocky retained austenite will show that the fitted values were not significantly influenced by the lamellar

Table 6.1 The fitted values of α and β parameters for the volume fraction of retained austenite (Figure 5.12)

Steel	α			β		
	Total	Blocky	Lamellar	Total	Blocky	Lamellar
1.0Al_35% γ 60s	22	23	13	2.5	2.7	1.8
1.0Al_35% γ 120s	15	16	14	1.9	1.7	1.9
1.0Al_50% γ 60s	22	23	20	2.3	2.6	1.4
1.0Al_50% γ 120s	26	30	15	1.5	1.7	1.1
1.5Al_35% γ 60s	50	42	56	1.4	1.7	0.8
1.5Al_35% γ 120s	6	5	5	2.3	2.7	2.1
1.5Al_50% γ 60s	16	17	5	2.0	2.0	4.0
1.5Al_50% γ 120s	11	9	13	2.0	2.1	1.6

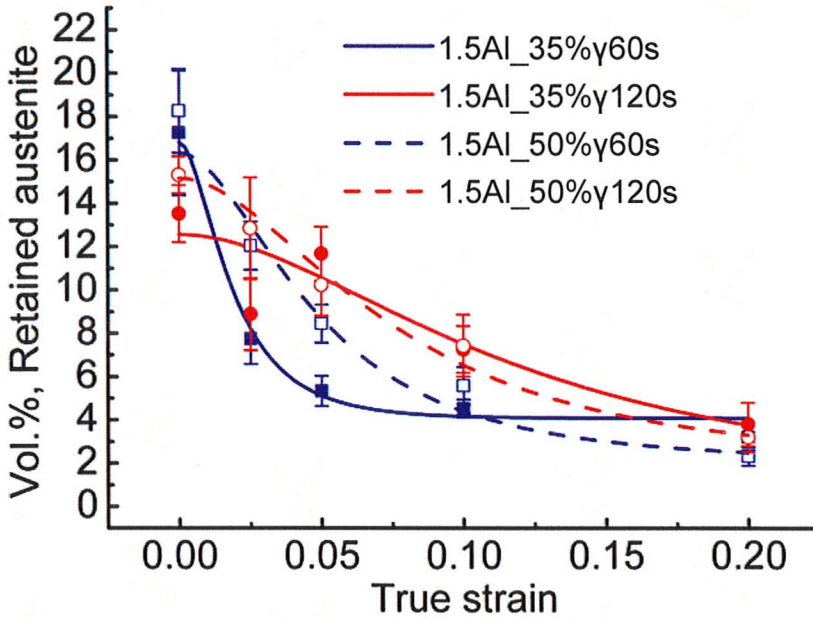


a) Evolution of retained austenite

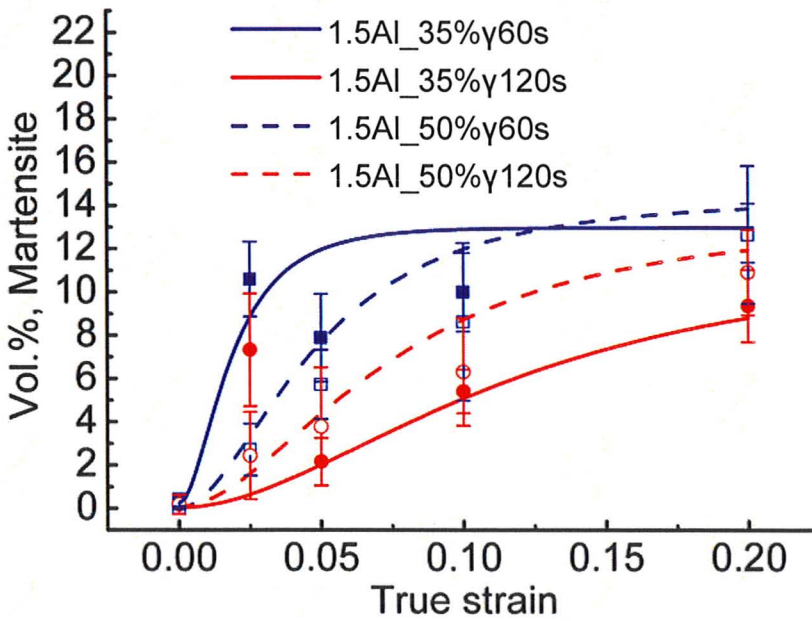


b) Evolution of martensite

Figure 6.2 Strain-induced transformation kinetics of the 1.0Al steels



a) Evolution of retained austenite



b) Evolution of martensite

Figure 6.3 Strain-induced transformation kinetics of the 1.5Al steels

retained austenite since the amount of lamellar retained austenite was limited. This indicates that the transformation kinetics of the total retained austenite were mainly determined by the blocky retained austenite, which was the primary contributor to the TRIP effect.

Figure 6.2 shows that the intercritical annealing temperature did not significantly affect the strain-induced transformation kinetics for the 1.0Al steels. It seems that the bainitic transformation hold time had a slight effect. This is probably due to greater carbon enrichment in the case of the longer bainitic transformation hold time, although this effect was not very evident from the X-ray data in Table 5.1. This was a similar case for the 1.5Al steels when looking at the effects of the intercritical annealing temperature and bainitic transformation hold time on the transformation kinetics in Figure 6.3. It is noteworthy that the transformation kinetics of the 1.5Al steels were more sensitive to thermal processing parameters than those of the 1.0Al steels. This might be associated with the positive effect of Al additions on ferrite formation occurring subsequent to intercritical annealing. The encouragement of ferrite formation could influence the 1.5Al steels at least in two ways. First, the final retained austenite fraction was reduced (Figure 6.1). Second, the isothermal bainitic transformation kinetics could be affected due to the carbon enrichment of the remaining austenite as a result of ferrite formation.

Compared to the 1.0Al steels, the 1.5Al steels, except for the 1.5Al_35% γ 60s

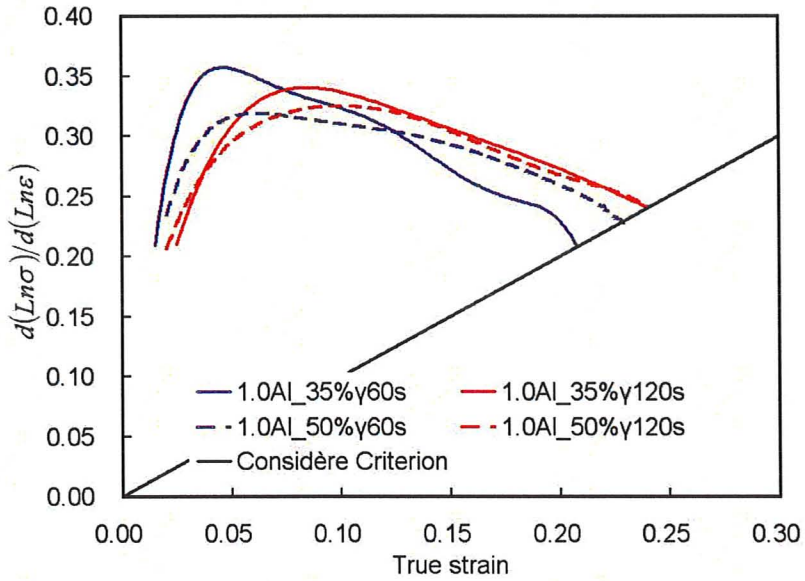
steel, exhibited relatively slower strained-induced transformation kinetics (Figures 6.2 and 6.3), which means higher stability of the retained austenite in the 1.5Al steels. This is due to the higher Al content in the 1.5Al steels, which increased the stacking fault energy (SFE) of the retained austenite [Samek et al. (2006), De Cooman (2004)]. This is shown by the smaller α parameter of the 1.5Al steels compared to that of the 1.0Al steels in Table 6.1. The 1.5Al_35% γ 60s steel seems very singular with rapid initial transformation kinetics and low ultimate saturation, i.e. high α and small β parameters in Table 6.1. This could be due to experimental bias during image analysis because the transformation kinetics indicated by the X-ray diffraction data (Figure 5.11 e)) were different.

6.2 Link to Mechanical Properties

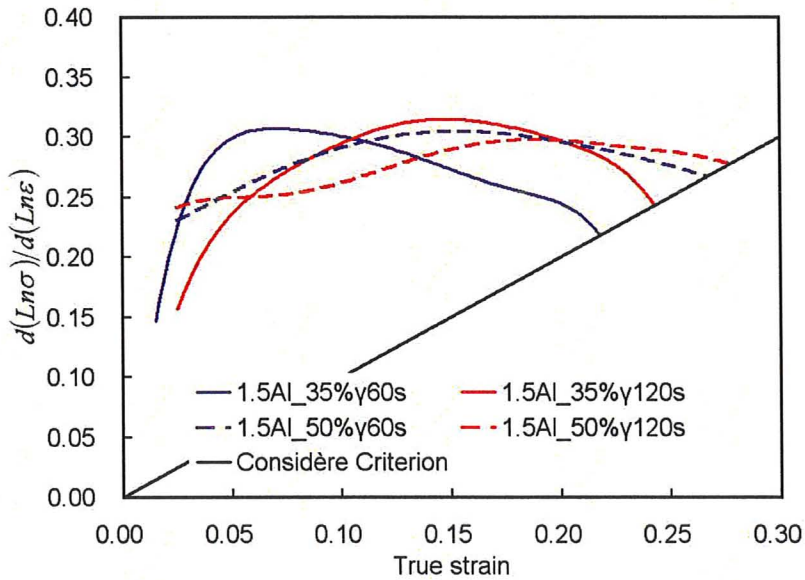
The transformation kinetics during thermal processing affected the final microstructure of the steels. This effect, together with the transformation kinetics during plastic deformation, directly influenced the work hardening behaviour of the steels. This section will show how the results discussed in §6.1 are linked to the work hardening behaviour of the experimental alloys in terms of the incremental strain hardening coefficient and kinematic hardening (the development of back stresses).

6.2.1 Incremental Strain Hardening Coefficient

The incremental strain hardening coefficients of all steels have been previously shown in Figure 5.5 as discrete plots. To facilitate comparison, these data for each alloy are re-plotted in Figure 6.4 a) and b) for the 1.0Al and 1.5Al steels, respectively. It is clear that the incremental strain hardening coefficient of the TRIP-assisted steel is not a constant, which is assumed in the Holloman equation, $\sigma = K\epsilon^n$. The n_{incr} of the 1.0Al steels (Figure 6.4 a)) evolved in a very similar way except for the 1.0Al_35% γ 60s steel, in which n_{incr} reached a peak value rapidly and also decreased rapidly after that, leading to a smaller uniform elongation of the steel. Recalling the lower yield stress (Table 5.3) and shorter yield elongation (Figure 5.3 a)) of the steel, it becomes clear that the work hardening of the 1.0Al_35% γ 60s steel is more like that of dual phase steels. Indeed, the microstructure shown in Figure 5.1 a) and the image analysis result shown in Figure 6.1 indicate a large amount of thermal martensite present in this steel. As a comparable case of dual phase steels, residual stresses, mobile dislocations in the ferrite matrix and strong internal stresses at the initial stage of plastic deformation, which are all due to the formation of thermal martensite, reduced the yield stress and discontinuous yielding behaviour and gave rise to significant initial work hardening of the 1.0Al_35% γ 60s steel [Matlock et al. (1979), Cribb and Rigsbee (1979), Gerbase et al. (1979), Speich and



a) 1.0Al steels



b) 1.5Al steels

Figure 6.4 Comparison of incremental strain hardening coefficients

Miller (1979)]. On the other hand, the large amount of martensite and strong internal stresses made the steel less ductile because more damage nucleation sites existed and decohesion between ferrite and martensite became easier (Figure 5.18). All these factors made the 1.0Al_35% γ 60s steel less resistant to the onset of tensile instability, resulting in a smaller uniform elongation.

Figure 6.1 b) indicated that all 1.5Al steels contained no significant thermal martensite, but their incremental strain hardening coefficients evolved in different ways from one another (Figure 6.4 b)). For the 1.5Al_50% γ 60s and 1.5Al_50% γ 120s steels, the incremental strain hardening coefficients evolved very smoothly and the larger uniform elongations were obtained, which is associated with their slower strain-induced transformation kinetics (Figure 6.3). The reverse was true for the 1.5Al_35% γ 60s steel. Faster strain-induced transformation kinetics led to a higher initial n_{incr} and lower uniform elongation. By contrast, the 1.5Al_35% γ 120s steel exhibited very flat retained austenite to martensite transformation kinetics (Figure 6.3), but the evolution of n_{incr} was not very smooth and the uniform elongation was not high. This was possibly due to its relatively low amount of retained austenite (Figure 6.1).

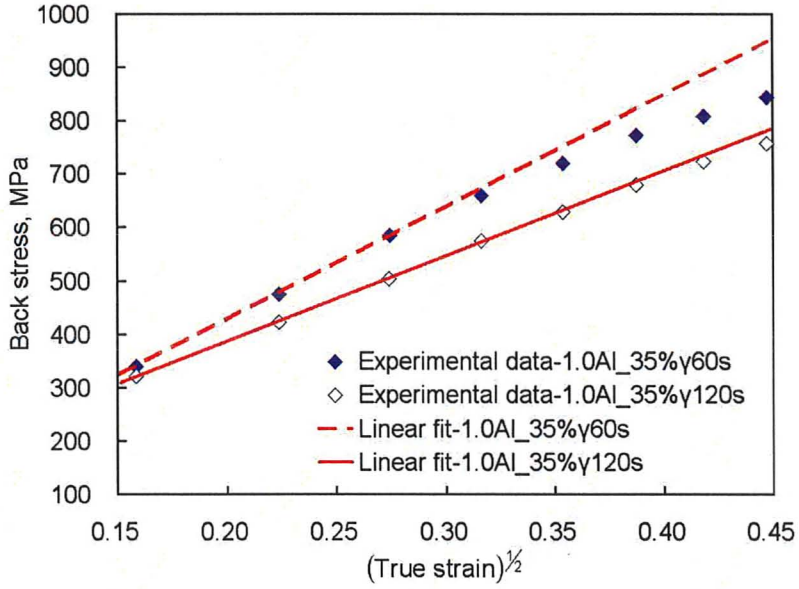
Generally, the incremental strain hardening coefficients of the 1.5Al steels (Figure 6.4 b)) evolved more smoothly than those of the 1.0Al steels (Figure 6.4 a)) and relatively larger uniform elongations were obtained. This is the result of the relatively

slower strain-induced transformation kinetics of the 1.5Al steels (Figure 6.3).

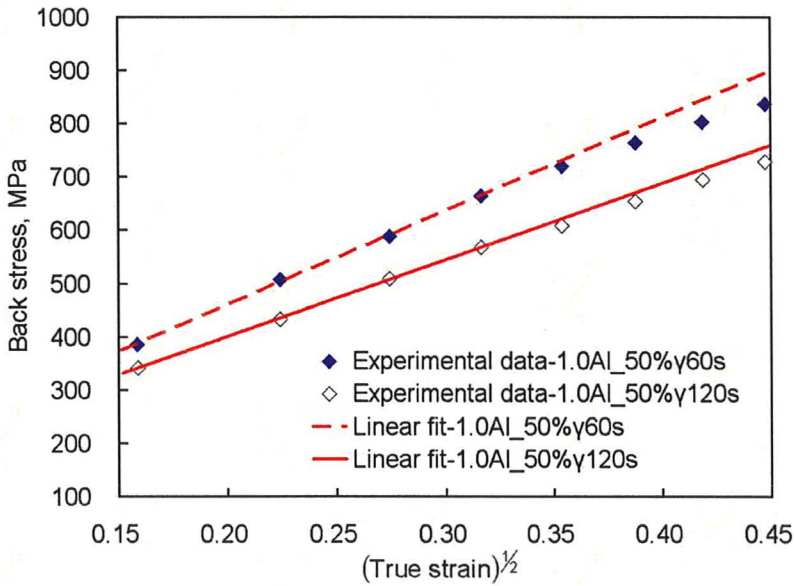
Based on the above analysis, it can be seen that, under the condition of no significant thermal martensite present in the as-annealed steel, the strain-induced transformation kinetics directly influenced the work hardening behaviour of the TRIP-assisted steel. Slower transformation kinetics, which mean higher stability of retained austenite, give a smoother evolution of work hardening and more efficiently delay the onset of tensile instability per the Considère criterion.

6.2.2 Kinematic Hardening

The evolution of back stresses for all steels have been previously shown in Figure 5.14. These results will be analyzed below following the Brown and Stobbs' model [Brown and Stobbs (1971b)]. A detailed explanation of the model (equation 2.2) was given in §2.3.1. As already mentioned, back stresses increase linearly with the square root of plastic strain according to this model. Following this model, the back stress data in Figure 5.14 were re-plotted against the square root of strain, as shown in Figure 6.5, where each graph compares a pair of steels that have the same composition and processing conditions with varying bainitic transformation hold times. From Figure 6.5, it can be seen that, for the 1.5Al_35% γ 120s, 1.5Al_50% γ 60s and 1.5Al_50% γ 120s steels, a linear relationship existed between the back stress and the square root of strain

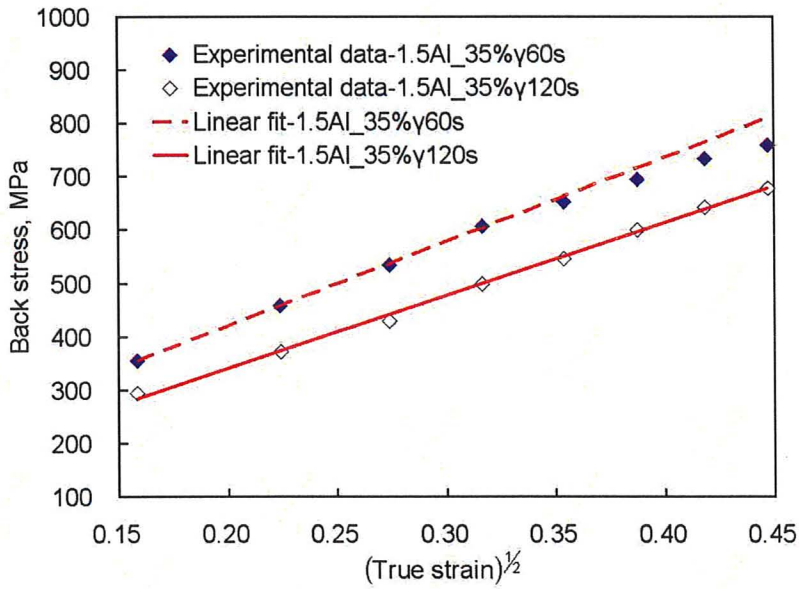


a) 1.0Al_35% γ 60s and 1.0Al_35% γ 120s

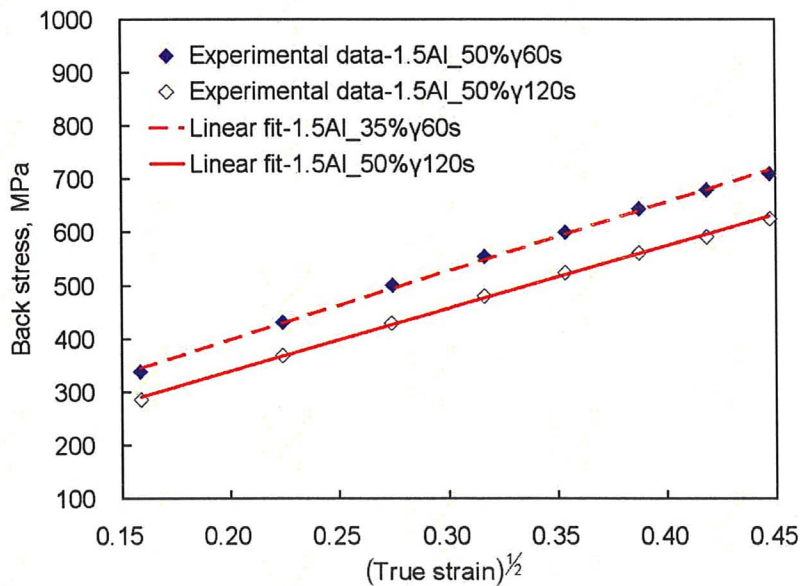


b) 1.0Al_50% γ 60s and 1.0Al_50% γ 120s

Figure 6.5 Evolution of back stresses vs. square root of true strain



c) 1.5Al_{35%}γ_{60s} and 1.5Al_{35%}γ_{120s}



d) 1.5Al_{50%}γ_{60s} and 1.5Al_{50%}γ_{120s}

Figure 6.5 (cont'd) Evolution of back stresses vs. square root of true strain

within experimental strain levels. This was not the case for the 1.0Al and 1.5Al_{35% γ} 60s steels, where the back stress deviated from linearity at different strain levels. In particular, the back stress in the 1.0Al_{35% γ} 60s steel (Figure 6.5 a)) significantly deviated from linearity after strains of approximately 0.10. For clarification, the strains at which the back stress deviated from the $\epsilon^{1/2}$ relationship are summarized in Table 6.2, where a steel is marked with “N/A” when no deviation was observed.

Table 6.2 Strains at which the back stress deviated from $\epsilon^{1/2}$ linearity

Steel	Deviation strain	Steel	Deviation strain
1.0Al _{35%γ} 60s	0.100	1.0Al _{50%γ} 60s	0.125
1.0Al _{35%γ} 120s	0.175	1.0Al _{50%γ} 120s	0.150
1.5Al _{35%γ} 60s	0.125	1.5Al _{50%γ} 60s	N/A
1.5Al _{35%γ} 120s	N/A	1.5Al _{50%γ} 120s	N/A

Note: “N/A” means the back stresses in this steel maintained the $\epsilon^{1/2}$ linearity within experimental strain levels.

An important feature of the Brown and Stobbs’ model [Brown and Stobbs (1971b)] is that strong plastic relaxation occurs at large plastic strains, leading to the saturation of back stresses, after which the model breaks down. In the original work of Brown and Stobbs (1971b), the model was only valid for plastic strains less than 0.08. In

alloys strengthened through the use of hard precipitates or particles, plastic relaxation can occur through dislocation annihilation or by the deformation of hard particles [Lloyd (1977)].

The deviation of the back stresses from $\epsilon^{1/2}$ linearity observed in the 1.0Al and 1.5Al_35% γ 60s steels indicates that the back stresses in these steels were becoming saturated and their contribution to the overall work hardening of the steels was being reduced. No deviation from $\epsilon^{1/2}$ linearity observed in the 1.5Al steels (except for the 1.5Al_35% γ 60s steel) implies that the back stresses in these steels did not saturate and the contribution of kinematic hardening was not reduced. For the TRIP-assisted steels studied in the present work, plastic relaxation which would lead to the back stress saturation was mainly due to the fracture or decohesion of hard martensite particles from the ferrite matrix [Gerbase et al. (1979)]. It should be noted that the back stress saturation observed in the present work was not as significant as that shown by Gerbase et al. (1979), and the deviation strains shown in Table 6.2 (no deviation observed in three 1.5Al steels) were much larger than the saturation strain of 0.01 reported by Gerbase et al. (1979) for a dual phase steel. This implies that the development of back stresses in TRIP-assisted steels is different from that in dual phase steels. Thus, further examination of this phenomenon in TRIP-assisted steels is necessary.

In the Brown and Stobbs' model (equation 2.2), the volume fraction of hard

particles is constant throughout the applied strain for a particular material. However, the amount of the hard phase, martensite, in TRIP-assisted steels is (ideally) gradually increasing during plastic deformation. This feature makes TRIP-assisted steels different from dual phase steels and makes it necessary to reconsider the Brown and Stobbs' model. The evolution of martensite in the 1.0Al and 1.5Al steels can be seen in Figures 6.2 and 6.3. In the particular case of TRIP-assisted steels, one possible mechanism that could take place was that plastic relaxation mechanisms could have indeed become operative for existing martensite particles at a certain strain, but as new martensite particles were constantly being produced by the retained austenite to martensite transformation, the newly transformed martensite would supply an additional site for dislocation pile-ups and lead to the observed continuous increase of back stresses. This means that a gradual retained austenite to martensite transformation could counterbalance the back stress saturation resulting from plastic relaxation, with the net result of delaying back stress saturation, as observed in the 1.5Al_35% γ 120s, 1.5Al_50% γ 60s and 1.5Al_50% γ 120s steels (Figure 6.5).

In this sense, the rate at which retained austenite transforms to martensite is essential to increase the level of kinematic hardening and maintain the work hardening rate at high values, thereby delaying the onset of tensile instability and resulting in a favorable strength-ductility balance. However, once no new martensite was formed,

plastic relaxation mechanisms began to dominate and the back stress saturation occurred. This would appear to be the case for the observed results of the 1.0Al and 1.5Al_{35% γ 60s} steels. As an example, Figure 6.2 b) shows that martensite in the 1.0Al_{35% γ 60s} steel increased quickly at the early stages of plastic deformation and the rate of new martensite being produced became extremely low after a strain of 0.10, which led to the observed deviation of back stresses from $\epsilon^{1/2}$ linearity (Figure 6.5 a)). Further examination of the martensite evolution for the 1.5Al_{35% γ 120s}, 1.5Al_{50% γ 60s} and 1.5Al_{50% γ 120s} steels (Figure 6.3 b)) indicates that new martensite in these steels was produced continuously until large strains, and accordingly the back stresses in these steels maintained their linear relationship with $\epsilon^{1/2}$ within experimental strain levels (Figure 6.5 c) and d)). It is also clear that the lower the rate of martensite transformation with increasing strain, the further the back stress saturation is delayed. For example, the 1.0Al_{35% γ 120s} steel, compared to the 1.0Al_{35% γ 60s} steel in Figures 6.2 b) and 6.5 a), and the 1.0Al_{50% γ 120s} steel, compared to the 1.0Al_{50% γ 60s} steel in Figures 6.2 b) and 6.5 b), exhibited further delayed appearance of back stress saturation, which well correlates with the later cessation of martensite transformation at a significant rate.

Strain-induced martensite transforms from retained austenite. A lower rate of martensite formation implies a higher stability of the retained austenite. From the above analysis, it can be seen that higher stability of retained austenite, which means slower

strain-induced phase transformation kinetics, encourages the production of back stresses, and in turn improves the contribution of kinematic hardening to the overall hardening of the steels.

Larger back stresses were produced in the 1.0Al_35% γ 60s, 1.0Al_50% γ 60s, 1.5Al_35% γ 60s and 1.5Al_50% γ 60s steels due to more martensite being present in these steels compared to the 1.0Al_35% γ 120s, 1.0Al_50% γ 120s, 1.5Al_35% γ 120s and 1.5Al_50% γ 120s steels (Figure 6.5 a) through d) and Figures 6.2 and 6.3, respectively). This qualitatively agrees with the Brown and Stobbs' model [Brown and Stobbs (1971b)] in that it is predicted that back stresses increase with the volume fraction of hard particles.

6.3 Interpretation of Work Hardening in TRIP-assisted Steels

In §2.4, it was discussed that the modified Swift equation (equation 2.7) was frequently used to analyze the tensile curves of dual phase steels. Using a $\ln(d\sigma/d\varepsilon)$ vs. $\ln\sigma$ plot based on equation 2.7, the dynamic evolution of $d\sigma/d\varepsilon$ can be characterized in terms of the slope of the plot. TRIP-assisted steels contain ferrite, retained austenite, and a minority of martensite in addition to bainitic ferrite. Ferrite is the principal source of plastic deformation; martensite and transforming retained austenite are second phases dynamically altering the work hardening rate of the material.

This is comparable to dual phase steels. The evolving $d\sigma/d\varepsilon$ of the experimental TRIP-assisted steels will be analyzed by plotting $\ln(d\sigma/d\varepsilon)$ against $\ln\sigma$ in this section.

The $\ln(d\sigma/d\varepsilon)$ vs. $\ln\sigma$ plots of the 1.0Al steels are shown in Figure 6.6. It can be seen that the work hardening rate, $d\sigma/d\varepsilon$, of the 1.0Al steels decreased more and more rapidly since the slope of the plots was becoming smaller and smaller. The transition between different deformation stages was not obvious. By contrast, the $\ln(d\sigma/d\varepsilon)$ vs. $\ln\sigma$ plots of the 1.5Al steels (Figure 6.7) took on different characteristics. The 1.5Al steels except for the 1.5Al_35% γ 60s steel exhibited stage transitions during plastic deformation. The transition points are marked with arrows in Figure 6.7. The behaviour of the 1.5Al_35% γ 60s steel (Figure 6.7 a)) was similar to that of the 1.0Al steels, i.e. more and more rapid decrease of the work hardening rate and no obvious stage transitions.

To have a direct understanding, the property parameters at the transition points (i.e. stress, strain, and fractions of transformed and untransformed retained austenite) of the 1.5Al steels are summarized in Table 6.3, where the 1.5Al_35% γ 60s steel is marked with "N/A" indicating no obvious stage transitions.

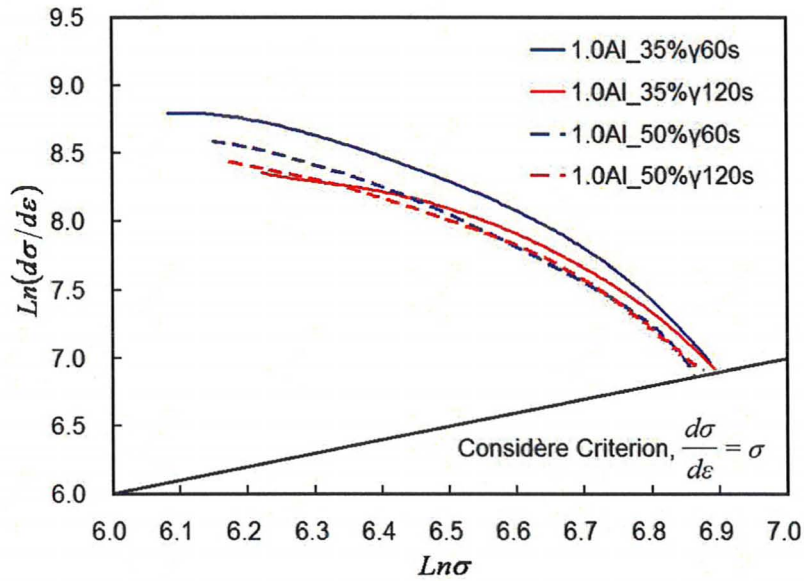


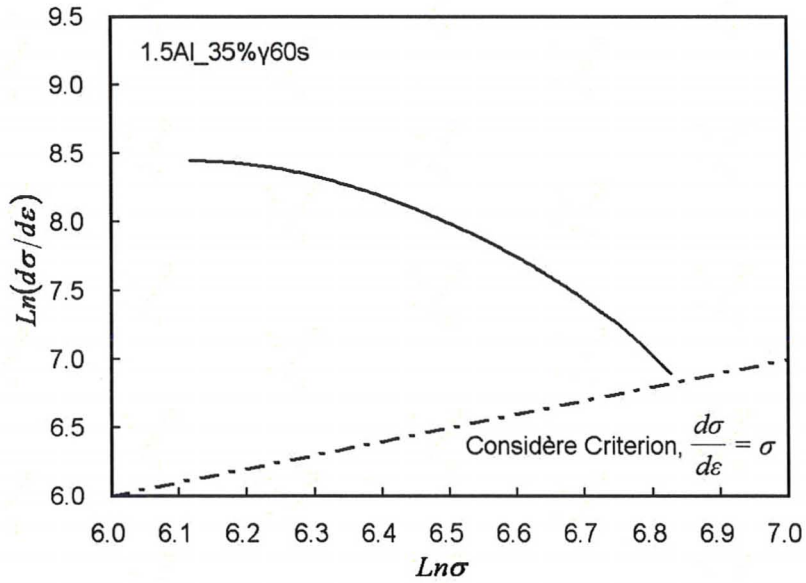
Figure 6.6 $\ln(d\sigma/d\varepsilon)$ vs. $\ln\sigma$ plots of the 1.0Al steels

Table 6.3 Property parameters at the transition points of the 1.5Al steels

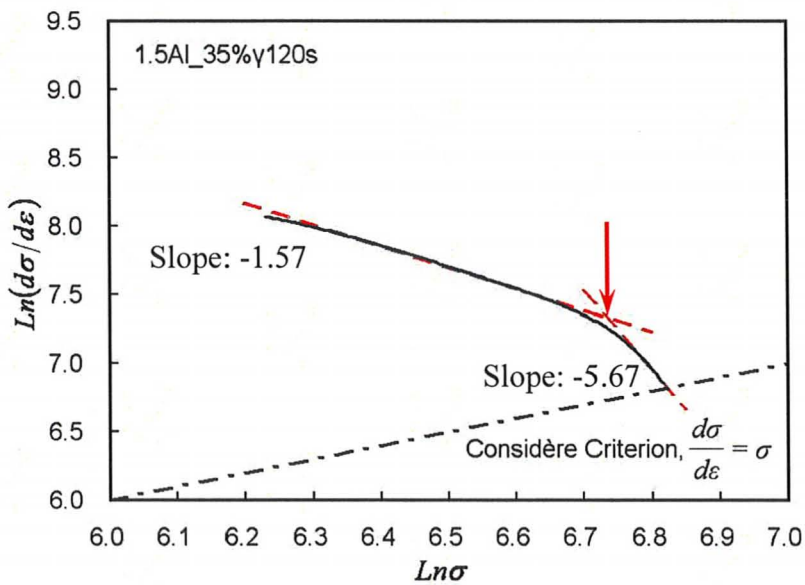
Steel	Strain	Stress (MPa)	Fraction of the Untransformed RA (%)	Fraction of the initial RA (%)	Percentage of the transformed RA (%)
1.5Al_35%γ60s			N/A		
1.5Al_35%γ120s	0.18	841	4.21	12.55	66
1.5Al_50%γ60s	0.17	788	2.71	16.33	83
1.5Al_50%γ120s	0.19	776	3.45	15.15	77

Note: 1) "N/A" indicates that no obvious transitions were observed for the 1.5Al_35%γ60s steel;

2) The volume fraction numbers of retained austenite are taken from Figure 6.3 a).

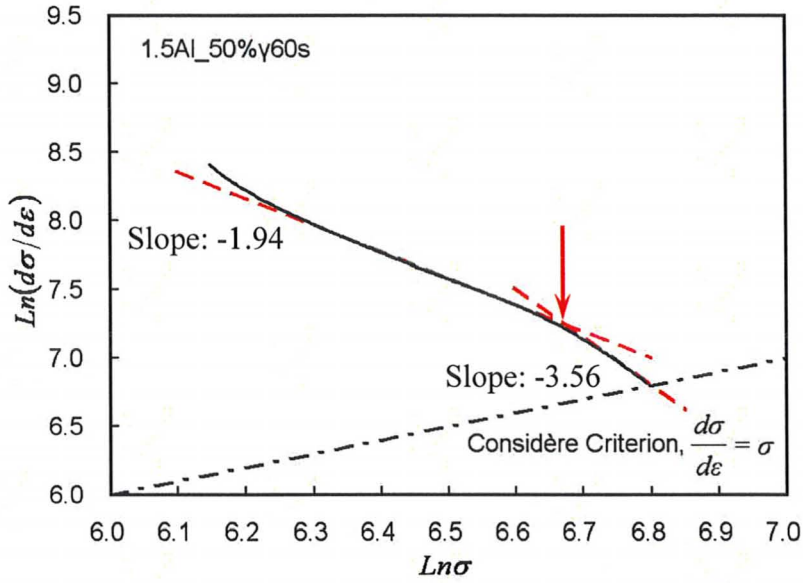


a) 1.5Al_35%γ60s

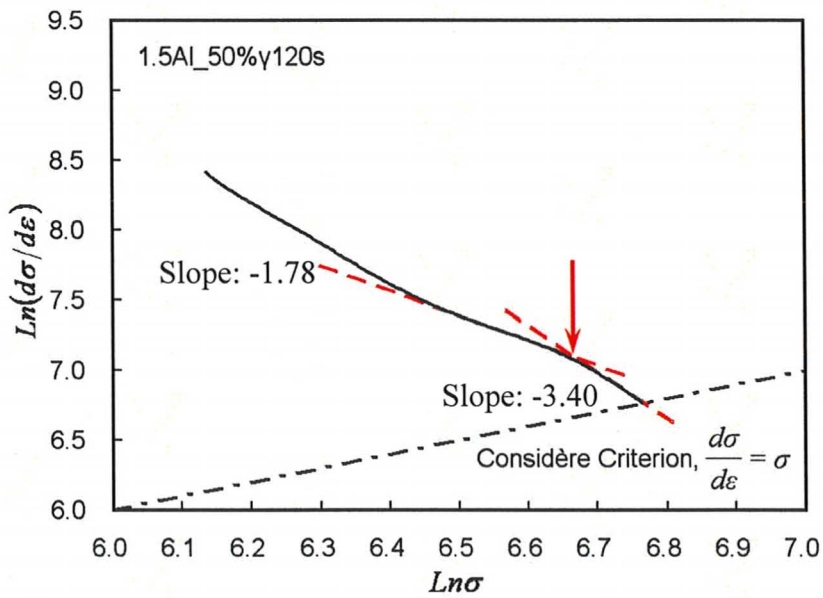


b) 1.5Al_35%γ120s

Figure 6.7 $\ln(d\sigma/d\varepsilon)$ vs. $\ln\sigma$ plots of the 1.5Al steels



c) 1.5Al_50%γ60s



d) 1.5Al_50%γ120s

Figure 6.7 (cont'd) $\text{Ln}(d\sigma/d\varepsilon)$ vs. $\text{Ln}\sigma$ plots of the 1.5Al steels

As shown in Figures 6.2 and 6.3, the retained austenite in the 1.0Al and 1.5Al_35% γ 60s steels exhibited relatively faster strain-induced transformation kinetics. Such low retained austenite stability was not efficient in attenuating the decreasing rate of work hardening rates for these experimental steels, resulting in a more rapid decrease of work hardening rates. The retained austenite in the 1.5Al_35% γ 120s, 1.5Al_50% γ 60s and 1.5Al_50% γ 120s steels transformed to martensite more smoothly, showing relatively slower transformation kinetics (Figure 6.3), and the back stresses in these steels increased with $\epsilon^{1/2}$ up to strains as large as 0.20 (Figure 6.5 c) and d)). This effect efficiently attenuated the decrease of work hardening rates before the transition points marked with the arrows in Figure 6.7. Table 6.3 shows that the deformation transition for the 1.5Al_35% γ 120s steel occurred at the point where 66% of the retained austenite had transformed to martensite. For the 1.5Al_50% γ 60s and 1.5Al_50% γ 120s steels, 83% and 77% of the retained austenite had transformed to martensite at the transition points, respectively. Note that, at the earlier deformation stage, there was an initial section where the work hardening rate of the 1.5Al_50% γ 120s steel decreased more rapidly. This was likely because the rate and amount of martensite production was relatively low, Figure 6.3 b).

The above examination on deformation stages indicates that retained austenite of higher stability exhibiting slower strain-induced transformation kinetics gives rise to

sustained work hardening mechanisms including significant kinematic hardening contributed by parabolically increasing back stresses and then the decrease of work hardening rates is efficiently attenuated. The deformation stage at which the work hardening rate decreases sharply is delayed to higher strains. For example, this stage did not occur until a strain of 0.17 for the 1.5Al_50% γ 60s steel (Table 6.3). It is also indicated that, after about 70~ 80% of the retained austenite had transformed to martensite, the decrease of work hardening rates became sharp for the TRIP-assisted steels. In this deformation stage, decohesion between ferrite and martensite and/or retained austenite that was not transformed contributed the main reason for the fast decrease of work hardening rates. Decohesion between ferrite and retained austenite that was not transformed in the 1.5Al_50% γ 60s and 1.5Al_50% γ 120s steels was shown in Figure 5.17.

6.4 Compatibility with Continuous Galvanizing Process

The above results and the work of Bellhouse and McDermid (2007) showed that the Al and Al/Si alloyed steels processed using the higher isothermal bainitic transformation temperature compatible with the continuous galvanizing process contained significant retained austenite. The present work confirmed that the retained austenite

exhibited a TRIP effect depending on the alloy and thermal processing parameters.

Generally, the 1.5Al steels possessed a better balance between strength and ductility due to a more gradual TRIP effect, which improved the work hardening behaviour of the steels more efficiently.

In particular, the 1.5Al steels intercritically annealed at the higher temperature (50% equilibrium intercritical austenite) had good work hardening behaviour regardless of the bainitic transformation time. Comparing the present results with similar alloys in the literature, which were heat treated using conventional processing routes shown in Table 2.1, shows that the alloys of the present work exhibited better mechanical properties, i.e higher UTS and ϵ_u .

Furthermore, Bellhouse et al. (2007) and Bellhouse and McDermid (2008) showed that the Al alloying element did not damage wettability of the steel surface due to its internal oxidation behaviour. It seems that the processing of Al-alloyed TRIP assisted steels with excellent mechanical properties can be compatible with the continuous galvanizing process.

CHAPTER 7: CONCLUSIONS

In the present research, two galvanizable TRIP-assisted steels with the desired multiphase microstructure were obtained using heat treatment routes compatible with the continuous galvanizing process. Based on the present work and the work of Bellhouse et al. (2007) and Bellhouse and McDermid (2008), it seems that it is possible to process Al-alloyed TRIP assisted steels with excellent mechanical properties using continuous galvanizing thermal cycles.

Through analyzing the phase constituents and their evolution during plastic deformation and relating these features to the work hardening behaviour of the steels, the following conclusions can be reached:

- 1) The intercritical annealing temperature did not have a strong effect on the final microstructure of the investigated TRIP-assisted steels due to ferrite formation during quenching from the intercritical annealing to isothermal bainitic transformation temperatures. More equilibrium intercritical austenite transformed to ferrite when a higher intercritical annealing temperature was used.

- 2) A longer isothermal bainitic transformation hold time was beneficial in obtaining retained austenite of higher stability and producing less martensite, although sometimes the amount of retained austenite was lower. The stable retained austenite was important in improving the work hardening behaviour of the TRIP-assisted steels.
- 3) More ferrite formation was observed in the 1.5Al steels. This may be the reason for which the microstructure and strain-induced transformation kinetics of the 1.5Al steels were more sensitive to thermal processing parameters in the present case. Generally, the retained austenite in the 1.5Al steels exhibited higher stability.
- 4) Although lamellar retained austenite exhibited higher stability than blocky retained austenite, its amount was very limited. The martensitic transformation of blocky retained austenite was the main source of the TRIP effect in the present steels.
- 5) Retained austenite of higher stability transformed to martensite more gradually during plastic deformation. This effect efficiently attenuated decreases in the work hardening rate, $d\sigma/d\varepsilon$, and gave rise to a smoother evolution of the incremental work hardening coefficient, $d(\ln\sigma)/d(\ln\varepsilon)$, resulting in good combination of strength and ductility for the alloys.

- 6) One of the attenuating mechanisms for retarding decreases in the work hardening rate was the development of back stresses, which contributed kinematic hardening to the overall work hardening. Gradual transformation of retained austenite to martensite during plastic deformation continuously supplied new obstacles to dislocations and delayed the saturation of back stresses. The back stresses in the 1.5Al_35% γ 120s, 1.5Al_50% γ 60s and 1.5Al_50% γ 120s steels increased linearly with the square root of strain up to strains as large as 0.20 due to the high stability of retained austenite in these steels.
- 7) After about 70 ~ 80% of the contained retained austenite had transformed to martensite, the work hardening rate, $d\sigma/d\varepsilon$, decreased sharply and led to the onset of necking. Decohesion between ferrite and martensite and/or retained austenite that was not transformed was the main reason for the sharp decrease in work hardening rates and fracture of the steels.

REFERENCES

- ASTM International ASTM E 8M-04, Standard Test Methods for Tension Testing of Metallic Materials, ASTM International (2007)
- Atkinson et al. (1974) J. D. Atkinson, L. M. Brown and W. M. Stobbs, The work-hardening of copper-silica IV. The Bauschinger effect and plastic relaxation, *Philosophical Magazine*, 30 (1974) 1247-1280
- Bate and Wilson (1986) P. S. Bate and D. V. Wilson, Analysis of the bauschinger effect, *Acta Metallurgica*, 34 (1986) 1097-1105
- Bellhouse et al. (2007) E. Bellhouse, A. Mertens, and J. McDermid, Development of the surface structure of TRIP steels prior to hot-dip galvanizing, *Materials Science & Engineering A*, 463A (2007) 147-156
- Bellhouse and McDermid (2008) E. M. Bellhouse and J. R. McDermid, Analysis of the Fe–Zn interface of galvanized high Al-low Si TRIP steels, *Materials Science & Engineering A*, 491A (2008) 39-46
- Bellhouse and McDermid (2007) E. Bellhouse and J. R. McDermid, Effect of Continuous Galvanizing Heat Treatments on the Microstructure and Mechanical Properties of Al-Si TRIP Steels, *Materials Science and Technology 2007, AIST Steel Properties and Applications Conference Proceedings*, 295-304
- Bhadeshia (2002) H. K. D. H. Bhadeshia, TRIP assisted steels?, *ISIJ International*, 42 (2002) 1059-1060
- Bhadeshia (2001) H. K. D. H. Bhadeshia, *Bainite in Steels: Transformations, Microstructure and Properties*, 2nd ed., IOM Communications Ltd., London, 2001

- Bhadeshia and Edmonds (1980) H. K. D. H. Bhadeshia and D. V. Edmonds, Mechanism of Bainite Formation in Steels, *Acta Metallurgica*, 28 (1980) 1265-1273
- Bhadeshia and Honeycombe (2006) H. K. D. H. Bhadesia and S. R. Honeycombe, *Steels: Microstructure and Properties*, 3rd ed., Elsevier, 2006
- Brandt (1997) M. L. Brandt, Ph.D. Thesis, Northwestern University, 1997
- Brown and Stobbs (1971a) L. M. Brown and W. M. Stobbs, The Work-hardening of Copper-Silica I. A Model Based on Internal Stresses, with no Plastic Relaxation, *Philosophical Magazine*, 23 (1971) 1185-1199
- Brown and Stobbs (1971b) L. M. Brown and W. M. Stobbs, The work-hardening of copper-silica II. The role of plastic relaxation, *Philosophical Magazine*, 23 (1971) 1201-1233
- Cribb and Rigsbee (1979) W. R. Cribb and J. M. Rigsbee, Work-Hardening Behavior and Its Relationship to The Microstructure and Mechanical Properties of Dual Phase Steels, in R. A. Kot and J. W. Morris, eds. *Structure and Properties of Dual-Phase Steels*, AIME (1979) 91-117
- De Cooman (2004) B. C. De Cooman, Structure-properties relationship in TRIP steels containing carbide-free bainite, *Current Opinion in Solid State & Materials Science*, 8 (2004) 285-303
- De Meyer et al. (1999a) M. De Meyer, D. Vanderschueren, and B. C. De Cooman, The Influence of the Substitution of Si by Al on the Properties of Cold Rolled C-Mn-Si TRIP Steels, *ISIJ International*, 39 (1999) 813-822
- De Meyer et al. (1999b) M. De Meyer, D. Vanderschueren, K. De Blauwe and B. C. De Cooman, The Characterization of Retained Austenite in TRIP Steels by X-ray Diffraction, *The 41st MWSP Conference Proceedings*, ISS, 37 (1999) 483-491
- Dyson and Holmes (1970) D. J. Dyson and B. Holmes, Effect of alloying additions on the lattice parameter of austenite, *Journal of the Iron and Steel Institute*,

208 (1970) 469-474

- Emadoddin et al. (2006) E. Emadoddin, A. Akbarzadeh and Gh. Daneshi, Effect of intercritical annealing on retained austenite characterization in textured TRIP-assisted steel sheet, *Materials Characterization*, 57 (2006) 408-413
- Embury (1987) J. D. Embury, Structural Aspects of the Bauschinger Effect, *Materials Forum*, 10 (1987) 27-32
- Garcia-Gonzalez (2005) Garcia-Gonzalez, Ph.D. Thesis, University of Pittsburgh, 2005
- Gaude-Fugarolas and Jacques (2006) D. Gaude-Fugarolas and P. J. Jacques, A new physical model for the kinetics of the bainite transformation, *ISIJ International*, 46 (2006) 712-717
- Gerbase et al. (1979) J. Gerbase, J. D. Embury and R. M. Hobbs, The mechanical behavior of some dual phase steels - with emphasis on the initial work hardening rate, in R. A. Kot and J. W. Morris, eds. *Structure and Properties of Dual-Phase Steels*, AIME (1979) 118-144
- Ghosh and Olson (2001) G. Ghosh and G. B. Olson, Simulation of Paraequilibrium Growth in Multicomponent Systems, *Metallurgical and Materials Transactions A*, 32A (2001) 455-467
- Girault et al. (1999) E. Girault, P. Jacques, P. Ratchev, J. Van Humbeeck, B. Verlinden and E. Aernoudt, Study of the temperature dependence of the bainitic transformation rate in a multiphase TRIP-assisted steel, *Materials Science & Engineering A*, 273-275 (1999) 471-474
- Girault et al. (1998) E. Girault, P. Jacques, Ph. Harlet, K. Mols, J. Van Humbeeck, E. Aernoudt, and F. Delannay, Metallographic Methods for Revealing the Multiphase Microstructure of TRIP-Assisted Steels, *Materials Characterization*, 40 (1998) 111-118
- Goel et al. (1983) A. Goel, R. K. Ray and G. S. Murty, Bauschinger effect in a dual phase steel, *Scripta Metallurgica*, 17 (1983) 375-380

- Hashimoto et al. (2004) Shunichi Hashimoto, Shushi Ikeda, Koh-ichi Sugimoto and Syugo Miyake, Effects of Nb and Mo Addition to 0.2%C-1.5%Mn-1.5%Mn Steel on Mechanical Properties of Hot Rolled TRIP-aided Steel Sheets, *ISIJ International*, 44 (2004) 1590-1598
- Hill (1950) R. Hill, *The Mathematical Theory of Plasticity*, Oxford, Clarendon, 1950
- Huang et al. (2004) J. Huang, W. J. Poole and M. Militzer, Austenite Formation during Intercritical Annealing, *Metallurgical and Materials Transactions A*, 35A (2004) 3363-3375
- Ibrahim (1974) N. A. Ibrahim, Ph.D. Thesis, McMaster University, 1974
- Jacques et al. (2006) P. J. Jacques, Q. Furnemont, S. Godet, T. Pardoën, K. T. Conlon and F. Delannay, Micromechanical characterization of TRIP-assisted multiphase steels by *in situ* neutron diffraction, *Philosophical Magazine*, 86 (2006) 2371-2392
- Jacques (2004) P. J. Jacques, Transformation-induced plasticity for high strength formable steels, *Current Opinion in Solid State and Materials Science*, 8 (2004) 259-265
- Jacques et al. (2001a) P. J. Jacques, E. Girault, A. Mertens, B. Verlinden, J. van Humbeeck and F. Delannay, The developments of cold-rolled TRIP-assisted multiphase steels: Al-alloyed TRIP-assisted multiphase steels, *ISIJ International*, 41 (2001) 1068-1074
- Jacques et al. (2001b) P. Jacques, Q. Furnemont, A. Mertens, and F. Delannay, On the sources of work hardening in multiphase steels assisted by transformation-induced plasticity, *Philosophical Magazine*, 81 (2001) 1789-1812
- Jacques et al. (2001c) P. J. Jacques, J. Ladriere, and F. Delannay, On the Influence of Interactions between Phases on the Mechanical Stability of Retained Austenite in Transformation-Induced Plasticity Multiphase Steels,

-
- Metallurgical and Materials Transactions A, 32A (2001) 2759-2768
- Jacques et al. (2001d) P. Jacques, Q. Furnemont, T. Pardoën and F. Delannay, On the Role of Martensitic Transformation on Damage and Cracking Resistance in TRIP-assisted Multiphase Steels, *Acta Materialia*, 49 (2001) 139-152
- Jacques et al. (1999) P. Jacques, E. Girault, T. Catlin, N. Geerlofs, T. Kop, S. van de Zwaag, and F. Delannay, Bainite transformation of low carbon Mn-Si TRIP-assisted multiphase steels: influence of silicon content on cementite precipitation and austenite retention, *Materials Science & Engineering A*, 273-275 (1999) 475-479
- Jacques et al. (1998) P. Jacques, X. Cornet, Ph. Harlet, J. Ladrière and F. Delannay, Enhancement of the Mechanical Properties of a Low-Carbon Low-Silicon Steel by Formation of a Multiphased Microstructure Containing Retained Austenite, *Metallurgical and Materials Transactions A*, 29A (1998) 2383-2393
- Jha et al. (1987) B. K. Jha, Ram Avtar, V. Sagar Dwivedi, and V. Ramaswamy, Applicability of modified Crussard-Jaoul analysis on the deformation behaviour of dual-phase steels, *Journal of Materials Science Letters*, 6 (1987) 891-893
- Kim et al. (2001) Sung-Joon Kim, Chang Gil Lee, Ildong Chol and Sunghak Lee, Effects of Heat Treatments and Alloying Elements on the Microstructures and Mechanical Properties of 0.15 Wt Pct C Transformation-Induced Plasticity-Aided Cold-Rolled Steel Sheets, *Metallurgical and Materials Transactions A*, 32A (2001) 505-514
- Krizan and De Cooman (2008) D. Krizan and B. C. De Cooman, Analysis of the strain-induced Martensitic Transformation of Retained Austenite in Cold Rolled Micro-Alloyed TRIP Steel, *Steel Research International*, 79 (2008) 513-522
- Lacroix et al. (2008) G. Lacroix, T. Pardoën and P. J. Jacques, The fracture toughness of TRIP-assisted multiphase steels, *Acta Materialia*, 56 (2008) 3900-3913

- Lee et al. (2004) Chang Gil Lee, Sung-Joon Kim, Tae-Ho Lee and Sunghak Lee, Effects of volume fraction and stability of retained austenite on formability in a 0.1C-1.5Si-1.5Mn-0.5Cu TRIP-aided cold-rolled steel sheet, *Materials Science & Engineering A*, 371 (2004) 16-23
- Lloyd (1977) D. J. Lloyd, The baushinger effect in polycrystalline aluminium containing coarse particles, *Acta Metallurgica*, 25 (1977) 459-466
- Mahieu et al. (2002a) J. Mahieu, J. Maki, B. C. De Cooman, and S. Claessens, Phase Transformation and Mechanical Properties of Si-Free CMnAl Transformation-Induced Plasticity-Aided Steel, *Metallurgical and Materials Transactions A*, 33A (2002) 2573-2580
- Mahieu et al. (2002b) J. Mahieu, B. C. De Cooman, J. Maki and S. Claessens, Hot-dip galvanizing of Al alloyed TRIP steels, *Iron & Steelmaker*, 29 (2002) 29-34
- Mahieu et al. (2001) J. Mahieu, S. Claessens, and B. C. De Cooman, Galvanizability of High-Strength Steels for Automotive Applications, *Metallurgical and Materials Transactions A*, 32A (2001) 2905-2908
- Marder (2000) A. R. Marder, The metallurgy of zinc-coated steel, *Progress in Materials Science*, 45 (2000) 191-271
- Matlock et al. (1979) D. K. Matlock, G. Krauss, L. F. Ramos and G. S. Huppi, A Correlation of Processing Variables With Deformation Behavior of Dual Phase Steels, in R. A. Kot and J. W. Morris, eds. *Structure and Properties of Dual-Phase Steels*, AIME (1979) 62-90
- Matsumura et al. (1987) Osamu Matsumura, Yasuharu Sakuma, Hiroshi Takechi, Enhancement of Elongation by Retained Austenite in Intercritical Annealed 0.4C-1.5Si- 0.8Mn Steel, *Transactions of the Iron and Steel Institute of Japan*, 27 (1987) 570-579
- Mertens et al. (2003) A. Mertens, P. J. Jacques, L. Zhao, S. O. Kruijver, J. Sietsma and F. Delannay, On the influence of aluminium and silicon contents on the kinetics of bainite transformation of intercritical austenite, *Journal de*

- Mertens and McDermid (2005) A. Mertens and J. R. McDermid, The effect of continuous galvanizing thermal cycle on the microstructure and mechanical properties of two multi-phase TRIP-assisted steels, *Materials Science & Technology 2005, Developments in Sheet Products for Automotive Applications*, 25-35
- Minote et al. (1996) T. Minote, S. Torizuka, A. Ogawa and M. Niikura, Modeling of Transformation Behavior and Compositional Partitioning in TRIP Steel, *ISIJ International*, 36 (1996) 201-207
- Moan (1977) G. Moan, PhD Thesis, McMaster University, 1977
- Northern Eclipse Northern Eclipse Help Reference, Version 6.0 (2001)
- Olson and Cohen (1975) G. B. Olson and Morris Cohen, Kinetics of Strain-Induced Martensitic Nucleation, *Metallurgical Transactions A*, 6 (1975) 791-795
- Orowan (1959) E. Orowan, Causes and Effects of Internal Stresses, in *Internal Stresses and Fatigue in Metals*, eds. G. M. Rassweiler and W. L. Grube, Elsevier, 1959
- Perlade et al. (2003) A. Perlade, O. Bouaziz and Q. Furnemont, A physically based model for TRIP-aided carbon steels behaviour, *Materials Science & Engineering A*, 356A (2003) 145-152
- Reed-Hill et al. (1973) R. E. Reed-Hill, W. R. Cribb and S. N. Monteiro, Concerning the Analysis of Tensile Stress-Strain Data Using $\text{Log } d\sigma/d\varepsilon_p$ Versus $\text{Log } \sigma$ Diagrams, *Metallurgical Transactions*, 4 (1973) 2665-2667
- Ruhl and Cohen (1969) R. Ruhl and M. Cohen, Splat quenching of iron-carbon alloys, *Transactions of the Metallurgical Society of AIME*, 245 (1969) 241-251
- Sakuma et al. (1991) Yasuharu Sakuma, Osamu Matsumura and Osamu Akisue, Influence of C Content and Annealing Temperature on Microstructure and

-
- Mechanical Properties of 400°C Transformed Steel Containing Retained Austenite, *ISIJ International*, 31 (1991) 1348-1353
- Samajdar et al. (1998) I. Samajdar, E. Girault, B. Verlinden, E. Aernoudt and J. Van Humbeeck, Transformations during Intercritical Annealing of a TRIP-assisted Steel, *ISIJ International*, 38 (1998) 998-1006
- Samek et al. (2006) L. Samek, E. De Moor, J. Penning and B. C. De Cooman, Influence of alloying Elements on the Kinetics of Strain-Induced Martensitic Nucleation in Low-Alloy Multiphase High-Strength Steels, *Metallurgical and Materials Transactions A*, 37A (2006) 109-124
- Sinclair (2001) C. Sinclair, PhD Thesis, McMaster University, 2001
- Soliman and Palkowski (2008) Mohamed Soliman and Heinz Palkowski, On Factors Affecting the Phase Transformation and Mechanical Properties of Cold-Rolled Transformation-Induced-Plasticity-Aided Steel, *Metallurgical and Materials Transactions A*, 39A (2008) 2513-2527
- Speich and Miller (1979) G. R. Speich and R. L. Miller, Mechanical Properties of Ferrite-Martensite Steels, in R. A. Kot and J. W. Morris, eds. *Structure and Properties of Dual-Phase Steels*, AIME (1979) 145-182
- Speich et al. (1981) G. R. Speich, V. A. Demarest and R. L. Miller, Formation of Austenite during Intercritical Annealing of Dual-Phase Steels, *Metallurgical Transactions A*, 12A (1981) 1419-1428
- Spencer (2004) K. Spencer, PhD Thesis, McMaster University, 2004
- Suh et al. (2007) Dong-Woo Suh, Seong-Jun Park, Chang-Seok Oh and Sung-Joon Kim, Influence of partial replacement of Si by Al on the change of phase fraction during heat treatment of TRIP steel, *Scripta Materialia*, 57 (2007) 1097-1100
- Thelning (1984) K. E. Thelning, *Steel and Its Heat Treatment*, 2nd ed., Butterworths, 1984
- Timokhina et al. I. B. Timokhina, P. D. Hodgson, and E. V. Pereloma, Effect of

-
- (2004) Microstructure on the Stability of Retained Austenite in Transformation- Induced-Plasticity Steels, Metallurgical and Materials Transactions A, 35A (2004) 2331-2341
- Traint et al. (2002) S. Traint, A. Pichler, K. Hauzenberger, P. Stiaszny and E. Werner, Influence of silicon, aluminum, phosphorus and copper on the phase transformations of low alloyed TRIP-steels, Steel Research, 73 (2002) 259-266
- Uko (1978) D. K. Uko, Ph.D. Thesis, McMaster University, 1978
- Wilson (1965) D. V. Wilson, Reversible work hardening in alloys of cubic metals, Acta Metallurgica, 13 (1965) 807-814
- Wu and Li (2006) Di Wu and Zhuang Li, Effect of Thermomechanical Controlled Processing on the Microstructure and Mechanical Properties of Fe-C-Mn-Si Multiphase Steels, ISIJ International, 46 (2006) 1059-1066
- Zackay et al. (1967) Victor F. Zackay, Earl R. Parker, Dieter Fahr and Raymond Busch, The Enhancement of Ductility in High-Strength Steels, Transactions of the ASM, (1967) 252-259
- Zhao et al. (2001) L. Zhao, N. H. van Dijk, E. Bruck, J. Sietsma and S. van der Zwaag, Magnetic and X-ray diffraction measurements for the determination of retained austenite in TRIP steels, Materials Science & Engineering A, 313 (2001) 145-152